AAPG BULLETIN

Impact of diagenesis on the pore evolution and sealing capacity of carbonate cap rocks in the Tarim Basin, China

Jun Wu, Tailiang Fan, Enrique Gomez-Rivas, Anna Travé, Qian Cao, Zhiqian Gao, Shanshan Wang, and Zhihong Kang

AAPG Bulletin published online 15 September 2022
doi: 10.1306/11082120136

Cite as: Wu, J., T. Fan, E. Gomez-Rivas, A. Travé, Q. Cao, Z. Gao, S. Wang, and Z. Kang, **Impact of diagenesis on the pore evolution and sealing capacity of carbonate cap rocks in the Tarim Basin, China**, *(in press; preliminary version published online Ahead of Print* 15 September 2022*):* AAPG Bulletin, doi: 10.1306/11082120136.

Impact of diagenesis on the pore evolution and sealing capacity of carbonate cap rocks in the Tarim Basin, China

Jun Wu [a, b, c*], Tailiang Fan [a, b], Enrique Gomez-Rivas [c], Anna Travé [c], Qian Cao [d], Zhiqian Gao [a, b], Shanshan Wang [e], Zhihong Kang [a, b*]

***E-mail addresses of the corresponding authors: zgdzdxbjwj@126.com (J. Wu), kangzh98@cugb.edu.cn (Z. Kang)**

a, School of Energy Resources, China University of Geosciences (Beijing), Beijing 100083, China;

b, Key Laboratory of Marine Reservoir Evolution and Hydrocarbon Enrichment Mechanism, Ministry of Education, Beijing 100083, China

c, Department of Mineralogy, Petrology and Applied Geology, Faculty of Earth Sciences, University of Barcelona (UB), Barcelona 08028, Spain

d, Exploration and Development Research Institute of PetroChina Changqing Oilfield Company, Xi'an 710018, China

e, Beijing Municipal Commission of Planning and Natural Resources Yanqing Branch, Beijing 102100, China

Acknowledgements

This study was supported by the National Natural Science Foundation of China (42102151, 41802155, 41972130, and U19B6003), DGICYT Spanish Projects, PGC2018-093903-B-C22 Ministerio de Ciencia, Innovación y Universidades / Agencia Estatal de Investigación / Fondo Europeo de Desarrollo Regional, Unión Europea, and the Grup Consolidat de Recerca "Geologia Sedimentària" (2017-SGR-824). Jun Wu also appreciates the China Scholarship Council (201806400037) for providing financial support during the study at the University of Barcelona. EGR acknowledges funding by the Spanish Ministry of Science, Innovation and Universities for the "Ramón y Cajal" fellowship RYC2018-026335-I. We would like to thank AAPG Editor Robert K. Merrill, Technical Editor Andrea Sharrer and three anonymous reviewers, whose constructive suggestions and critical comments that significantly improved the paper. The authors thank Yue Chen, Xinxin Yin, and Xue Fan for sampling during fieldwork and preparing the test samples.

Abstract: Analyzing the pore structure and sealing efficiency of carbonate cap rocks is essential to assess their ability to retain hydrocarbons in reservoirs and minimize leaking risks. In this contribution, the impact of diagenesis on the cap rock's sealing capacity is studied in terms of their pore structure by analyzing rock samples from Ordovician carbonate reservoirs (Tarim Basin). Four lithology types are recognized: highly compacted peloidal packstone-grainstone, highly cemented intraclastic-oolitic-bioclastic grainstone, peloidal dolomitic limestone, and incipiently dolomitized peloidal packstone-grainstone. The pore types of cap rocks include microfractures, intercrystalline pores, intergranular pores, and dissolution vugs. The pore structure of these cap rocks was heterogeneously modified by six diagenetic processes, including calcite cementation, dissolution, mechanical and chemical compaction, dolomitization, and calcitization (dedolomitization). Three situations affect the rock's sealing capacity: (1) grainstone cap rocks present high sealing capacity in cases where compaction preceded cementation; (2) residual microfractures connecting adjacent pores result in low sealing capacity; (3) increasing grain size in grainstones results in a larger proportion of intergranular pores being cemented. Four classes of cap rocks have been defined according to the lithology, pore structures, diagenetic alterations, and sealing performance. Class I cap rocks present the best sealing capacity because they underwent intense mechanical compaction, abundant chemical compaction and calcite cementation, which contributed to the heterogeneous pore structures with poor pore connectivity. A four-stage conceptual model of pore evolution of cap rocks is presented to reveal how the diagenetic evolution of cap rocks determines the heterogeneity of their sealing capacity in carbonate reservoirs.

Keywords: Carbonate cap rock; Diagenesis; Pore structure evolution; Sealing capacity classification; Tarim Basin.

1 Introduction

Cap rocks are defined as lithostratigraphic layered units having the ability to interrupt hydrocarbon migration. They are generally divided into three categories according to their lithology: mudrocks, evaporites, and carbonate rocks (Sutton et al., 2004; Zhou et al., 2012; Fu et al., 2018; Bihani and Daigle, 2019). Cap rocks are characterized by their low porosity and low permeability and are therefore a fundamental component of the petroleum entrapment system (Schowalter, 1979; Schmitt et al., 2013; Rezaeyan et al., 2015), because they prevent the upwards migration of hydrocarbons from the underlying reservoir (Boulin et al., 2013). The sealing capacity of a rock can be quantified as the gas column height that the seal can hold (Cheng et al., 2006; Amann-Hildenbrand et al., 2013; Wu et al., 2019). This corresponds to the capillary pressure at which a trapped fluid starts leaking through the overlying seal rocks (Vavra et al., 1992; Schmitt et al., 2013; Rezaeyan et al., 2015). Understanding the sealing capacity of cap rocks and their heterogeneity is key for: (1) the successful forecasting of favorable zones for oil and gas production (He et al., 2016); (2) to accurately evaluate the sealing of captured carbon in storage sites (for carbon capture and storage) and the geological disposal of nuclear waste (Kaldi et al., 2013; Espinoza and Santamarina, 2017; Górniak, 2019).

Even though huge volumes of hydrocarbons are stored in carbonate reservoirs, little attention has been paid to the study of carbonate cap rocks, probably due to their heterogeneous vertical and lateral distribution and complex combinations of depositional processes and diagenetic alterations that together control their sealing potential (Lü et al., 2017; Zhou et al., 2019). Previous studies of carbonate cap rocks mainly aimed to identify and predict their spatial and temporal distribution (Lü et al., 2017; Wu et al., 2018a), together with the characterization of their pore structures (Wu et al., 2019, 2021; Zhou et al., 2019). Recent systematic work on carbonate cap rock characterization includes the following aspects: (1) Four qualitative recognition patterns and quantitative identification criteria have been established to reveal that five sets of cap rocks are well superimposed but laterally less continuous (Wu et al., 2018a). (2) A four-stage conceptual model is proposed to explain the relationship between dolomites and pyrobitumen (Wu et al., 2018b). Highly abundant stylolites with the occlusion of residual bitumen and precipitation of cements resulted in the low porosity and permeability of cap rocks. (3) Six types of pore structures and fractal dimensions are classified based on the pore size distribution of cap rocks (Wu et al., 2019). Macropores and mesopores have a significant negative correlation with fractal changes. The sealing capacity of cap rocks shows a good correlation (either exponential or linear) with fractal dimensions (Wu et al., 2021). The increasing proportion of macropores results in a decrease in the rock's sealing capacity.

Meanwhile, the sealing capacity of cap rocks is primarily controlled by the distribution of their narrow pore throat structures (Daniel and Kaldi, 2009; Norbisrath et al. 2015; Espinoza and Santamarina, 2017). Generally, the pore systems of carbonate rocks, including multiscale fractures, vugs, and cavities, always exhibit extremely high heterogeneity with complex pore morphologies and pore size distributions (Hollis et al., 2010; Kim et al., 2011; Garing et al., 2014; Baqués et al., 2020). The study of Wu et al. (2019) revealed that the pore space of carbonate cap rocks is typically formed by macropores (with a diameter larger than 1 μm), mesopores (ranging between 0.1 and 1 μm) and transitional pores (from 0.01 to 0.1 μm). The pore space distribution in rocks containing macropores and mesopores is normally more heterogeneous than that of rocks dominated by transitional pores. In general, the heterogeneity of pore structures and thus the sealing capacity gets enhanced when the proportion of mesopores increases and the proportion of macropores decreases. A rock can act as an effective seal when the threshold capillary pressure is greater than the underlying buoyancy pressure of the fluid column (Amann-Hildenbrand et al., 2013; Nourollah and Urosevic, 2019). The rock capillary pressure can be estimated from a series of microscopic laboratory tests, such as mercury intrusion capillary pressure (MICP), rate-controlled porosimetry (RCP), and high-pressure mercury intrusion porosimetry (HPMIP) (Schlömer and Krooss, 1997; Hollis et al., 2010; Honarmand and Amini 2012; Li et al., 2017b; Xiao et al., 2017).

Carbonate rocks are typically very heterogeneous due to the combination of (1) lateral and vertical changes in sedimentary environments during their deposition, (2) syn- to postdepositional diagenetic alterations and (3) the presence of tectonic structures such as faults, fractures and tectonic stylolites (Melim et al., 2002; Cox et al., 2010; Hollis et al., 2010; Wang et al., 2012; Martín-Martín et al., 2013, 2018; Rustichelli et al., 2013; Li et al., 2017b; Li et al., 2017c; Javanbakht et al., 2018; Jiang et al., 2018). Diagenetic alterations result in strong heterogeneity of carbonate reservoirs in most cases (Moore, 2001; Teillet et al., 2019), because the overprint of processes such as compaction, dissolution, cementation, and mineral replacement significantly alter the primary porosity and permeability of the rock (Longman, 1980; Morad et al., 2018; Ehrenberg and Baek, 2019; Sfidari et al., 2019), eventually resulting in multiporosity systems. Numerous studies have demonstrated how the depositional characteristics and subsequent diagenetic modifications of carbonate rocks not only have a significant impact on the abundance of pores and pore structures but have also shown how they control fluid flow and the rock’s storage properties (Mazzullo, 1981; Amel et al., 2015; Dou et al., 2018; Liu and Xie, 2018; Morad et al., 2018; Ishaq et al., 2019). A volume of sediment can progressively go through different diagenetic environments, potentially resulting in a final rock with very different petrophysical properties depending on the diagenetic path (*e.g.*, Roehl and Choquette, 1990; Moore, 2001).

Diagenetic overprints can have a constructive or destructive impact on the rock's pore structure. Diagenetic processes play a significant role in the formation and occlusion of the pore space, as well as on the sealing potential of carbonate cap rocks. For example, the pore size of carbonate rocks normally decreases with mechanical compaction, secondary pores form because of dissolution of carbonate components or cements while cements occlude primary and secondary pores (e.g., Moore and Wade, 2013; Javanbakht et al., 2018; Morad et al., 2018). Mechanical compaction reduces the bulk rock volume as a consequence of progressive burial, dissolution generally results in a porosity increase through the enhancement of fluid mobility and facilitates hydrocarbon migration (Jiang et al., 2018; Dou et al., 2018), and cementation occludes the pore networks and increases their tortuosity. The early compaction apparently constrains fluid flow and leads to nearly complete cementation, which contributes to the low permeability of carbonate rocks (Melim et al., 2001). The dissolved unstable calcite minerals preferentially precipitate again as new pore-filling products. Furthermore, diagenetic alternations such as dissolution and cementation control the petrophysical properties, by enhancing or diminishing porosity and permeability of carbonate reservoirs (Croizé et al., 2010; Makhloufi et al., 2013; Ali et al., 2018; Al Khalifah et al., 2020).

A considerable number of analytical techniques have been used to characterize the pore structure of carbonate rocks, including thin-section petrography, focused ion beam scanning electron microscopy (FIB-SEM), backscattered scanning electron microscopy (BSEM), field emission scanning electron microscopy (FE-SEM) and micro- and nanocomputed tomography (micro-CT/nano-CT) (Van Geet et al., 2000; Al-Kharusi and Blunt, 2008; Bera et al., 2012; Fusi and Martinez-Martinez, 2013; Mayo et al., 2015). Among these methods, casting thin sections are impregnated with methylene blue dye to make the pore space easier to identify and has been used to study the pore types and pore structures in two-dimensions, but the magnification of two-dimensional (2-D) pore images by casting thin section petrography is relatively limited (Okabe and Blunt, 2007). FIB-SEM, BSEM and FE-SEM analysis result in micrographs with enough resolution for the detection of the 2-D microscopic morphology and pore size distribution at different scales but fail to obtain information such as the connectivity of pore throats in three dimensions (Sok et al., 2010; Bera et al., 2012). Both micro-CT and nano-CT scanning methods are effective ways of reconstructing the three-dimensional spatial arrangement of pore network systems using numerical values from the scanned image (Fusi and Martinez-Martinez, 2013). They can accurately locate the exact position of different pore throats in the rock samples, but result in an unrealistic simulation of transport properties and fail in analyzing nanopores (Al-Kharusi and Blunt, 2008; Mayo, et al., 2015). Micro-CT analysis fails to reveal porosity related to fluid-flow at the nanoscale due to the significant limitation of the finite voxel size, and thus cannot differentiate ores or minerals with similar attenuation coefficients (Wang and Miller, 2020). Nano-CT is more sensitive to the misaligned geometry because of the movement of object manipulator and has a lower signal-to-noise ratio and larger data volume than micro-CT. Consequently, these shortcomings increase the difficulty of reconstructing the pore structure at high resolution (Tang and Li, 2020). In summary, all these methods alone present a series of limitations and measurement errors for the determination of pore-size distributions (Ito et al., 2011; Lai et al., 2018). Combinations of techniques can help to analyze the spectra of data that is required to achieve a complete quantification of pore structures in carbonate rocks (Zhang et al., 2018).

The relationships between diagenetic processes and the pore structure heterogeneity for facies deposited in certain environments have been widely investigated in sandstone reservoirs (e.g., Li et al., 2017b; Li et al., 2017c; Dou et al., 2018; Oluwadebi et al., 2018; Kadkhodaie-Ilkhchi et al., 2019; Li et al., 2019). However, most diagenetic studies in carbonate rocks have mainly focused on how different diagenetic processes impact reservoir quality (Mazzullo, 1981; Amel et al., 2015; Liu and Xie, 2018; Zhang et al., 2018), and not so much on how diagenesis relates to the resulting petrophysical properties of carbonate cap rocks (Daniel and Kaldi, 2009). Accordingly, the scientific and oil & gas industry communities still lack systematic studies focusing on analyzing how different diagenetic processes control the evolution of the pore space, the distribution of pore sizes and, therefore, how they determine the sealing capacity of carbonate cap rocks, despite that such studies are essential to better predict the presence and sealing properties of carbonate cap rocks.

In order to contribute to filling the knowledge gap between carbonate rock diagenetic alterations and the sealing capacity evolution associated with their pore structure, here we fully characterize the spectrum of pore sizes and pore structures of a series of carbonate cap rock samples, and reveal how diagenesis impacts the pore evolution and sealing capacity of such rocks. It is widely known that high-pressure mercury intrusion porosimetry (HPMIP) is an effective method to characterize the pore structure of a carbonate rock, including its pore size distribution (from nanometers to micrometers), the geometrical shape of pores, and their connectivity and morphology (Münch and Holzer, 2008; Sakhaee-Pour and Bryant, 2014; Song et al., 2018). Meanwhile, the combination of mercury injection capillary pressure (MICP) and nitrogen gas adsorption (N_2GA) has proven to have good application prospects in quantitatively determining the sealing capacity of cap rocks (Schmitt et al., 2013; Wu et al., 2019). The mercury intrusion capillary pressure analysis is suitable to investigate pore structures with pore sizes of the macro- and mesopore range, while the nitrogen gas adsorption technique can be utilized to study the distribution of meso- and micropores. In this contribution, we combine these techniques to study how different diagenetic processes affect the heterogeneity of pore structure evolution and sealing capacity of carbonate cap rocks using samples from outcrops and drill cores of the Yingshan Formation in the Tarim Basin (China).

The Tahe oilfield is the first discovered Paleozoic marine carbonate oilfield in the Tarim Basin that includes paleokarst-controlled reservoirs (Figure 1A) (Kang, 2007;

Tian et al., 2016; Baqués et al., 2020). It hosts 4.306 Gbbl (5.875×10^8 tons) of proven original oil-in-place (OOIP) and 649.719 BCF (183.98×10^8 m^3) of natural gas in Ordovician formations (Ma et al., 2017; Han et al., 2019a). The carbonate cap rocks of the Yingshan Formation are considered some of the key seals in the Tarim Basin and played a crucial role in the accumulation and preservation of hydrocarbons (Lin, 2002; He et al., 2016; Lü et al., 2017; Wu et al., 2018a; Zhou et al., 2019). Samples of the carbonate cap rocks obtained from wells in the Tahe oilfield present similar depositional and petrographic characteristics to those exposed in outcrops of the Keping and Bachu counties of the northwestern edge of the Tarim Basin (Figure 1B, C) (Kang, 1989; Ji et al., 2013; Zhou et al., 2019). Wang et al. (2019) have proposed a depositional model for the Yingshan Formation carbonates in the Tarim Basin, including the presence of restricted carbonate and open carbonate platforms. The former comprises three successive environments, namely restricted tidal flat, lagoon, and barrier shoal (Gao et al., 2018; Wu et al., 2018b), while the latter includes intraplatform shoal and intershoal sea (Wang et al., 2018). Therefore, such outcropping rocks are considered as analogs of the subsurface carbonates in reservoirs (Tian et al., 2016; Wang et al., 2019). Accordingly, the detailed study of the exposed carbonate cap rock is essential to understand the sealing mechanisms for different pore structures and to improve the predictions of pore evolution and sealing capacity in reservoirs.

The aims of this contribution are: (1) to characterize the dominating lithology types and diagenetic processes of the study carbonate cap rocks; (2) to unravel the heterogeneity of pore structures and sealing performance of carbonate cap rocks; (3) to propose a pore evolution conceptual model to dynamically evaluate the variation of the sealing capacity of carbonate cap rocks.

2 Geological setting

2.1 Sedimentary background

The Tarim Basin has an area of 56×10^4 km^2 (~21.62×10^4 mi^2) and is the largest petroliferous basin in China. It is a multicycle composite basin bound by the Tianshan Mountains to the north, the Kunlun Mountains to the southwest and the Altyn Mountains to the southeast (Kang, 2007) (Figure 1A). This basin underwent multi-stage tectonic episodes during the Caledonian, Hercynian, Indosinian, Yanshanian and Himalayan Orogenies (He et al., 2016).

The studied outcrop sections in the Keping and Bachu counties are named Penglaiba, Yangjikan, Kepingshuinichang and Dabantage. They are located in the Keping uplift of the northwestern margin of the Tarim Basin (Figure 1B). The Ordovician strata account for the main carbonate rocks in this basin and can be divided into six formations from bottom to top: Lower Ordovician Penglaiba, Lower-Middle Ordovician Yingshan, Middle Ordovician Yijianfang, and Upper Ordovician Qiaerbake, Lianglitage and Sangtamu Formations (Figure 2) (Qi and Yun, 2010; Tian et al., 2016). Due to tectonic inversion from extensional to compressional setting in the Tabei uplift, the dominant carbonate depositional system that formed the Cambrian-Ordovician formations evolved to a mixed carbonate-siliciclastic sedimentary system in the Late Ordovician. The depositional facies from the Penglaiba to the Sangtamu Formation consist of restrictive platform, open platform, platform margin, and mixed continental shelf deposits (Han et al., 2019a).

The Penglaiba Formation is mostly composed of a restricted carbonate platform carbonates (Dong et al., 2013), mostly dolomitized. The restricted carbonate platform mainly comprised tidal flat and lagoon deposits. It formed during the Early Ordovician and is dominated by fine- to medium-crystalline dolomite. Its thickness mostly ranges between 300 and 500 m but can be up to 1500 m.

The Yingshan Formation is composed of shallow carbonate platform carbonates, partially dolomitized (Ruan et al., 2013). It formed during the Early Ordovician and Middle Ordovician and is generally 250-600 m thick, with a maximum thickness locally exceeding 900 m. The Yingshan Formation is commonly divided into two parts, according to a clear lithological change from dominant dolomite and dolomitic limestones in the lower part to limestones in the upper part (Chen et al., 2003; Wang et al., 2018). The rocks of the lower part of the Yinshan Formation are dominated by fine crystalline dolomite and peloidal dolomitic limestone, and they have been interpreted as resulting from deposition in a restricted carbonate platform. The rocks of the upper part of the Yingshan Formation are dominated by peloidal packstone and intraclastic grainstone, and they are thought to correspond to an open carbonate platform (Han et al., 2015; Du et al., 2017). The open carbonate platform mainly comprised intrashoal platform and intershoal sea (Wang et al., 2019). The carbonate reservoirs of the upper parts of the Yingshan Formation correspond to paleokarsts with fracture-vuggy-cavity pore systems (Chen et al., 2012). The dense intervals of the Yingshan Formation carbonates are widely recognized as the local sealing unit for hydrocarbons in the Tarim Basin (Figure 3) (Wu et al., 2018b), and therefore has huge economic importance.

The Yijianfang Formation has a wide thickness variation (from 0 to 110 m) and is divided into two parts according to the lithofacies association. The rocks of the lower part of the Yijiangfang Formation are dominated by intraclastic grainstone and algae-bearing oolitic grainstone, which correspond to the depositional environment of the carbonate platform (Xu et al., 2012). The rocks of the upper part of this formation are dominated by oolitic and bioclastic grainstone and cyanobacteria bindstone, which corresponds to the sedimentary environment of the carbonate platform margin reef (Yu et al., 2008). The reef building organisms consist of receptaculitids and sponges (Xu et al., 2012).

The Qiaerbake, Lianglitage and Sangtamu Formations consist of mixed continental shelf facies comprising mud-bearing nodular limestone, argillaceous limestone, and siliciclastic mudrock. The thicknesses of the Qiaerbake and Lianglitage Formations are 0-35 m and 0-102 m, respectively (Liu et al., 2017). The Sangtamu Formation is 0-600 m thick and acts as high-quality regional cap rock for the underlying carbonate reservoirs of the Yingshan and Yijianfang Formations (Ding et al., 2020).

2.2 Tectonic and burial history

The Tahe oilfield is located in the southern slope of the Akekule arch within the Tabei uplift of the Tarim Basin (Figure 1C) (Lin, 2002). The Akekule arch is a long-term paleohigh on the basis of the sub-Sinian metamorphic basement. This arch experienced four different stages with three significant uplifts for the Ordovician strata. Stage 1: Thick and massive Cambrian-Ordovician carbonates were deposited and formed the stable platform before the late Caledonian Orogeny. Pervasive karstification took place during the middle Caledonian Orogeny (including three episodes, namely I, II and III) (Tian et al., 2016). Episode I of the middle Caledonian karstification occurred between the deposition of the middle Yijianfan and the upper Qiaerbake Formations. The Tabei uplift was uplifted gradually and a slight karstification exposure formed in the northern part of the Akekule arch (Han et al., 2019a). Episode II took place between the deposition of the upper Lianglitage and Qiaerbake Formations, the rocks of the Lianglitage Formation was directly exposed to meteoric water and suffered from karstfication. Episode III occurred between the sedimentation of the upper Sangtamu Formation and that of the Silurian strata (He et al., 2016). Stage 2: The late Caledonian Orogeny (Late Ordovician to early Silurian) to early Hercynian Orogeny (Late Devonian to early Carboniferous) resulted in the formation of a paleomorphological high during this stable uplift. Another significant karstification event took place, leading to the denudation of Silurian, Devonian and part of the Middle and Upper Ordovician strata. Therefore, the Ordovician strata in the north part of the Tahe oilfield were eroded to some extent due to complex erosional episodes. For example, the Yingshan Formation was partially denuded and the Lianglitage and Sangtamu Formations were completely denuded, thus the Carboniferous Bachu Formation unconformably overlies the Yingshan Formation (Figure 2), while they remained well-preserved in the southern part (Chen et al., 2003). Stage 3: During the late Hercynian Orogeny (late Permian) and the Indosinian Orogeny, the Tabei uplift was subjected to compressional tectonics, further deforming it from its original shape. Stage 4: The present tectonic configuration of the Tabei uplift was achieved after some adjustments during the Yanshan-Himalayan Orogeny. The Ordovician strata in the Tahe oilfield subsided and underwent progressive burial. The Paleozoic strata in the Akekule arch were tilted towards the south (Tian et al., 2016).

These study outcrop sections in the Keping uplift were subjected to extensional tectonic settings early in the Caledonian Orogeny (Wang et al., 2019) and were part of the passive continental margin (Jiang et al., 2015). Subsequently, a large-scale tectonically controlled transgression occurred in the middle to late Caledonian Orogeny (488.3-416 Ma) (Han et al., 2015; Wang et al., 2018). The Yingshan Formation at the Dabantage and Penglaiba outcrops experienced two rapid subsidence stages during the Middle Ordovician and middle Permian (Kang, 1989; Dong et al., 2013), with a maximum burial depth of about 4000 m (Du et al., 2017). During the Permian, the

Keping uplift along the northwestern flank of Tarim block extensively underwent uplift due to the amalgamation between the island arc of middle Tianshan and Tarim plates (Jia et al., 1998). At the end of Permian, the uplifted study area, resulting from the domal uplift of a mantle plume, was exposed to the near-surface and underwent a denudation as demonstrated by Mesozoic lacuna (Yang et al., 2007; N. Chen et al., 2014; Jiang et al., 2015). The rocks corresponding to the studied outcrop sections in the Keping uplift were affected by the Himalayan Orogeny to form a series of east-northeast-striking imbricated overthrust nappes because of the collision from the Indian plate farther south and Asian plate in the Cenozoic (Yang et al., 2006; Dong et al., 2013; Du et al., 2017), resulting in the present-day exposure of this formation (Zhou et al., 2019) (Figure 4).

Investigating the timing and chronology of hydrocarbon charging is not only of significance for the study of the temporal-spatial coupling of hydrocarbon migration and accumulation, but also to evaluate the sealing effectiveness of cap rocks. This is because the sequence of hydrocarbon charging and cap rock formation determines their sealing effectiveness. Carbonate rocks can typically be effective seals when they formed a long time before hydrocarbon charging. Otherwise, hydrocarbon leakage can take place when the cap rocks develop during or after hydrocarbon charging. There were three hydrocarbon charging stages during the whole geological history of the Tahe oilfield (Chen et al., 2014). The first two phases occurred during the middle to late Caledonian Orogeny (463.2-414.9 Ma) and the late Hercynian Orogeny (312.9-

268.8 Ma), respectively. The third natural gas charging phase took place during the Himalayan Orogeny (22-4.8 Ma) (Figure 4).

3 Samples and methods

This study is based on the analysis of samples from four outcrop sections and six wells from the Tarim Basin (Table 1). The classification of carbonate rocks in this study follows Dunhams (1962), which is based on depositional textures. Previous studies revealed that pore sizes of carbonate cap rocks in this formation are highly variable, and range from several nanometers to tens of micrometers (Wu et al., 2018b, 2019). Accordingly, the pore size classification scheme proposed by Xoaoth (1966), Li et al. (2017a) and Wu et al. (2019) was used in this study. This classification considers macropores (> 1 μm), mesopores (0.1-1 μm), transitional pores (0.01-0.1 μm) and micropores (＜0.01 μm).

3.1 Thin-section petrography

A total of 375 carbonate cap rock samples were chosen for thin-section preparation in this study, with the aim of studying the depositional characteristics and diagenetic evolution of each rock type. 180 of them are from wells and 195 from outcrops. 225 of these thin sections were only 1/3-stained with Alizarin Red S to differentiate calcite and dolomite, while the other 150 were not only 1/3-stained with Alizarin Red S but also impregnated with methylene blue dye to make the pore space easier to identify. They were studied under petrographic optical microscopes at the China University of

Geosciences (Beijing).

The grain size distribution was quantified from photomicrographs using digital image analysis techniques (Grove and Jerram, 2011). Zhang et al. (2014) demonstrated that a large number of images should be taken to cover a representative number of grains when analyzing particularly heterogeneous samples. Our previous studies confirm that measuring 80 grains per thin section meets the grain size quantification of carbonate cap rocks in the Tarim Basin (Wu et al., 2019). The calcite cement content was estimated by volumetric percentages from at least eight photomicrographs of each thin section using image analysis software (e.g. Adobe Photoshop). This quantification workflow was divided in three steps (Zhang et al., 2014): (1) image preparation: microscopic images were taken from thin sections, and image color, saturation, brightness, and contrast were adjusted, (2) selection and pixels reading: the calcite cement was selected and filled with a color on a single layer, then the number of pixels of the selected calcite cement were read, and (3) data processing: the ratio of the pixel number of the calcite cement to the whole image equals the content of calcite cement. Further comparisons of calcite cement content between thin sections could be achieved by analyzing the similarities and differences in gray levels or colors in photomicrographs using pixel management techniques (Zhang et al., 2014), and by using shape-selection tools to capture calcite cement, which typically presents a certain outline (Wang et al., 2015).

3.2 Scanning electron microscope measurements

Fifteen broken carbonate rock samples (0.5 cm×1.0 cm×0.2 mm) coated with gold were observed using an FEI Quanta FEG450 SEM with a working current set at an accelerating voltage of 20.0 kV and distance of 8-9 mm at the Experimental Research Center of Unconventional Technology Research Institute of CNOOC in Tianjin (China). Scanning electron microscopy (SEM) was used to characterize the microporosity characteristics and cement morphology in carbonate cap rock intervals. The carbonate porosity classification of Choquette and Pray (1970) was used in this study. In addition, energy dispersive spectrometry (EDS) was used to analyze the detailed mineral compositions of grains and cements.

3.3 High-pressure mercury intrusion porosimetry analysis

Twenty carbonate cap rock plug samples (nine from outcrops and eleven from drill cores) with a diameter of 25 mm and length of 39-51 mm were selected for pore structure and porosity and permeability analysis at the experimental research center of unconventional technology research institute of CNOOC. An Automatic 9510-III High-pressure Mercury Intrusion Porosimeter was utilized to investigate the pore size distribution using the Washburn equation (Washburn, 1921).

$$P_c = \frac{2\sigma\cos\theta}{r} \tag{1}$$

where P_c is the capillary pressure in dyne/cm^2; σ is the interfacial tension of air/mercury in dyne/cm; θ is the wetting angle in °; r is the pore throat radius in cm.

The interfacial tension of air/mercury and wetting angles are 485 mN/m and 140° in this study. Thus, the Washburn equation can be simplified as:

$$P_c = \frac{0.735}{r} \tag{2}$$

where P_c and r are the capillary pressure in MPa and pore throat radius in μm, respectively. The pore radii can be automatically acquired in accordance with the specific pressures during the intrusion/extrusion processes according to Equation (2). The test pressures vary from 0.012 to 116.667 MPa, which correspond to a pore radius range from 63 μm to 0.006 μm, respectively.

3.4 Combination of MICP and N_2GA analyses

A total of 40 carbonate cap rock plugs (21 from drill wells and 19 from outcrop sections) with a diameter of 25 mm were selected to investigate their sealing capacity. In order to minimize the rock sample damage as much as possible during the sampling process, two steps were taken in the field: (1) the weathered carbonate layer on the outcrop surface was removed to expose the fresh rock surface; (2) the rock was then drilled to a depth of 40-50 cm using a Shaw single backpack drill rig to obtain a cylindrical rock sample. The combination of MICP and N_2GA analyses were tested at the Experimental Research Center of the Wuxi Research Institute of Petroleum Geology, SINOPEC. The sealing performance of these selected samples was determined using an Autopore IV9520 Micropore Structure Analyzer. The MICP technique was utilized to characterize the distribution of pore sizes with pore radii in the range of 6 to 10,000 nm, and the N_2GA test was used to quantify porosity defined by pores with radii ranging from 1 to 10 nm. The existence of an overlapping region of pore size between 6 nm and 10 nm provides the foundation for the combination of MICP and N_2GA analyses. Consequently, the 6 nm pore size was used as a linking point to establish the connection of both techniques and to obtain the distribution of pore size in the range of 1-10,000 nm (Cheng et al., 2006). The detailed description of the combination of MICP and N_2GA test methods can be read in Wu et al. (2019, 2021).

Hence, three key testing parameters, comprising height of the gas column (*HGC*), breakthrough pressure (P_b) and cover coefficient (*CC*) can be directly obtained to quantitatively analyze the sealing capacity of cap rocks. The *HGC* that a seal can hold before the seal begins to leak refers to the critical accumulation height of oil and gas (Watts, 1987; Lohr and Hackley, 2018). The *HGC* that can be stored under a cap rock in a reservoir mainly depends on the P_b of cap rocks (Wollenweber et al., 2010; Rezaeyan et al., 2015) and can be calculated using the equation (3).

$$HGC = \frac{P_{\mathrm{b}}}{(\rho_w - \rho_{\mathrm{og}})g} \tag{3}$$

where P_b is the breakthrough pressure (in MPa), ρ_w and ρ_{og} are the density of water and hydrocarbon (in g/cm^3), respectively, g is the acceleration of gravity (9.8 m/s^2).

The capacity of sealing natural gas of the carbonate cap rock can be expressed by the cover coefficient (*CC*) in specific traps (Cheng et al., 2006). A larger cover coefficient means a stronger capacity of the cap rock to seal the gas column, that is, a better sealing performance of the cap rock (Li et al., 1990). Accordingly, the *CC* can be calculated using the following equation (4).

$$CC = \frac{HGC}{Z} \times 100\% \quad (4)$$

CC is the cover coefficient (in %) and *Z* is the closure of the structure (in m).

4 Results

4.1 Petrology

Based on the petrographic analysis of thin sections, four main lithology types were defined for the studied cap rocks, namely (1) highly compacted peloidal packstone-grainstone, (2) highly cemented intraclastic-oolitic-bioclastic grainstone, (3) peloidal dolomitic limestone, and (4) incipiently dolomitized peloidal packstone-grainstone.

Type 1: Highly compacted peloidal packstone-grainstone is the predominant lithology type (Figure 5A) and is typically distributed in the upper part of the Yingshan Formation. It is very common in high-energy intraplatform shoal of open carbonate platform. This lithology type is composed of tightly packed peloids and deformed bioclast fragments. Medium- to coarse-sand-sized peloids vary in size from 0.25 to 0.58 mm and their content is 40.5% to 97.2% of the total rock volume. Bioclasts are not always easy to identify due to the following aspects: (1) the wide variety of broken shell morphologies and wall structures that form during subsidence and uplift, (2) the randomness of thin sections cut through complex shell forms, and (3) the presence of unstable minerals in various diagenetic alteration stages. Bioclast fragments only account on average for 2.8% (varying from 0.5% to 7.5%) of the rock volume. In addition, both the micrite crystals and calcite cements have a wider range of volumetric content, ranging from 0% to 25.4% and from 0% to 11.8%, respectively.

Type 2: Highly cemented intraclastic-oolitic-bioclastic grainstone is the second most abundant lithology type and is present in the lower and upper parts of the Yingshan Formation. It typically occurs in high-energy barrier shoals of restricted carbonate platforms and high-energy intraplatform shoals of open carbonate platforms. This lithology type includes poorly sorted intraclasts (Figure 5B), well-sorted ooids (Figure 5C) and bioclast fragments. These very fine- to coarse sand-sized grainstones are characterized by an average grain size ranging from 0.12 to 0.86 mm. Volumetrically, intraclastic grainstones occupy the most proportion within this lithology type, whereas oolitic grainstones and bioclastic grainstones are rare, only accounting for 5.1% and 2.5% or less, respectively. Cements are dominated by calcite and dolomitic crystals, with average volume percentages of 14.5% and 3.6%, respectively.

Type 3: Peloidal dolomitic limestone is the third most abundant lithology type and is restricted to the lower part of the Yingshan Formation (Figure 5D). It is very common in low-energy lagoons of restricted carbonate platforms. The dolomitic limestone encompasses peloidal wackestone and packstone. Fine- to coarse-sand-sized peloids range in size from 0.13 mm to 0.92 mm with an average of 0.49 mm. This lithology type is partly replaced by different types of dolomite crystals. Fine- to medium-crystalline dolomite crystals exhibit subhedral to anhedral shapes and vary in size from 0.12 to 0.45 mm with an average of 0.29 mm. Coarse-crystalline dolomite crystals are euhedral to subhedral rhombs in shape and range from 0.52 to 0.95 mm in size.

Type 4: Incipiently dolomitized peloidal packstone-grainstone is the least abundant of the lithology types and mainly occurs in the lower part of the Yingshan Formation (Figure 5E, F). It typically occurs in barrier shoals of restricted carbonate platforms. They are predominately supported by poorly sorted grains comprising peloids and minor intraclasts. The total volume of grains varies between 53.8% and 72.9% of the rock.

4.2 Pore types

Four pore types are identified through the combination of thin section observation and SEM analyses. They include microfractures, intercrystalline and intergranular pores, and dissolution vugs, and appear unevenly distributed in cap rock samples (Figures 5, 6). Microfractures account for 63.5% of the total pore volume, intercrystalline pores constitute 23.6%, and the rest of the pore space corresponds to intergranular pores and dissolution vugs.

Microfractures are abundant in highly cemented intraclastic-oolitic-bioclastic grainstones and peloidal dolomitic limestones, exhibiting a broad width range from

0.01 to 0.36 mm (average 0.18 mm) and a varied length range from 0.42 to 2.35 mm. Most microfractures are highly cemented by equant calcite crystals, and less commonly by anhedral dolomite crystals. Accordingly, some parts of microfractures are not cemented by calcite crystals and exhibit different isolated geometries (Figure 5G). The solution-enlarged intercrystalline pores are common in peloidal dolomitic limestones and incipiently dolomitized peloidal packstones (Figure 5H), and range in diameter from 0.02 to 8.23 μm with an average of 4.26 μm. These pores are partially or completely filled with calcite cement and clay minerals (e.g., illite) (Figure 6A). Intergranular pores with poor connectivity are predominant in highly cemented intraclastic-oolitic-bioclastic grainstones (Figure 6B). These intergranular pores are rarely observed since these pore spaces are dominantly occluded with drusy calcite cement and are highly compacted during burial. In addition, isolated dissolution vugs are locally observed and always have irregular geometries, showing different pore sizes from 2.6 to 10 μm.

4.3 Diagenetic phases

Diagenetic phases of carbonate cap rocks are mainly characterized by calcite cementation, dissolution, mechanical and chemical compaction, dolomitization and dedolomitization.

4.3.1 Calcite cementation

Calcite cement is an important and pervasive diagenetic product observed in most of the studied samples with the exception of those corresponding to peloidal dolomitic limestone. The volume percentage of calcite cement varies from only 3.6% in highly compacted peloidal packstone to almost 75.3% in intraclastic grainstone. It is characterized by four cement fabric types, including (1) isopachous crusts of bladed, (2) meniscus, (3) blocky and (4) drusy cements.

(1) Isopachous crusts of bladed cement formed around peloids and/or intraclasts (Figures 5D, 6C) and is commonly observed in intraclastic grainstone, with volumetric contents varying from 12.6% to 27.2% (with an average of 18.4%), as estimated from thin sections.

(2) Meniscus cement is commonly recognized in both highly compacted and highly cemented peloidal grainstone (Figure 6D), showing a curved surface in the grain boundaries.

(3) Blocky calcite cement is commonly formed by subhedral to anhedral crystals ranging from 0.08 μm to 1.23 mm in size. Intergranular pores are completely occluded by these blocky cements with medium-sized crystals (Figure 5B).

(4) Drusy cement is pervasively filling pores between peloids (Figure 6C). More than 93% of the secondary porosity is completely cemented in carbonate cap rocks intervals, compared to 4.8% of pores in oil-bearing reservoir intervals.

4.3.2 Dissolution

Fabric-selective dissolution is a common diagenetic process in highly compacted peloidal packstone-grainstone and highly cemented intraclastic-oolitic-bioclastic grainstone (Figure 5A), as revealed by the presence of enlarged intergranular and intercrystalline pores. Subsequently, this type of pore space was partially or completely filled with calcite cements. Nonfabric-selective dissolution primarily affected highly cemented intraclastic grainstone, highly compacted peloidal packstone-grainstone and incipiently dolomitized packstone, featuring the extensive formation of vugs and solution-enlarged microfractures. However, some microfractures with irregular shape appear completely filled with sparry calcite (Figure 6D), and some solution-enlargement microfractures are partially filled with calcite cements and appear discontinuous locally (Figure 5G).

4.3.3 Mechanical compaction

Mechanical compaction is easy to identify due to the presence of deformed intraclasts and rearranged ooids. It is quite common in highly cemented intraclastic-oolitic-bioclastic grainstone and incipiently dolomitized peloidal packstone-grainstone, and in peloidal dolomitic limestone in rare cases.

Two distinct characteristics of mechanical compaction are observed from thin section analysis: (1) cementation occurred before mechanical compaction, showing a large volume of calcite cements around grains with rare occurrence of point to linear contacts (Figure 5B). Intensive cementation resulted in a considerable decrease in primary porosity; (2) tight packing occurred before cementation, showing peloid deformation and ooid and/or bioclast rearrangement (Figure 5A). Peloids became more closely packed, exhibiting concave-convex contacts in tightly compacted zones (Figure 7A). In addition, some clay minerals were affected by plastic deformation in a way that they appear squeezed between grains. The intergranular porosity between intraclasts and peloids was reduced (Figure 6B), but new microfractures formed. Calcite cements infilling intergranular pores resisted grain deformation exerted by overlying sediment burden and contributed to the preservation of large pores during mechanical compaction.

4.3.4 Chemical compaction

Chemical compaction is widely observed in both highly cemented intraclastic-oolitic-bioclastic grainstone and highly compacted peloidal packstone-grainstone. Bedding-parallel stylolites have different amplitudes from several micrometers to tens of millimeters. According to the stylolite classification proposed by Koehn et al. (2016), three types of stylolites are recognized: suture and sharp peak (Figure 7B), seismogram pinning (Figure 7C), and simple wave-like. There are stylolites that dissolved calcite cement, matrix and lithologic interface of intraclastic grainstone and peloidal packstone-grainstone (Figure 7D, E). In addition, rhombic dolomite crystals appear distributed along or in the vicinity of a swarm of stylolites. Translucent brown to opaque pyrobitumen pervasively occludes pore networks (Figure 7E).

4.3.5 Dolomitization

Dolomitization is generally found in highly compacted peloidal packstone-grainstone containing bioclast fragments and also in peloidal dolomitic limestone, and is minor to absent in the other rock types. Dolomite occurs in the form of isolated medium to coarse rhombohedral crystals (Figure 5E). Medium-crystalline dolomite crystals resulting from calcite replacement range from 280-350 μm in diameter, and they are scattered in peloidal grainstone (Figure 7E). Coarse-crystalline dolomite crystals are in the range of 510-860 μm, and up to 1020 μm.

4.3.6 Dedolomitization

Dedolomitization is relatively weak with rare occurrence in peloidal dolomitic limestone. There are highly irregular patches of dolomite in coarse-crystalline limpid calcite due to dedolomitization imprints (Figure 7F). Dolomite crystals mainly have diameters of 80-120 μm, while calcite crystals resulting from dolomite calcitization are typically coarser, ranging from 80-230 μm in diameter. The elongated intercrystalline pores between calcite crystals are connected, with only a small portion being partially isolated.

4.4 HPMIP analysis

Table 1 shows a series of pore structure characterization parameters obtained from the HPMIP tests of 20 studied cap rock samples, including threshold pressure, maximum pore throat radius, median saturation capillary pressure, median pore throat radius, maximum mercury intrusion saturation, efficiency of mercury withdrawal, average pore throat radius, and skewness. In this study, the threshold capillary pressure, maximum mercury saturation and efficiency of mercury withdrawal have been chosen to show the differences between carbonate cap rocks. The differentiation has been carried out according to three aspects:

(1) The threshold pressure and maximum pore throat radius are two parameters that are inversely proportional. The threshold pressure is the minimum pressure for the nonwetting phase to be forced into the core and is also necessary to characterize the sealing capacity of cap rocks (Ito et al., 2011). The maximum pore throat radius is the radius corresponding to the threshold pressure.

(2) The median saturation capillary pressure and median pore throat radius are another two parameters that are inversely proportional. The median saturation capillary pressure refers to the capillary pressure at 50% accumulated mercury saturation. The median pore throat radius is the pore throat radius corresponding to the median pressure. However, the median saturation capillary pressure cannot be used because the accumulated mercury saturation in most rock samples is less than 50%. Hence, the maximum mercury saturation was chosen to evaluate the connectivity of the pore throat. A larger maximum mercury saturation corresponds to a larger portion of the pore throat volume of the rock that is saturated with mercury, indicating better connectivity of pore throats. The lower the maximum mercury saturation is, the worse the connectivity of pore throats (Qing et al., 2021).

(3) The efficiency of mercury withdrawal can reflect the geometry of the pore system (Wardlaw and Taylor, 1976). A high efficiency of mercury withdrawal indicates

a relatively small range of pore throat sizes and high pore accessibility, and vice versa (Mastalerz et al., 2021).

Four types (A, B, C, and D) of cap rocks can be recognized in accordance with the mercury-air capillary pressure curve (Figure 8).

(1) The threshold capillary pressure: High threshold pressures increase the difficulty for mercury to penetrate the pore systems during the mercury intrusion process. Type A curves reveal the tight nature of carbonate cap rocks. The average threshold pressure of the type A pore structure is generally higher than 11.25 MPa, and is thus significantly larger than those of the types B (1.72 MPa), C (1.20 MPa) and D (0.0125 MPa) pore structures, as revealed by the initial mercury intrusion stage (Figure 8). The threshold pressure difference between the four pore structure types indicates that the pore networks of type A are dominated by small pore throats, while large pores and smooth throats are rarely developed and not well interconnected. In terms of the morphological characteristics of capillary pressure curves, the curves corresponding to the types A, C and D show a steep slope and lack a horizontal stage in the intermediate mercury intrusion curve (Figure 8A, C, D). However, the type B curve shows a relatively horizontal stage with a gentle slope in this corresponding stage (Figure 8B), signifying that a large number of pores with a similar pore throat radii are intruded by mercury under a certain small pressure range.

(2) In terms of maximum mercury saturation (S_{max}), the type B carbonate cap rocks have the highest value (67.61%) at pressure as high as 116.67 MPa, followed by the

types D and A (27.71% and 20.9%, respectively). The type C cap rocks have the lowest maximum mercury saturation (5.08%), suggesting that micropores with complex pore structures are quite well developed in this carbonate cap rock type.

(3) Mercury extrusion process: the mercury extrusion curves of these four pore structure types in HPMIP tests are quite steep (Figure 8). The efficiency of mercury withdrawal, expressed in percentage, refers to the ratio of mercury saturation at the minimum pressure at the end of mercury extrusion process to the mercury saturation at the maximum pressure at the end of mercury intrusion process (Wardlaw and Taylor, 1976). The efficiency of mercury withdrawal in type C is higher (36.16%) than those of the other three types (A, B and D), which range from 15.14% to 19.37% (Figure 8C). This indicates that the cap rocks of type C have a smaller range of pore size distribution and better pore accessibility than the other types (A, B and D), which present larger range of pore size distribution and worse pore accessibility. Additionally, a volume of intruded mercury is still trapped in the pore spaces when the extrusion pressure almost returns to atmospheric pressure again (as low as 0.117 MPa).

4.5 Porosity and permeability

The studied carbonate cap rock samples have a wide range of porosities (Table 1), which range from 0.7% to 10.3% with an average of 1.57%. Permeability varies by two or three orders of magnitude, from 0.001×10^{-3} μm^2 to 2.15×10^{-3} μm^2 (0.00101-2.1783 md) with an average of 0.23×10^{-3} μm^2 (0.233 md). The cross-plot between porosity and permeability shows a poor correlation, with a low coefficient of determination (Figure 9). This indicates that the amount of porosity is not strongly correlated to permeability, and the pore networks of carbonate cap rocks are strongly heterogeneous and anisotropic.

4.6 Sealing capacity analysis

The sealing capacity of carbonate cap rocks can be defined by cover coefficients (Cheng et al., 2006), in a way that the larger the cover coefficients, the better the sealing capacity of the carbonate cap rocks and vice versa. Cover coefficients of well samples have a wide range, varying from 4.38% to 127.77% with an average of 27.23% (Figures 10A, C, Table 2). Cover coefficients of outcrop samples are relatively low, exhibiting a narrow variation from 3.90% to 5.71% with an average of 4.57% (Figures 10B, C). Average cover coefficients of well samples are almost six times as large as those of outcrop samples, indicating that well samples generally have better sealing capacity than the outcrop samples.

4.7 Carbonate cap rock classification

Based on the lithology, pore structure and diagenetic processes, the sealing capacity of carbonate cap rocks can be classified into four classes (Figure 11).

Class I carbonate cap rocks are characterized by the lowest porosity and permeability, highest threshold capillary pressure, and best sealing capacity in incipiently dolomitized peloidal packstone-grainstones and highly cemented intraclastic-oolitic-bioclastic grainstones (Figure 11A). Class I carbonate cap rocks correspond to the type A pore structure of the HPMIP analysis. The pore size distributions of class I rock samples show multimodal characteristics and mainly consist of micropores and transitional pores. There is a major pore throat peak with pore throat radii varying from 0.025 to 0.1 μm. The pore types are dominated by highly cemented intergranular and intercrystalline pores, and the samples are lacking open microfractures. Microfractures acting as fluid flow paths were completely occluded by blocky calcite cement. Together with intense mechanical compaction and abundant chemical compaction, calcite cementation occluded the original pore space, contributing to porosity reduction and the enhancement of the rock's sealing capacity.

Class II carbonate cap rocks show a high porosity with a large range, moderate permeability, relatively high capillary pressure, and a relatively good sealing capacity in highly cemented intraclastic-oolitic-bioclastic grainstones and peloidal dolomitic limestones (Figure 11B). Class II carbonate cap rocks correspond to the type B pore structure. Class II rocks are represented by a narrow range of transitional pores. The dominant pore radii of the samples of this class commonly presents a unimodal pore size distribution and have a relatively large proportion with a pore throat radius ranging from 0.025 to 0.25 μm. Pores are mainly disconnected microfractures, completely filled intergranular pores and rare dissolution vugs. However, dissolution and dolomitization occasionally led to the pore space enhancement for this class of cap rocks. Intense cementation and strong mechanical compaction, together with slight chemical compaction, effectively improved their sealing performance.

Class III carbonate cap rocks present moderate porosity, relatively low permeability, moderate threshold capillary pressure, and moderate sealing capacity in highly compacted peloidal packstone-grainstones and highly cemented intraclastic-oolitic-bioclastic grainstones (Figure 11C). Class III carbonate cap rocks correspond to the type C pore structure, which is dominated by transitional pores and mesopores of sizes ranging from 0.025 to 1 μm. No obvious radius peak indicates that there is poor pore size sorting for this class of cap rocks. Class III rock samples are dominated by partially occluded microfractures, isolated dissolution vugs, and minor scattered intergranular pores. This can be triggered by the combined effects of moderate cementation, mechanical compaction, and abundant chemical compaction. Moderate dissolution and scattered dolomitization increased the pore volume in a way that residual, incompletely filled microfractures are still available for fluid flow and hydrocarbon migration to some extent.

Class IV carbonate cap rocks exhibit low porosity, the highest permeability, the lowest threshold capillary pressure, and poor sealing capacity in highly compacted peloidal packstone-grainstones and peloidal dolomitic limestones (Figure 11D). Compared to the first three pore structure types, the type D pore structure corresponding to class IV carbonate cap rocks presents a unimodal pattern of macropores, with pore radii larger than 2.5 μm occupying 13.67% of the total volume. Minor cementation, moderate mechanical compaction and minor chemical compaction play a limited role in the porosity enhancement. Consequently, locally filled microfractures, partially occluded intercrystalline pores and minor dissolution vugs are dominant pore spaces in this class rocks. Intense dissolution and minor dolomitization are responsible for hydrocarbon loss.

5 Discussion

5.1 Paragenetic sequence

Common diagenetic imprints of carbonate rocks of the studied Ordovician succession have previously been recognized with the combination of geochemical data from published sources (Chen et al., 2003; Chen, 2004; Dong et al., 2013; Du et al., 2017; Han et al., 2019a). These authors inferred five major diagenetic environments for the Ordovician succession in the Tahe oilfield, including marine, meteoric, early shallow burial, epigenetic meteoric, and shallow – deep burial (Table 3). Based on C, O and Sr isotopes and fluid inclusions, Han et al. (2019a) inferred three types of diagenetic fluids: marine, meteoric, and formation waters. Three diagenetic stages were interpreted by studying the Tahe oilfield by Chen et al. (2014) comprising the penecontemporaneous-eogenetic-early mesogenetic, epigenetic, and early mesogenetic-late mesogenetic. In terms of outcrop studies, the diagenetic processes that the equivalent carbonate rocks underwent can be broadly divided into three stages: penecontemporaneous, burial, and epigenetic (Figure 12).

5.1.1 Penecontemporaneous stage

Diagenetic processes during this stage include calcite cementation, dissolution and dolomitization, which occurred at or near the time of sediment deposition. Fibrous to bladed cements with isopachous fringes are considered of early marine origin and are consistent with precipitation from seawater (Moore and Wade, 2013). This is because both the $\delta^{13}C$ and $\delta^{18}O$ values of isopachous calcite cements are close to the original isotopic composition of the Ordovician marine carbonates reported by Chen et al. (2003), with $\delta^{13}C$ from -3‰ to +1.0‰ VPDB, $\delta^{18}O$ from -9.8‰ to -5.6‰ VPDB, and homogenization temperature of fluid inclusion from 45.1 to 67.8℃ (Figure 13). In addition, the contents of other elements (e.g., B, Sr, Na) in cements are close to those of seawater (Table 3). These cements are mainly interpreted as a consequence of penecontemporaneous diagenesis.

Due to subaerial exposure, bioclast-bearing packstone containing abundant aragonite were prone to undergo dissolution. When these carbonates were exposed due to intermittent sea-level fluctuations at this stage, fabric-selective dissolution likely affected only a few unstable components under high water-rock ratios (Moore and Wade, 2013). Zhu et al. (2020) attributed this phenomenon to the short duration of exposure and the high frequency and small scale of the sea-level fluctuations. Effective pore space was created when carbonates were undersaturated with carbonate minerals. Subsequently, as one typical diagenetic product that formed in the vadose zone (Moore and Wade, 2013), meniscus cements have extremely low FeO, MnO, Na_2O, SrO and

BaO content, as tested by Chen (2004). This indicates that the meniscus cements precipitated under oxidizing conditions. Medium-crystalline dolomites appear dispersed in the micrite matrix rather than being plaque-like. These euhedral dolomite crystals are generally considered as the products of early dolomitization (Sibley and Gregg, 1987), indicating that the diagenetic fluid had a relatively low salinity and low temperature.

5.1.2 Burial stage

Diagenetic processes during this stage mainly include mechanical and chemical compaction, calcite cementation, and dolomitization. Burial diagenesis took place dominated by formation water, according to the negative $\delta^{18}O$, low $^{87}Sr/^{86}Sr$ values and low homogenization temperature of fluid inclusions tested by Han et al. (2019a).

Mechanical compaction is easier to identify in grainstones and packstones than in bioclast-bearing highly compacted peloidal packstone-grainstone. This is due to the presence of deformed intraclasts and rearranged ooids. Peloidal packstone-grainstone lithologies do not present clear indications of mechanical compaction except for the presence of deformed peloids and bioclast fragments. Chemical compaction induced by the weight of the overlying sediments is recognized from three types of stylolites: suture and sharp peak, seismogram pinning, and simple wave-like types (following the classification of Koehn et al., 2016). Carbonate minerals dissolved due to pressure solution could precipitate within stylolite porosity. Furthermore, as tested by Chen et al.

(2003), coarse-crystalline drusy calcite cements have $\delta^{13}C$ from +4.6‰ to +6.5‰ VPDB, $\delta^{18}O$ from -9.4‰ to -7.3‰ VPDB and homogenization temperature of fluid inclusion from 54.3 to 65.7℃. These cements are of shallow burial origin, precipitated from formation water and occluded intergranular pores and microfractures. In addition, burial dolomitization is pervasively developed with abundant coarse-crystalline dolomite crystals. However, critical data aiming at constraining their timing and further investigating dolomite origin are not available at present.

5.1.3 Epigenetic stage

The exposure of the studied carbonate strata in the outcrop sections is due to tectonic uplifting during the Indosian Orogeny (Kang, 1989). The diagenetic processes corresponding to this stage are nonfabric-selective dissolution, calcite cementation and dolomite calcitization (i.e., dedolomitization).

Nonfabric-selective dissolution resulted in the formation of secondary moldic and vuggy porosity with irregular geometries and simultaneously enlarged microfractures. Meniscus and pendant cement forms due to CO_2 loss and/or evaporation when meteoric water is saturated with respect to calcite in the meteoric vadose environment. Chen et al. (2003) reported that these blocky cements filled in microfractures and vugs are characterized by a relatively negative $\delta^{13}C$ composition ranging from -3.9‰ to -0.1‰ VPDB, a clear negative $\delta^{18}O$ signature ranging from -14‰ to -10‰ VPDB, and homogenization temperature of fluid inclusion ranging from 50.9 to 83℃ (Figure 13), and contain low B, Sr, and Na contents. This suggests that they are the products precipitated from meteoric water during the epigenetic stage. This interpretation is also supported by the work of Han et al. (2019a) in this study area, revealing a relatively high ratio of $^{87}Sr/^{86}Sr$ (0.709~0.709908) and low fluid inclusion homogenization temperature (<60°C to 90°C), as well as low salinity of the epigenetic meteoric water. Calcitization (dedolomitization) resulted in the formation of subhedral to anhedral calcite crystals, and poor connectivity of intercrystalline pores.

5.2 Conceptual model for pore evolution associated with diagenetic alterations and sealing capacity

On top of the depositional features of carbonate rocks, their pore evolution is affected by many other factors, including the properties of the pore fluids, the tectonic activity (which controls the amount and type of fractures) and the burial conditions (e.g., Melim et al., 2002; Javanbakht et al., 2018). Diagenetic alterations in different diagenetic stages have a key influence on the porosity and sealing capacity of carbonate cap rocks. Based on the petrological and petrophysical study presented here a conceptual model for pore evolution in relation to diagenesis and sealing capacity of carbonate cap rocks in the Yingshan Formation is presented (Figure 14).

5.2.1 Stage 1: Penecontemporaneous stage

During the deposition of the Yingshan Formation, the intergranular pores were occupied by saturated marine water, which favored the precipitation of calcite. Bladed cements with isopachous crusts formed the first generation of cement around intraclasts, ooids and peloids (Figure 14A). These cements partially or completely occluded the majority of intergranular pores. Subsequently, equant calcite crystals precipitated in part of these intergranular pores, coarsened towards the pore center, as the second generation of cement in the subsequent meteoric realm (Figure 14B).

Due to the intermittent relative sea-level falls during subaerial exposure, the rocks were periodically exposed to meteoric water during sea-level lowstands and thus subjected to meteoric dissolution in high-energy intraplatform shoals. Meteoric water influx resulted in the partial dissolution of grains (e.g., peloids, ooids, intraclasts, etc.) and contributed to the formation of dissolution vugs and moldic pores. Chen et al. (2003) confirmed that the cements that partially precipitated in the moldic secondary porosity in the study area are characterized by nonluminescent and extremely low FeO, MnO, Na_2O, SrO and BaO content. Accordingly, they were interpreted as cements originated from meteoric water. A similar phenomenon has been documented by He et al. (2010), who reported that dissolution vugs with different sizes and shapes occurred in high positions of carbonate platforms due to the subaerial exposure as eustatic fluctuations in seal level in the same study area. As highlighted by Du et al. (2017), fabric-selective dissolution preferentially resulted in the transformation of early aragonite cement or high-magnesium (i.e., unstable) calcite to low magnesium calcite and played a significant role in creating effective pore space when pore fluids were undersaturated with carbonate minerals. However, this porosity was not well preserved due to intense calcite cementation and restricted grain dissolution (Figure 14B). As noted by Chen (2004), the porosity of the rock in the penecontemporaneous stage showed a decreasing trend. Therefore, the sealing capacity of carbonate cap rocks was significantly enhanced.

5.2.2 Stage 2: First shallow to deep burial stage

The homogenization temperatures of fluid inclusions in calcite filling different dissolution vugs and microfractures indicate that the whole Yingshan Formation underwent two burial stages: shallow-intermediate burial (90℃~110℃) and intermediate-deep burial (110℃~140℃) (Han et al., 2019a). In the initial shallow burial stage, drusy calcite precipitation decreased the pore space by filling intergranular pores. Formation water with CO_2, H_2S and organic acids resulted in burial dissolution and later on limited burial dissolution created vugs locally. Two groups of north-northwest- and north-northeast-trending faults in the Akekule arch formed, controlled by the north – south weak compressive stress in the middle Caledonian Orogeny (Han, 2014). Meanwhile, microfractures also formed (Han et al., 2016) and were enlarged by nonfabric-selective dissolution (Figure 14C).

When the Yingshan Formation rocks were subjected to the overburden pressure resulting from progressive sedimentation, mechanical compaction resulted in a rock volume reduction, closer grain packing and the formation of sutured grain contacts. Partially spalled-off intraclasts highlight the strength of mechanical compaction (Figure 14D). The infilling in faults mainly affected the northern part of the Tahe oilfield, and was controlled by the paleogeomorphology (He et al., 2010). Light gray fine sandstones, gray-green mudstones and green-gray argillaceous siltstones are preferably filled in the highland of paleostructures or in positions corresponding to marked changes of slope. The rare earth element (REE) analysis performed by Yun (2009) showed that clay minerals were closely related to the sandstone of the Carboniferous Bachu Formation, indicating that infilling probably formed during the early Hercynian Orogeny. Clay minerals (e.g., filamentous illites) filling pores blocked pore throats and resulted in a significant reduction of the pore throat size (Figure 6A). The pore space in sedimentary rocks is very prone to reduction as a consequence of compaction associated with increasing burial depth (Cox et al., 2010). Increasing overburden pressure gave rise to an increase of sediment density and a reduction of intergranular porosity. Accordingly, mechanical compaction led to a slight decrease in porosity and permeability (Rustichelli, et al., 2013; Goulty et al., 2016), and correspondingly an increase in the sealing capacity of the cap rocks.

Carbonate cap rocks continued to be mechanically compacted due to the increasing effective stress. Following the initial shallow burial stage where mechanical compaction dominated, the variation of rock texture and mineralogy resulted in chemical compaction (Ishaq et al., 2019). Stylolites with various morphologies and amplitudes triggered by pressure solution were very commonly formed at the intermediate-deep burial stage. Dissolved carbonate minerals by pressure solution tended to precipitate locally rather than be transported from the stylolites, causing a porosity reduction of the cap rocks. Previously developed microfractures became cemented microfractures by later calcite filling. Parts of the dissolution vugs were occluded by blocky calcite cements (Figure 14E). A relatively small number of medium- to coarse-crystalline euhedral dolomite crystals appear distributed along or in the vicinity of stylolites. The first hydrocarbon charging phase took place in the middle to late Caledonian Orogeny (Figure 4, Chen et al., 2014). Based on the observations of cores and thin sections, fluorescence, electron probe, and Raman spectrum analyses, Chen and Huang (2004) and Abdurahman et al. (2010) interpreted that both tawny pyrobitumen and pyritized organic matter were concentrated within stylolites of the Ordovician carbonate rocks in this study area. Chen et al. (2014) confirmed the exact time of hydrocarbon charging, and revealed the pressure solution started earlier than hydrocarbon charging. In addition, the presence of pyrobitumen that precipitated occluding stylolite surfaces indicates these stylolites once acted as conduits for hydrocarbon migration. The dual behavior of stylolites as barriers and conduits for fluid flow has been reported in previous studies (Martín-Martín et al., 2018). Isolated pyrobitumen, together with drusy calcite cement, filled microfractures and vugs, thus increased the heterogeneity of pore structure and sealing capacity of cap rocks (Figure 14F).

5.2.3 Stage 3: Epigenetic exposure stage

During the middle Caledonian Orogeny and early Hercynian Orogeny, tectonic activity led to the uplift of Ordovician strata and the formation of major reverse, tensile and strike-slip faults (Kang, 2007; Han et al., 2015). The Yingshan Formation carbonate successions were exposed to the surface (Figure 4) and were subjected to meteoric water infiltration during subaerial exposure (Qi and Yun, 2010). Leaching and dissolution in relation to meteoric water with dissolved CO_2 preferentially occurred along large-scale faults and fractures (Han et al., 2019a, 2019b). The flow of freshwater along fractures favored the weathering and leaching of carbonate rocks. Abundant CO_2 from the atmosphere and soil contributed significantly to the formation of vugs with irregular geometries. Intensive water-rock interaction enlarged microfractures and dissolution vugs, which became the most abundant pore type in carbonate rocks. Some microfractures formed by decompression and cut the grains. The sealing performance of cap rocks was degraded in time as a result of the reactivation of faults by fluid overpressure due to multistage uplifting. This conclusion is supported by the works of Chiaramonte et al. (2008) and Espinoza and Santamarina (2017) that the presence of faults and fractures destroys the mechanical stability of the cap rock for hydrocarbon storage under geological timeframes. Therefore, microfractures between macropores characterized by high connectivity caused a considerable reduction of the rock's sealing capacity at these outcrop sections (Figure 14G).

5.2.4 Stage 4: Second shallow- to deep burial stage

Subsequently, the entire Yingshan Formation successions in the Tahe oilfield entered again into a long-term burial stage owing to subsidence (He et al., 2016). Another phase of chemical compaction took place with the increasing overburden pressure. Abundant dolomite crystals formed along stylolites (Figure 14H), controlled by pore fluids with variable chemistry and salinity and at different temperatures and pressures (Dong et al., 2013; Du et al., 2017). Two hydrocarbon charging events took place in the late Hercynian Orogeny and Himalayan Orogeny (Figure 4). The existence of paleo-oil reservoirs is supported by pervasive pore-filling bitumen. Insoluble residual bitumen as a result of thermal cracking of paleooil reservoirs had a significant impact on the reduction of porosity and permeability. Cao et al. (2015) demonstrated that the reduction of porosity and permeability is a consequence of the bitumen occlusion within microfractures and vugs. Although stylolites and microfractures provided fluid flow pathways, previously precipitated pyrobitumen completely prevented further transport of dissolved material, resulting in the cessation of chemical compaction (as suggested by the model of Morad et al., 2018). Therefore, the flow channels for later hydrocarbon charging were pervasively occluded, as it was already interpreted in previous studies (Wu et al., 2018b). Additionally, abundant blocky calcite cements have been interpreted as burial diagenetic products formed by leaching by meteoric water and presents the lowest $\delta^{13}C$ composition (ranging -6.4‰ to -1.7‰ VPDB), the lowest $\delta^{18}O$ (ranging from -15.4‰ to -13.7‰ VPDB), and the highest homogenization temperature (ranging from 95.5 to 104.6°C). This reveals that the fluids gradually changed from an open state to a semiclosed and closed state diagenetic system

(Chen et al., 2003). These cements completely filled the residual microfractures and dissolution pore networks. The paleo-oil accumulation as evidenced by pore- and stylolite-filling bitumen played a key role in reducing permeability (Wu et al., 2018b), thus enhancing the sealing capacity of cap rocks found in wells at a present-day burial depth of > 5000 m.

5.3 Controls of diagenesis on the rock's sealing potential

5.3.1 Sequence of compaction and cementation

Compaction and cementation are two remarkable diagenetic processes and their relative timing presents a variable influence on the sealing capacity of the studied cap rocks. Our data reveals two different situations:

(1) Cementation started earlier than compaction: calcite cementation can partially occur occluding intergranular porosity with a certain intensity in peloidal-intraclastic grainstones (Figure 15A) and prevent further diagenetic alterations of the rock (e.g., mechanical compaction), thus affecting the pore structures during progressive burial (Sfidari et al., 2019). Early calcite cement precipitation not only occludes all but small quantities of the intergranular porosity, it also provides a strong framework support for preventing the further loss of intergranular pore space to some extent (Adam et al., 2018; Morad et al., 2018). Such a result is observed from the presence of isolated pores and uncompacted rock components (e.g., intraclasts and peloids) (Figure 15B). Makhloufi et al. (2013) reported similar observations in situations where cementation took place

earlier than compaction, characterized by isopachous cements coating around the grains that serve as the stabilizing framework that prevents interpenetration during later compaction in the Oolithe Blanche Formation of the Paris Basin in France. In addition, this result is in agreement with the previous conclusions obtained by Makhloufi et al. (2013) and Amel et al. (2015), who showed that various types of grainstones with high porosity and permeability are still recognizable even when they underwent intense cementation. Large pore throat radii corresponding to relatively low-threshold capillary pressures indicate that cementation also probably offset porosity reduction caused by mechanical compaction. This is most likely due to the fact that partial intergranular pores are preserved through the inhibition of mechanical and chemical compaction (Amel et al., 2015; Dou et al., 2018; Liu and Xie, 2018; Regnet et al., 2019). Therefore, there is no significant enhancement of the sealing capacity of the cap rocks when cementation precedes compaction.

(2) Compaction started earlier than cementation: mechanical compaction can reduce to some extent the bulk rock volume during shallow burial (Kadkhodaie-Ilkhchi et al., 2019). Goldhammer (1997) documented that mechanical compaction in their case study initiates due to an overburden of a few hundred meters and ceases at burial depths of less than 2000 m. When the increasing effective stress caused by the weight of the overlying sediments exceeds the brittle strength of grains and matrix, rock components, such as peloids, intraclasts and ooids, are in touch with each other mainly in the form of point to linear contacts (Figure 15C). Intense grain deformation starts and some

grains are slightly spalled owing to severe mechanical compaction. Intergranular pore spaces are occluded due to the closer grain packing and breaking, as proven in the work of Goldhammer (1997), which showed that up to 38% pore space reduction can occur in compacted packstones and grainstones. Furthermore, overburden pressure by the weight of the overlying sediments contributes to the formation of cracks cross-cutting original microfractures, thereby forming individual microfracture segments in isolation. Chemical compaction triggered by the increasing overburden pressure partially or even completely obstructs the intergranular porosity. In addition, residual pyrobitumen distributed along or in the vicinity of stylolites can act as a barrier for fluid circulation (Wu et al., 2018b). Cementation following chemical compaction occurred in the form of blocky calcite crystals and contributed to achieving an almost total occlusion of pores (Figure 15D). This is consistent with the conclusions of Han et al (2019b), who showed that up to 95% of the pore space is occluded after various phases of calcite filling. The combined effect of compaction and cementation effectively plugged the pore throats and increased their tortuosity. The sequence of compaction and cementation has a considerable impact on the variation of sealing capacity. Those cap rocks that underwent compaction earlier than cementation always present higher threshold capillary pressure and smaller average pore throat radii than those that underwent cementation earlier than compaction.

5.3.2 Impact of microfracture and dissolution

The whole Yingshan Formation was uplifted and subjected to meteoric fluid leaching during the early Hercynian Orogeny (Chen, 2004; Han et al., 2019a). In general, the widespread leaching along faults and intensive dissolution generated porosity (Kang, 2007). During the uplift stage, pore systems of secondary origin formed due to the nonfabric-selective dissolution of unstable minerals as well as microfracture propagation (Figure 15E). Intense dissolution created a large volume of available pore spaces for the subsequent precipitation of calcite cement. As a whole, multiple generations of calcite cementation resulted in the reduction of vuggy porosity. Parts of the microfracture pore space are mainly filled with blocky and drusy sparry calcite cement (Figure 15B). However, effectively connected channels between intergranular, incompletely filled intercrystalline pores and separate vugs result from the presence of abundant microfractures (Figure 15F). These microfractures, which present various aperture widths (varying from 0.03 to 10.85 mm), generated less tortuous paths, which contributed to enhance the porosity and permeability of the cap rocks.

Fluids generally tend to percolate along large pore throats with a short flow path (Bihani and Daigle, 2019). Based on the analysis of aqueous inclusions and stable radioactive isotopes of Re-Os and K-Ar, Chen et al. (2014) demonstrated that the second hydrocarbon charging phase in the Tahe oilfield took place during the late Hercynian Orogeny (312.9-268.8 Ma). Potential hydrocarbon leakage by seepage through residual open microfractures takes place when the buoyancy pressure exceeds the capillary pressure of the rocks. In summary, microfractures played a role in connecting adjacent pore spaces that resulted in a medium threshold capillary pressure. This is disadvantageous for the sealing of underlying hydrocarbon reservoirs.

In addition, isolated dissolution pores could not improve the pore network connectivity and thus the rock's permeability (Honarmand and Amini, 2012; Javanbakht et al., 2018). Consequently, it is extremely difficult to enhance porosity without an efficient large-scale and efficient mass transport mechanism.

5.3.3 Impact of grain size and calcite cement

Four lithology types of carbonate cap rocks are characterized by ultralow porosity and permeability (Table 1). Figure 9 reveals that porosity has no positive relationship with permeability. Overall, the porosity of most of the rock samples tested are lower than 5%. Zhou et al. (2019) confirmed that the combined effects of microfractures and intercrystalline pores provide effective fluid pathways. Hence, peloidal dolomitic limestones containing microfractures always show low porosity and relatively high permeability. The average porosity and permeability of highly cemented intraclastic-oolitic-bioclastic grainstone cap rocks are lower than those of highly compacted peloidal packstone-grainstone cap rocks (Figure 16). This indicates that grainstones do not always present high porosity and permeability if they contain a wide volumetric variation of calcite cement content, which can be attributed to complex cementation processes (Heydari, 2000; Chen et al., 2003; Esrafili-Dizaji and Rahimpour-Bonab, 2009; Sfidari et al., 2019).

Furthermore, there is a good positive correlation between grain size and sealing capacity (defined by the cover coefficients) with a high coefficient of determination in grainstones (Figure 17). The porosity and permeability of grainstone cap rocks show a decreasing trend as grain size increases (Figure 17A, B, C). It is widely accepted that the coarser the grain size, the larger the pore throat. However, for the grainstone cap rocks with a wide volumetric variation of calcite cement, large grain size facilitates the large flow of cementing fluids, and hence more pore space could be cemented zones of calcite cements. The calcite cements pervasively occluded the pore networks and increase their tortuosity. This may be explained by the findings of Sutton et al. (2004), who suggested that large grains of carbonate cap rocks are enough to considerably increase the tortuosity of fluid flow paths in comparison with shale cap rocks that are composed of small clay particles. The study of Wu et al. (2018b) showed that a significant positive correlation exists between grain size and cement content, implying that grain size is a good indicator of the cement content in highly cemented intraclastic-oolitic-bioclastic grainstone cap rocks. A positive correlation between the rock's sealing capacity and the amount of carbonate cement indicates that cementation is a key factor that determines the rock's sealing potential. Honarmand and Amini (2012) stated that the content of calcite cement within grain-supported limestone has a significant impact on the petrophysical properties. Pervasive cementation results in a remarkable decrease of the pore volume and an increase of the pore throat heterogeneity. Permeability reduction by two orders of magnitude is triggered by the decrease of the pore throat size. On the basis of the relationship between capillary pressure and pore radius of the rock shown in the Washburn Equation (1), the capillary pressure increases with the pore size decrease. When the capillary pressure of the seal is greater than the upward buoyancy pressure exerted by the underlying fluid column, carbonate rocks with extremely small pore size can act as effective barriers for hydrocarbon migration thus allowing entrapment.

Accordingly, calcite cementation has positive but variable effects on the sealing capacity of carbonate cap rocks in nonporous tight zones, depending on the cement content. This finding is supported by Zhu et al. (2018), who stated that cementation contributed to the enhancement of sealing capacity in shale gas reservoirs.

5.3.4 Summary of how diagenesis affects the rock's sealing potential

The pore structure of carbonate cap rocks, whose evolution is controlled by complex diagenetic processes, has a profound effect on the heterogeneity of the rock's sealing capacity. In the marine diagenetic stage, the pore structures associated with diagenetic processes were largely governed by the original rock fabric and the depositional settings. Bladed cements with isopachous bladed crusts are ubiquitous in the barrier shoal and intraplatform shoal, where CO_2 degassing and high volume of seawater were flushed into the porous sediments due to the driving force from high tidal and wave energy (Madden and Wilson, 2013). On the one hand, this diagenetic process significantly contributed to the loss of primary porosity and the occurrence of tortuous pore throats. Furthermore, it caused a drastic enhancement of sealing capacity and increased resistance to further compaction between these grains during burial. Then, during the meteoric diagenetic stage, a minor fabric-selective dissolution phase preferentially affected sediments in the paleogeomorphic highlands, where the sediments were exposed to meteoric water. This diagenetic process caused a slight increase of porosity in the form of dissolution pores, but slightly reduced the rock's sealing capacity due to the limited diagenesis scales. Meanwhile, meniscus cements partially occluded the residual intergranular pores, causing a little increase of sealing potential. With progressive burial, mechanical compaction resulted in rapid porosity loss and the occurrence of heterogeneous pore throats, therefore enhancing the rock's sealing capacity. However, this diagenetic process also facilitated the formation of microfractures, which can act as fluid pathway and drastically increase the permeability of highly cemented intraclastic-oolitic-bioclastic grainstones. During epigenic karstification, intensive nonfabric-selective dissolution further enlarged the previous microfractures and dissolution vugs, particularly in the paleographic highlands where carbonates were preferentially exposed to the dissolution of undersaturated meteoric water. Enlarged microfractures acted as fluid pathways and the sealing capacity of cap rocks reduced. Chemical compaction provided an important source for late calcite cementation during another progressive burial stage. When the formation fluids are undersaturated in carbonates, particularly in some open microfractures and macropores, they have more effective fluid pressure release and rapid change, which is favorable to calcite precipitation (Zhou et al., 2018; Zhu et al., 2020). Most of the pore space, particularly in these enlarged microfractures, was considerably occluded by abundant blocky calcite cements. Although burial dissolution locally enlarged some small pores, there was no net porosity gain or loss for carbonate cap rocks. Scattered and disconnected residual pores without the connection of microfractures made little contribution to permeability and could not act as effective fluid flow or hydrocarbon migration paths. Therefore, poor connectivity and large tortuosity between these pore networks are responsible for the high sealing capacity of carbonate cap rocks.

Finally, in order to accurately predict the distribution of better carbonate cap rocks, further research work should be combined with sequence stratigraphy, depositional facies, and diagenetic alteration, which can be divided into the following steps: (1) establishing in more detail the sequence stratigraphic framework of the Yingshan Formation carbonates, including third- and fourth-order sequences; (2) characterizing the depositional facies and paragenetic sequence of diagenesis within the sequence stratigraphic framework, respectively; (3) revealing how the sequence stratigraphic framework controls the spatial and temporal distributions of the depositional facies and the variations of diagenetic alterations; (4) analyzing the impact of diagenesis within the sequence stratigraphic framework upon depositional facies and diagenetic alterations on the vertical and lateral distribution of better carbonate cap rocks, combined with previous findings of pore structure characterization and rock's sealing evaluation.

6 Conclusions

Carbonate cap rocks in the Ordovician Yingshan Formation comprises four lithology types: highly compacted peloidal packstone-grainstone, highly cemented intraclastic-oolitic-bioclastic grainstone, peloidal dolomitic limestone, and incipiently dolomitized peloidal packstone-grainstone. They present four pore types: microfractures, intercrystalline pores, intergranular pores, and dissolution vugs. The porosity for these carbonate cap rocks has poor correlation with permeability.

The major diagenetic processes that impacted the sealing capacity of carbonate cap rocks include calcite cementation (four calcite cement types), dissolution (fabric- and nonfabric-selective dissolution), mechanical and chemical compaction, dolomitization and dedolomitization. The pore network system of carbonate cap rocks was significantly affected by the subsequent modification of various diagenetic events. Based on the lithology, pore structure and diagenetic processes, the sealing capacity of carbonate cap rocks are classified into four classes. We propose a conceptual model for pore evolution in relation to the diagenetic evolution and sealing capacity of carbonate cap rocks in the Tarim Basin containing four stages: penecontemporaneous, first shallow- to deep burial, epigenetic exposure, and second shallow- to deep burial stage.

References

Abdurahman, A., J. Zhong, Y. Li, and X. Chen, 2010, Stylolite characteristics and petroleum geology significance of Ordovician carbonate rocks in Tahe Oilfield: Journal of China University of Petroleum, v. 34, no. 1, p. 7-12.

Adam, A., R. Swennen, W. Abdulghani, A. Abdlmutalib, M. Hariri, and A. Abdulraheem, 2018, Reservoir heterogeneity and quality of Khuff carbonates in outcrops of central Saudi Arabia: Marine and Petroleum Geology, v. 89, p. 721–751, doi:10.1016/j.marpetgeo.2017.11.010.

Al Khalifah, H., P. W. J. Glover, and P. Lorinczi, 2020, Permeability prediction and diagenesis in tight carbonates using machine learning techniques: Marine and Petroleum Geology, v. 112, no. 112, p. 104096, doi:10.1016/j.marpetgeo.2019.104096.

Ali, A., M. Wagreich, and M. Strasser, 2018, Depositional constraints and diagenetic pathways controlling petrophysics of Middle Miocene shallow-water carbonate reservoirs (Leitha limestones), Central Paratethys, Austria-Hungary: Marine and Petroleum Geology, v. 91, p. 586–598, doi:10.1016/j.marpetgeo.2018.01.031.

Al-Kharusi, A. S., and M. J. Blunt, 2008, Multiphase flow predictions from carbonate pore space images using extracted network models: Water Resources Research, v. 44, no. 6, p. 1-14, doi:10.1029/2006WR005695.

Amann-Hildenbrand, A., P. Bertier, A. Busch, and B. M. Krooss, 2013, Experimental investigation of the sealing capacity of generic clay-rich caprocks: International Journal of Greenhouse Gas Control, v. 19, p. 620–641, doi:10.1016/j.ijggc.2013.01.040.

Amel, H., A. Jafarian, A. Husinec, A. Koeshidayatullah, and R. Swennen, 2015, Microfacies, depositional environment and diagenetic evolution controls on the reservoir quality of the Permian Upper Dalan Formation, Kish Gas Field, Zagros Basin: Marine and Petroleum Geology, v. 67, p. 57–71, doi:10.1016/j.marpetgeo.2015.04.012.

Baqués, V., E. Ukar, S. E. Laubach, S. R. Forstner, and A. Fall, 2020, Fracture, Dissolution, and Cementation Events in Ordovician Carbonate Reservoirs, Tarim Basin, NW China: Geofluids, v. 2020, p. 1–28, doi:10.1155/2020/9037429.

Bera, B., N. S. K. Gunda, S. K. Mitra, and D. Vick, 2012, Characterization of Nanometer-Scale Porosity in Reservoir Carbonate Rock by Focused Ion Beam–Scanning Electron Microscopy: Microscopy and Microanalysis, v. 18, no. 1, p. 171–178, doi:10.1017/S1431927611012505.

Bihani, A., and H. Daigle, 2019, On the role of spatially correlated heterogeneity in determining mudrock sealing capacity for CO_2 sequestration: Marine and Petroleum Geology, v. 106, p. 116–127, doi:10.1016/j.marpetgeo.2019.04.038.

Boulin, P. F., P. Bretonnier, V. Vassil, A. Samouillet, M. Fleury, and J. M. Lombard, 2013, Sealing efficiency of caprocks: Experimental investigation of entry pressure measurement methods: Marine and Petroleum Geology, v. 48, p. 20–30, doi:10.1016/j.marpetgeo.2013.07.010.

Cao, T., Z. Song, S. Wang, X. Cao, Y. Li, and J. Xia, 2015, Characterizing the pore structure in the Silurian and Permian shales of the Sichuan Basin, China: Marine and Petroleum Geology, v. 61, p. 140–150, doi:10.1016/j.marpetgeo.2014.12.007.

Chen, H., Y. Wu, Y. Feng, Z. Lu, S. Hu, L. Yun, and L. Qi, 2014, Timing and Chronology of Hydrocarbon Charging in the Ordovican of Tahe Oilfield, Tarim Basin, NW China: Oil & Gas

Geology, v. 35, no. 6, p. 806-819.

Chen, N., J. Dong, S. Yang, J. Chen, Z. Li, and N. Ni, 2014, Restoration of geometry and emplacement mode of the Permian mafic dyke swarms in Keping and its adjacent areas of the Tarim Block, NW China: Lithos, v. 204, p. 73–82, doi:10.1016/j.lithos.2014.05.020.

Chen, Q., Y. Qian, H. Ma, and S. Wang, 2003, Diagenesis and porosity evolution of the Ordovician carbonate rocks in Tahe oilfield, Tarim Basin: Petroleum Geology & Expeximent, v. 25, no. 6, p. 729-734.

Chen, Q., and J. Huang, 2004, Hydrocarbon conduit systems and migration-accumulation model in Tahe Oilfield: Xinjiang Petroleum Geology, v. 25, no. 2, p. 143-146.

Chen, Q., Y. Zhao, G. Li, C. Chu, and B. Wang, 2012, Features and controlling factors of epigenic karstification of the Ordovician carbonates in Akekule arch, Tarim Basin: Journal of Earth Science, v. 23, no. 4, p. 506–515, doi:10.1007/s12583-012-0271-4.

Chen, Q., 2004, Diagenesis and porosity evolution of the Ordovician carbonate rocks in Tahe oilfield, Tarim Basin. China University of Geoscience (Wuhan), Wuhan, 51 p.

Cheng, Q., H. Chen, M. Fan, Q. Wang, and W. Chen, 2006, Determination of the total pore texture of caprock: Petroleum Geology & Experiment, vo. 28, no. 6, p. 604-608.

Chiaramonte, L., M. D. Zoback, J. Friedmann, and V. Stamp, 2008, Seal integrity and feasibility of CO_2 sequestration in the Teapot Dome EOR pilot: geomechanical site characterization: Environmental Geology, v. 54, no. 8, p. 1667–1675, doi:10.1007/s00254-007-0948-7.

Choquette, P. W., and L. C. Pray, 1970, Geologic Nomenclature and Classification of Porosity in Sedimentary Carbonates: AAPG Bulletin, v. 54, no. 2, p. 207-250, doi:10.1306/5D25C98B-16C1-11D7-8645000102C1865D.

Cox, P. A., R. A. Wood, J. A. D. Dickson, H. B. Al Rougha, H. Shebl, and P. W. M. Corbett, 2010, Dynamics of cementation in response to oil charge: Evidence from a Cretaceous carbonate field, U.A.E.: Sedimentary Geology, v. 228, no. 3–4, p. 246–254, doi:10.1016/j.sedgeo.2010.04.016.

Croizé, D., S. N. Ehrenberg, K. Bjørlykke, F. Renard, and J. Jahren, 2010, Petrophysical properties of bioclastic platform carbonates: implications for porosity controls during burial: Marine and Petroleum Geology, v. 27, no. 8, p. 1765–1774, doi:10.1016/j.marpetgeo.2009.11.008.

Daniel, R. F., and J. G. Kaldi, 2009, Evaluating seal capacity of cap rocks and intraformational barriers for CO_2 containment, in M. Grobe, J. C. Pashin, and R. L. Dodge, eds., Carbon dioxide sequestration in geological media—State of the science: AAPG Studies in Geology 59, p. 335–345, doi:10.1306/13171247St59227.

Ding, Z., R. Wang, F. Chen, J. Yang, Z. Zhu, Z. Yang, X. Sun, B. Xian, E. Li, T. Shi, C. Zuo, and Y. Li, 2020, Origin, hydrocarbon accumulation and oil-gas enrichment of fault-karst carbonate reservoirs: A case study of Ordovician carbonate reservoirs in South Tahe area of Halahatang oilfield, Tarim Basin: Petroleum Exploration and Development, v. 47, no. 2, p. 306–317, doi:10.1016/S1876-3804(20)60048-9.

Dong, S., D. Chen, H. Qing, X. Zhou, D. Wang, Z. Guo, M. Jiang, and Y. Qian, 2013, Hydrothermal alteration of dolostones in the Lower Ordovician, Tarim Basin, NW China: Multiple constraints from petrology, isotope geochemistry and fluid inclusion microthermometry: Marine and Petroleum Geology, v. 46, p. 270–286, doi:10.1016/j.marpetgeo.2013.06.013.

Dou, W., L. Liu, K. Wu, Z. Xu, X. Liu, and X. Feng, 2018, Diagenetic heterogeneity, pore throats characteristic and their effects on reservoir quality of the Upper Triassic tight sandstones of Yanchang Formation in Ordos Basin, China: Marine and Petroleum Geology, v. 98, p. 243-257, doi:10.1016/j.marpetgeo.2018.08.019.

Du, Y., T. Fan, and Z. Gao, 2016, Geochemical characteristics and their implications to diagenetic environment of Lower-Middle Ordovician carbonate rocks, Tarim Basin, China: A case study of Bachu Dabantage outcrop and Aksu Penglaiba outcrop: Natural Gas Geoscience, v. 27, no. 8, p. 1509-1523.

Du, Y., T. Fan, Z. Gao, H. Han, and Q. Zhang, 2017, Diagenesis and sequence stratigraphic framework of the Lower-Middle Ordovician Yingshan Formation, Tarim Basin: A case study from Tahe area and Keping-Bachu outcrop: Oil & Gas Geology, v. 38, no. 4, p. 677-692.

Dunham, R.J., 1962, Classification of carbonate rocks according to depositional textures: AAPG Memoir. v. 1, p. 108-121.

Ehrenberg, S. N., and H. Baek, 2019, Deposition, diagenesis and reservoir quality of an Oligocene reefal-margin limestone succession: Asmari Formation, United Arab Emirates: Sedimentary Geology, v. 393–394, p. 105535, doi:10.1016/j.sedgeo.2019.105535.

Espinoza, D. N., and J. C. Santamarina, 2017, CO_2 breakthrough—Caprock sealing efficiency and integrity for carbon geological storage: International Journal of Greenhouse Gas Control, v. 66, p. 218–229, doi:10.1016/j.ijggc.2017.09.019.

Esrafili-Dizaji, B., and H. Rahimpour-Bonab, 2009, Effects of depositional and diagenetic characteristics on carbonate reservoir quality: a case study from the South Pars gas field in the Persian Gulf: Petroleum Geoscience, v. 15, no. 4, p. 325–344, doi:10.1144/1354-079309-817.

Fusi, N., and J. Martinez-Martinez, 2013, Mercury porosimetry as a tool for improving quality of micro-CT images in low porosity carbonate rocks: Engineering Geology, v. 166, p. 272–282, doi:10.1016/j.enggeo.2013.10.002.

Fu, X., T. Wu, Y. Lü, S. Liu, H. Tian, and M. Lu, 2018, Research status and development trend of the reservoir caprock sealing properties: Oil & Gas Geology, v. 39, no. 3, p. 454-468.

Gao, H., D. He, X. Tong, Z. Wen, and Z. Wang, 2018, Tectonic-depositional environment and petroleum exploarion of Yingshan Formaiton in the Tarim Basin, Earth Science, v.43, no. 2, p. 551-465.

Garing, C., L. Luquot, P. A. Pezard, and P. Gouze, 2014, Electrical and flow properties of highly heterogeneous carbonate rocks: AAPG Bulletin, v. 98, no. 1, p. 49–66, doi:10.1306/05221312134.

Górniak, K., 2019, The cap rocks sealing the reservoir in the Węglówka oil field, sub-Silesian unit, Polish outer Carpathians: Petrographical approach: AAPG Bulletin, v. 103, no. 10, p. 2369–2398, doi:10.1306/01211917085.

Goldhammer, R. K., 1997, Compaction and decompaction algorithms for sedimentary carbonates: Journal of Sedimentary Research, v. 67, no. 1, p. 26-35, doi:10.1306/d42684e1-2b26-11d7-8648000102c1865d.

Goulty, N. R., C. Sargent, P. Andras, and A. C. Aplin, 2016, Compaction of diagenetically altered mudstones – Part 1: Mechanical and chemical contributions: Marine and Petroleum Geology, v. 77, p. 703–713, doi:10.1016/j.marpetgeo.2016.07.015.

Grove, C., and D. A. Jerram, 2011, jPOR: An ImageJ macro to quantify total optical porosity from blue-stained thin sections: Computers & Geosciences, v. 37, no. 11, p. 1850–1859, doi:10.1016/j.cageo.2011.03.002.

Han, C., 2014, Seismogeology of karst carbonate reservoir in 2th block of Ordovician Tahe Oilfield: Master Degree thesis, China University of Petroleum (East China).

Han, C., C. Lin, L. Ren, X. Lu, T. Wei, and X. Zhang, 2016, Characteristics of Ordovician fault in the Block 10 of Tahe Oilfield, Tarim Basin and its controlling factors on karst reservoirs: v. 27, no. 5, p. 790-798, doi:10.11764/j.issn.1672-1926.2016.05.0790.

Han, C., C. Lin, X. Lu, J. Tian, L. Ren, and C. Ma, 2019a, Petrological and geochemical constraints on fluid types and formation mechanisms of the Ordovician carbonate reservoirs in Tahe Oilfield, Tarim Basin, NW China: Journal of Petroleum Science and Engineering, v. 178, p. 106–120, doi:10.1016/j.petrol.2019.03.010.

Han, C., C. Lin, T. Wei, C. Dong, L. Ren, X. Zhang, L. Dong, and X. Zhao, 2019b, Paleogeomorphology restoration and the controlling effects of paleogeomorphology on karst reservoirs: a case study of an ordovician-aged section in Tahe oilfield, Tarim Basin, China: Carbonates and Evaporites, v. 34, no. 1, p. 31–44, doi:10.1007/s13146-017-0382-1.

Han, J., Q. Wang, J. Chen, C. Lin, Y. Song, J. Xu, H. Li, X. Xue, and Y. Wang, 2015, Carbonate sequence structure and microfacies distribution of the Middle and Lower Ordovician in northwestern Tarim Basin: Geoscience, v. 29, no. 3, p. 599-608.

He, Z., S. Peng, and T. Zhang, 2010, Controlling factors and genetic pattern of the Ordovician reservoirs in the Tahe area, Tarim Basin: Oil & Gas Geology, v. 31. no. 6, p. 743-752.

He, Z., X. Jin, Y. Wo, H. Li, Z. Bai, C. Jiao, and Z. Zhang, 2016, Hydrocarbon accumulation characteristics and exploration domains of ultra-deep marine carbonates in China: China Petroleum Exploration, v. 21, no. 1, p. 3–14.

Heydari, E., 2000, Porosity Loss, Fluid Flow, and Mass Transfer in Limestone Reservoirs: Application to the Upper Jurassic Smackover Formation, Mississippi1: AAPG Bulletin, v. 84, no. 1, p. 100-118, doi:10.1306/C9EBCD79-1735-11D7-8645000102C1865D.

Hollis, C., V. Vahrenkamp, S. Tull, A. Mookerjee, C. Taberner, and Y. Huang, 2010, Pore system characterisation in heterogeneous carbonates: An alternative approach to widely-used rock-typing methodologies: Marine and Petroleum Geology, v. 27, no. 4, p. 772–793, doi:10.1016/j.marpetgeo.2009.12.002.

Honarmand, J., and A. Amini, 2012, Diagenetic processes and reservoir properties in the ooid grainstones of the Asmari Formation, Cheshmeh Khush Oil Field, SW Iran: Journal of Petroleum Science and Engineering, v. 81, p. 70–79, doi:10.1016/j.petrol.2011.12.022.

Ishaq, M., I. U. Jan, M. Hanif, and M. Awais, 2019, Microfacies and diagenetic studies of the early Eocene Sakesar Limestone, Potwar Plateau, Pakistan: approach of reservoir evaluation using outcrop analogue: Carbonates and Evaporites, v. 34, no. 3, p. 623 – 656, doi:10.1007/s13146-018-0430-5.

Ito, D., K. Akaku, T. Okabe, T. Takahashi, and T. Tsuji, 2011, Measurement of threshold capillary pressure for seal rocks using the step-by-step approach and the residual pressure approach: Energy Procedia, v. 4, p. 5211–5218, doi:10.1016/j.egypro.2011.02.499.

Javanbakht, M., H. A. Wanas, A. Jafarian, N. Shahsavan, and M. Sahraeyan, 2018, Carbonate diagenesis in the Barremian-Aptian Tirgan formation (Kopet-Dagh basin, NE Iran): petrographic, geochemical and reservoir quality constraints: Journal of African Earth Sciences, v. 144, p. 122-135, doi: 10.1016/j.jafrearsci.2018.04.016.

Ji, C., H. Qing, D. Chen, P. Luo, Z. Jin, and L. Shao, 2013, Characteristics and dolomitization of upper cambrian to lower ordovician dolomite from outcrop in keping uplift, Western Tarim Basin, Northwest China: Acta Geologica Sinica (English Edition), v. 87, no. 4, p. 1005-1018, doi:10.1111/1755-6724.12106.

Jia, D., H. Lu, D. Cai, S. Wu, Y. Shi, and C. Chen, 1998, Structural Features of Northern Tarim Basin: Implications for Regional Tectonics and Petroleum Traps: AAPG Bulletin, v. 82, no. 1, p. 147-159, doi:10.1306/1D9BC3B3-172D-11D7-8645000102C1865D.

Jiang, H., Q. Chen, D. You, J. Huang, and Y. Chen, 2015, The different Ordovician sequence boundary's features and factors of Keping-Bachu Area in Tarim Basin: Xinjiang Geology, v. 33, no. 1, p. 84-89.

Jiang, L., R. H. Worden, C. F. Cai, A. J. Shen, X. Y. He, and L. Y. Pan, 2018, Contrasting diagenetic evolution patterns of platform margin limestones and dolostones in the Lower Triassic Feixianguan Formation, Sichuan Basin, China: Marine and Petroleum Geology, v. 92, p. 332–351, doi:10.1016/j.marpetgeo.2017.10.029.

Kadkhodaie-Ilkhchi, R., A. Kadkhodaie, R. Rezaee, and V. Mehdipour, 2019, Unraveling the reservoir heterogeneity of the tight gas sandstones using the porosity conditioned facies modeling in the Whicher Range field, Perth Basin, Western Australia: Journal of Petroleum Science and Engineering, v. 176, p. 97–115, doi:10.1016/j.petrol.2019.01.020.

Kaldi, J., R. Daniel, E. Tenthorey, K. Michael, U. Schacht, A. Nicol, J. Underschultz, and G. Backe, 2013, Containment of CO_2 in CCS: Role of caprocks and faults: Energy Procedia, v. 37, p. 5403–5410, doi:10.1016/j.egypro.2013.06.458.

Kang, Y., 1989, Dissolution on several petro-geological problems in the Northern Tarim Basin: Geoscience, v. 3, no. 1, p. 111-123.

Kang, Y., 2007, Review and revelation of oil/gas discoveries in the Paleozoic marine strata of China: Oil & Gas Geology, v. 28, no. 5, p. 570-575.

Kim, K., Y. Lee, S. Hwang, J. Seo, and W. Sung, 2011, Improved capillary pressure model considering dual-pore geometry system in carbonate reservoirs: Journal of Petroleum Science and Engineering, v. 78, no. 3–4, p. 601–608, doi:10.1016/j.petrol.2011.08.004.

Koehn, D., M. P. Rood, N. Beaudoin, P. Chung, P. D. Bons, and E. Gomez-Rivas, 2016, A new stylolite classification scheme to estimate compaction and local permeability variations: Sedimentary Geology, v. 346, p. 60–71, doi:10.1016/j.sedgeo.2016.10.007.

Lai, J., G. Wang, Z. Wang, J. Chen, X. Pang, S. Wang, Z. Zhou, Z. He, Z. Qin, and X. Fan, 2018, A review on pore structure characterization in tight sandstones: Earth-Science Reviews, v. 177, p. 436–457, doi:10.1016/j.earscirev.2017.12.003.

Li, P., M. Zheng, H. Bi, S. Wu, and X. Wang, 2017a, Pore throat structure and fractal characteristics of tight oil sandstone: A case study in the Ordos Basin, China: Journal of Petroleum Science and Engineering, v. 149, p. 665–674, doi:10.1016/j.petrol.2016.11.015.

Li, X., X. Dai, W. Zhang, and W. Xiao, 1990, Cap assessment and genetic mechanism of isolated island shallow gas pools: Experimental Petroleum Geology, v. 12, no. 3, p. 307-315.

Li, Y., X. Chang, W. Yin, T. Sun, and T. Song, 2017b, Quantitative impact of diagenesis on reservoir quality of the Triassic Chang 6 tight oil sandstones, Zhenjing area, Ordos Basin, China: Marine and Petroleum Geology, v. 86, p. 1014–1028, doi:10.1016/j.marpetgeo.2017.07.005.

Li, Y., X. Chang, W. Yin, G. Wang, Jinliang Zhang, B. Shi, Jianhua Zhang, and L. Mao, 2019, Quantitative identification of diagenetic facies and controls on reservoir quality for tight sandstones: A case study of the Triassic Chang 9 oil layer, Zhenjing area, Ordos Basin: Marine and Petroleum Geology, v. 102, p. 680–694, doi:10.1016/j.marpetgeo.2019.01.025.

Li, Z., S. Wu, D. Xia, X. Zhang, and M. Huang, 2017c, Diagenetic alterations and reservoir heterogeneity within the depositional facies: A case study from distributary-channel belt sandstone of Upper Triassic Yanchang Formation reservoirs (Ordos Basin, China): Marine and Petroleum Geology, v. 86, p. 950–971, doi:10.1016/j.marpetgeo.2017.07.002.

Lin, Z., 2002, Carbonate rock reservoir features and oil-gas accumulating conditions in the Ordovician of Tahe oilfield in Northern Tarim Basin: Acta Petrolei Sinica, v. 23, no. 3, p. 23-26, 27.

Liu, C., and Q. Xie, 2018, Depositional, sedimentary, and diagenetic controls on reservoir quality in carbonate successions: A case study from the carbonate gas reservoirs of the Lower Triassic Feixianguan Formation, eastern Sichuan Basin, China: Journal of Petroleum Science and Engineering, v. 163, p. 484–500, doi:10.1016/j.petrol.2017.12.063.

Liu, J., Z. Li, L. Cheng, and J. Li, 2017, Multiphase Calcite Cementation and Fluids Evolution of a Deeply Buried Carbonate Reservoir in the Upper Ordovician Lianglitag Formation, Tahe Oilfield, Tarim Basin, NW China: Geofluids, v. 2017, p. 1–19, doi:10.1155/2017/4813235.

Lohr, C. D., and P. C. Hackley, 2018, Using mercury injection pressure analyses to estimate sealing capacity of the Tuscaloosa marine shale in Mississippi, USA: Implications for carbon dioxide sequestration: International Journal of Greenhouse Gas Control, v. 78, p. 375–387, doi:10.1016/j.ijggc.2018.09.006.

Longman, M. W., 1980, Carbonate diagenetic textures from nearsurface diagenetic environments: AAPG Bulletin, v. 64, no. 4, p. 461-487, doi:10.1306/2F918A63-16CE-11D7-8645000102C1865D.

Lü, X., Y. Wang, H. Yu, and Z. Bai, 2017, Major factors affecting the closure of marine carbonate caprock and their quantitative evaluation: A case study of Ordovician rocks on the northern slope of the Tazhong uplift in the Tarim Basin, western China: Marine and Petroleum Geology, v. 83, p. 231–245, doi:10.1016/j.marpetgeo.2017.03.006.

Ma, Y., D. He, X. Cai, and B. Liu, 2017, Distribution and fundamental science questions for petroleum geology of marine carbonate in China: Acta Petrologica Sinica, v. 33, no. 4, p. 1007-1020.

Madden, R. H. C., and M. E. J. Wilson, 2013, Diagenesis of a SE Asian Cenozoic carbonate platform margin and its adjacent basinal deposits: Sedimentary Geology, v. 286–287, p. 20–38, doi:10.1016/j.sedgeo.2012.11.006.

Makhloufi, Y., P. Y. Collin, F. Bergerat, L. Casteleyn, S. Claes, C. David, B. Menendez, F. Monna, P. Robion, J. Sizun, R. Swennen, and C. Rigollet, 2013, Impact of sedimentology and diagenesis on the petrophysical properties of a tight oolitic carbonate reservoir. The case of the Oolithe Blanche Formation (Bathonian, Paris Basin, France): Marine and Petroleum Geology,

v. 48, p. 323–340, doi:10.1016/j.marpetgeo.2013.08.021.

Martín-Martín, J. D., E. Gomez-Rivas, T. Bover-Arnal, A. Travé, R. Salas, J. A. Moreno-Bedmar, S. Tomás, M. Corbella, A. Teixell, J. Vergés, and S. L. Stafford, 2013, The Upper Aptian to Lower Albian syn-rift carbonate succession of the southern Maestrat Basin (Spain): Facies architecture and fault-controlled stratabound dolostones: Cretaceous Research, v. 41, p. 217–236, doi:10.1016/j.cretres.2012.12.008.

Martín-Martín, J. D., E. Gomez-Rivas, D. Gómez-Gras, A. Travé, R. Ameneiro, D. Koehn, and P. D. Bons, 2018, Activation of stylolites as conduits for overpressured fluid flow in dolomitized platform carbonates: Geological Society, London, Special Publications, v. 459, no. 1, p. 157–176, doi:10.1144/SP459.3.

Mastalerz, M., A. Drobniak, and J. C. Hower, 2021, Controls on reservoir properties in organic-matter-rich shales: Insights from MICP analysis: Journal of Petroleum Science and Engineering, v. 196, p. 1-11. doi: 10.1016/j.petrol.2020.107775.

Mayo, S., M. Josh, Y. Nesterets, L. Esteban, M. Pervukhina, M. Ben Clennell, A. Maksimenko, and C. Hall, 2015, Quantitative micro-porosity characterization using synchrotron micro-CT and xenon K-edge subtraction in sandstones, carbonates, shales and coal: Fuel, v. 154, p. 167–173, doi:10.1016/j.fuel.2015.03.046.

Mazzullo, S. J., 1981, Facies and burial diagenesis of a carbonate reservoir: Chapman Deep (Atoka) Field, Delaware Basin, Texas: AAPG Bulletin, v. 65, no. 5, p. 850-865, doi:10.1306/2F919B16-16CE-11D7-8645000102C1865D.

Melim, L. A., H. Westphal, P. K. Swart, G. P. Eberli, and A. Munnecke, 2002, Questioning carbonate diagenetic paradigms: evidence from the Neogene of the Bahamas: Marine Geology, v. 185, no. 1–2, p. 27–53, doi:10.1016/S0025-3227(01)00289-4.

Melim, L. A., F. S. Anselmetti, and G. P. Eberli, 2001, The importance of pore type on permeability of Neogene carbonates, Great Bahama Bank, In Ginsburg, RN (ed) Subsurface geology of a prograding carbonate platform margin, Great Bahama Bank: Results of the Bahamas drilling project: SEPM Special Publication, no. 70, p. 217–240.

Moore, C. H., 2001, Carbonate reservoirs. Porosity evolution and diagenesis in a sequence stratigraphic framework, Elsevier, 443 p.

Moore, C. H., and W. J. Wade, 2013, Carbonate reservoirs: Porosity and diagenesis in a sequence stratigraphic framework, Elsevier, 374 p.

Morad, D., F. H. Nader, M. Gasparrini, S. Morad, C. Rossi, E. Marchionda, F. Al Darmaki, M. Martines, and H. Hellevang, 2018, Comparison of the diagenetic and reservoir quality evolution between the anticline crest and flank of an Upper Jurassic carbonate gas reservoir, Abu Dhabi, United Arab Emirates: Sedimentary Geology, v. 367, p. 96–113, doi:10.1016/j.sedgeo.2018.02.008.

Münch, B., and L. Holzer, 2008, Contradicting Geometrical Concepts in Pore Size Analysis Attained with Electron Microscopy and Mercury Intrusion: Journal of the American Ceramic Society, v. 91, no. 12, p. 4059–4067, doi:10.1111/j.1551-2916.2008.02736.x.

Norbisrath, J. H., G. P. Eberli, B. Laurich, G. Desbois, R. J. Weger, and J. L. Urai, 2015, Electrical and fluid flow properties of carbonate microporosity types from multiscale digital image analysis and mercury injection: AAPG Bulletin, v. 99, no. 11, p. 2077–2098, doi:10.1306/07061514205.

Nourollah, H., and M. Urosevic, 2019, Evaluation of sealing potential near gas chimneys–the Gippsland Basin, Australia: Journal of Applied Geophysics, v. 160, p. 254–263, doi:10.1016/j.jappgeo.2018.11.019.

Okabe, H., and M. J. Blunt, 2007, Pore space reconstruction of vuggy carbonates using microtomography and multiple-point statistics: Water Resources Research, v. 43, no. 12, doi:10.1029/2006WR005680.

Oluwadebi, A. G., K. G. Taylor, and P. J. Dowey, 2018, Diagenetic controls on the reservoir quality of the tight gas Collyhurst Sandstone Formation, Lower Permian, East Irish Sea Basin, United Kingdom: Sedimentary Geology, v. 371, p. 55–74, doi:10.1016/j.sedgeo.2018.04.006.

Qi, L., and L. Yun, 2010, Development characteristics and main controlling factors of the Ordovician carbonate karst in Tahe oilfield: Oil & Gas Geology, v. 31, no. 1, p. 1-12.

Qing, F., J. Yan, J. Wang, Q. Hu, M. Wang, B. Geng, and J. Chao, 2021, Pore structure and fluid saturation of near-oil source low-permeability turbidite sandstone of the Dongying Sag in the Bohai Bay: Journal of Petroleum Science and Engineering, v. 196, p. 1-19, doi: 10.1016/j.petrol.2020.108106.

Regnet, J. B., C. David, P. Robion, and B. Menéndez, 2019, Microstructures and physical properties in carbonate rocks: A comprehensive review: Marine and Petroleum Geology, v. 103, p. 366–376, doi:10.1016/j.marpetgeo.2019.02.022.

Rezaeyan, A., S. A. Tabatabaei-Nejad, E. Khodapanah, and M. Kamari, 2015, A laboratory study on capillary sealing efficiency of Iranian shale and anhydrite caprocks: Marine and Petroleum Geology, v. 66, p. 817–828, doi:10.1016/j.marpetgeo.2015.07.022.

Roehl, P. O., and P. W. Choquette, 1990, Carbonate petroleum reservoirs: Sedimentary Geology, v. 66, no. 3–4, p. 305, doi:10.1016/0037-0738(90)90081-4.

Ruan, Z., B. Yu, and Y. Chen, 2013, Application of fluid inclusion analysis for buried dissolution predicting in the Tahe Oilfield of Tarim Basin, NW China: Journal of Earth Science, v. 24, no. 3, p. 343–354, doi:10.1007/s12583-013-0338-x.

Rustichelli, A., E. Tondi, F. Agosta, C. Di Celma, and M. Giorgioni, 2013, Sedimentologic and diagenetic controls on pore-network characteristics of Oligocene–Miocene ramp carbonates (Majella Mountain, central Italy): AAPG Bulletin, v. 97, no. 3, p. 487–524, doi:10.1306/07311212071.

Sakhaee-Pour, A., and S. L. Bryant, 2014, Effect of pore structure on the producibility of tight-gas sandstones: AAPG Bulletin, v. 98, no. 4, p. 663–694, doi:10.1306/08011312078.

Schlömer, S., and B. M. Krooss, 1997, Experimental characterisation of the hydrocarbon sealing efficiency of cap rocks: Marine and Petroleum Geology, v. 14, no. 5, p. 565–580, doi:10.1016/S0264-8172(97)00022-6.

Schmitt, M., C. P. Fernandes, J. A. B. da Cunha Neto, F. G. Wolf, and V. S. S. dos Santos, 2013, Characterization of pore systems in seal rocks using Nitrogen Gas Adsorption combined with Mercury Injection Capillary Pressure techniques: Marine and Petroleum Geology, v. 39, no. 1, p. 138–149, doi:10.1016/j.marpetgeo.2012.09.001.

Schowalter, T. T., 1979, Mechanics of Secondary Hydrocarbon Migration and Entrapment: AAPG Bulletin, v. 63, no. 5, p. 723-760, doi:10.1306/2F9182CA-16CE-11D7-8645000102C1865D.

Sfidari, E., A. Amini, A. Kadkhodaie-Ilkhchi, A. Chehrazi, and S. M. Zamanzadeh, 2019, Depositional facies, diagenetic overprints and sequence stratigraphy of the upper Surmeh reservoir (Arab Formation) of offshore Iran: Journal of African Earth Sciences, v. 149, p. 55–71, doi:10.1016/j.jafrearsci.2018.07.025.

Sibley, D. F., and J. M. Gregg, 1987, Classification of dolomite rock textures: Journal of Sedimentary Research, v. 57, no. 6, p. 967-975, doi:10.1306/212F8CBA-2B24-11D7-8648000102C1865D.

Sok, R. M., T. Varslot, A. Ghous, S. Latham, A. P. Sheppard, and M. A. Knackstedt, 2010, Pore scale characterization of carbonates at multiple scales: Integration of micro-CT, BSEM, and FIBSEM, in Petrophysics, v. 51, no. 6, p. 1-12.

Song, Z., G. Liu, W. Yang, H. Zou, M. Sun, and X. Wang, 2018, Multi-fractal distribution analysis for pore structure characterization of tight sandstone—A case study of the Upper Paleozoic tight formations in the Longdong District, Ordos Basin: Marine and Petroleum Geology, v. 92, p. 842–854, doi:10.1016/j.marpetgeo.2017.12.018.

Sutton, S. J., F. G. Ethridge, W. R. Almon, W. C. Dawson, and K. K. Edwards, 2004, Textural and sequence-stratigraphic controls on sealing capacity of Lower and Upper Cretaceous shales, Denver basin, Colorado: AAPG Bulletin, v. 88, no. 8, p. 1185–1206, doi:10.1306/02210403081.

Tang, W., and M. Li, 2020, Scalable double regularization for 3D Nano-CT reconstruction: Journal of Petroleum Science and Engineering, v. 192, p. 107271, doi:10.1016/j.petrol.2020.107271.

Teillet, T., F. Fournier, F. Gisquet, L. F. Montaggioni, J. Borgomano, Q. Villeneuve, and F. Hong, 2019, Diagenetic history and porosity evolution of an Early Miocene carbonate buildup (Upper Burman Limestone), Yadana gas field, offshore Myanmar: Marine and Petroleum Geology, v. 109, p. 589–606, doi:10.1016/j.marpetgeo.2019.06.044.

Tian, F., Q. Jin, X. Lu, Y. Lei, L. Zhang, S. Zheng, H. Zhang, Y. Rong, and N. Liu, 2016, Multi-layered ordovician paleokarst reservoir detection and spatial delineation: A case study in the Tahe Oilfield, Tarim Basin, Western China: Marine and Petroleum Geology, v. 69, p. 53–73, doi:10.1016/j.marpetgeo.2015.10.015.

Van Geet, M., R. Swennen, and M. Wevers, 2000, Quantitative analysis of reservoir rocks by microfocus X-ray computerised tomography: Sedimentary Geology, v. 132, no. 1–2, p. 25–36, doi:10.1016/S0037-0738(99)00127-X.

Vavra, C., J. G. Kaldi, and R. M. Sneider, 1992, Geological Applications of Capillary Pressure: A Review (1): AAPG Bulletin, v. 76, no. 6, p. 840-850, doi:10.1306/BDFF88F8-1718-11D7-8645000102C1865D.

Wang, G., P. Li, F. Hao, H. Zou, L. Zhang, and X. Yu, 2015, Impact of sedimentology, diagenesis, and solid bitumen on the development of a tight gas grainstone reservoir in the Feixianguan Formation, Jiannan area, China: Implications for gas exploration in tight carbonate reservoirs: Marine and Petroleum Geology, v. 64, p. 250–265, doi:10.1016/j.marpetgeo.2015.02.045.

Wang, Q., C. Lin, H. Li, J. Han, Y. Sun, and H. He, 2018, Carbonate sedimentary microfacies characteristics and evolution of the Middle and Lower Ordovician in northestern of Tarim Basin: Nature Gas Geoscience, v. 29, no. 9, p. 1274-1288.

Wang, Q., J. Han, H. Li, Y. Sun, H. He, and S. Ren, 2019, Carbonate sequence architecture, sedimentary evolution and sea level fluctuation of the Middle and Lower Ordovician on outcrops at the northwestern margin of Tarim Basin: Oil & Gas Geology, v. 40, no. 4, p. 835-850, 916.

Wang, R., X. Zhu, Y. Chen, and K. Li, 2012, Diagenesis and reservoir characteristics of the Lower-Middle Carboniferous carbonates in Kenkyak area, Pre-Caspian Basin: Oil & Gas Geology, v. 33, no. 2, p. 225-235.

Wang, Y., and J. D. Miller, 2020, Current developments and applications of micro-CT for the 3D analysis of multiphase mineral systems in geometallurgy: Earth-Science Reviews, in press, doi: 10.1016/j.earscirev.2020.103406.

Wardlaw, N. C., and R. P. Taylor, 1976, Mercury capillary pressure curves and the interpretation of pore structure and capillary behavior in reservoir rocks: Bullentin of Canadian Petroleum Geology, v. 24, no. 2, p. 225-262.

Washburn, E. W., 1921, The Dynamics of Capillary Flow: Physical Review, v. 17, no. 3, p. 273–283, doi:10.1103/PhysRev.17.273.

Watts, N. L., 1987, Theoretical aspects of cap-rock and fault seals for single- and two-phase hydrocarbon columns: Marine and Petroleum Geology, v. 4, no. 4, p. 274–307, doi:10.1016/0264-8172(87)90008-0.

Wollenweber, J., S. Alles, A. Busch, B. M. Krooss, H. Stanjek, and R. Littke, 2010, Experimental investigation of the CO2 sealing efficiency of caprocks: International Journal of Greenhouse Gas Control, v. 4, no. 2, p. 231–241, doi:10.1016/j.ijggc.2010.01.003.

Wu, J., T. Fan, Z. Gao, Y. Gu, J. Wang, Y. Du, C. Li, S. Wang, C. Zhang, M. Meng, D. Wei, and H. Fan, 2018a, Identification and characteristic analysis of carbonate cap rock: A case study from the Lower-Middle Ordovician Yingshan Formation in Tahe oilfield, Tarim Basin, China: Journal of Petroleum Science and Engineering, v. 164, p. 362–381, doi:10.1016/j.petrol.2017.12.070.

Wu, J., T. Fan, Z. Gao, X. Yin, X. Fan, C. Li, W. Yu, C. Li, C. Zhang, J. Zhang, and X. Sun, 2018b, A conceptual model to investigate the impact of diagenesis and residual bitumen on the characteristics of Ordovician carbonate cap rock from Tarim Basin, China: Journal of Petroleum Science and Engineering, v. 168, p. 226–245, doi:10.1016/j.petrol.2018.05.034.

Wu, J., T. Fan, E. Gomez-Rivas, Z. Gao, S. Yao, W. Li, C. Zhang, Q. Sun, Y. Gu, and M. Xiang, 2019, Impact of pore structure and fractal characteristics on the sealing capacity of Ordovician carbonate cap rock in the Tarim Basin, China: Marine and Petroleum Geology, v. 102, p. 557–579, doi:10.1016/j.marpetgeo.2019.01.014.

Wu, J., T. Fan, E. Gomez-Rivas, A. Travé, Z. Gao, S. Wang, and X. Sun, 2021, Fractal characteristics of pore networks and sealing capacity of Ordovician carbonate cap rocks: A case study based on outcrop analogues from the Tarim Basin, China: AAPG Bulletin, v. 105, no. 2, p. 437-479, doi: 10.1306/03172019022.

Xiao, D., S. Jiang, D. Thul, W. Huang, Z. Lu, and S. Lu, 2017, Combining rate-controlled porosimetry and NMR to probe full-range pore throat structures and their evolution features in tight sands: A case study in the Songliao Basin, China: Marine and Petroleum Geology, v. 83, p. 111–123, doi:10.1016/j.marpetgeo.2017.03.003.

Xoaoth, B.B., 1966. Coal and gas outburst. In: Song, S., Wang, Y. (Eds.), Translation, Beijing, China Industry Press.

Xu, K., S. Liu, and B. Yu, 2012, Reef-Flat Complex Sedimentary Characteristics of Middle Ordovician Yijianfang Formation in Bachu Area, Tarim Basin: Xinjiang Petroleum Geology, v. 23, no. 5, p. 536-539.

Yang, S.-F., Z. Li, H. Chen, M. Santosh, C.-W. Dong, and X. Yu, 2007, Permian bimodal dyke of Tarim Basin, NW China: Geochemical characteristics and tectonic implications: Gondwana Research, v. 12, no. 1–2, p. 113–120, doi:10.1016/j.gr.2006.10.018.

Yang, X., Y, Ran, F. Song, X. Xu, J, Cheng, W. Min, Z. Han, and L. Chen, 2006, The analysis for crust shortening of Kalpin thrust tectonic zone, south-western Tianshan, Xinjiang, China: Seismology and Geology, v. 28, no. 2, p. 194-204.

Yu, H., H. Fu, H. Huang, Q. Wu, and J. Chen, 2008, Feature of sedimentary and reservoir for the Yijiang Formation, Tahe oilfield: Mineralogy and Petrology, v. 28, no. 2, p. 95-101.

Yun, L., 2009, Petroleum accumulation model of Ordovician reservoir in Tahe Oilfield, Ph.D. thesis, China University of Geosciences (Beijing).

Zhang, K., X. Pang, Z. Zhao, X. Shao, X. Zhang, W. Li, and K. Wang, 2018, Pore structure and fractal analysis of Lower Carboniferous carbonate reservoirs in the Marsel area, Chu-Sarysu basin: Marine and Petroleum Geology, v. 93, p. 451–467, doi:10.1016/j.marpetgeo.2018.03.027.

Zhang, X., B. Liu, J. Wang, Z. Zhang, K. Shi, and S. Wu, 2014, Adobe photoshop quantification (PSQ) rather than point-counting: A rapid and precise method for quantifying rock textural data and porosities: Computers & Geosciences, v. 69, p. 62–71, doi:10.1016/j.cageo.2014.04.003.

Zhou, X., W. Ding, J. He, A. Li, Y. Sun, and X. Wang, 2018, Microfractures in the middle Carboniferous carbonate rocks and their control on reservoir quality in the Zanaral Oilfield: Marine and Petroleum Geology, v. 92, p. 462–476, doi:10.1016/j.marpetgeo.2017.11.009.

Zhou, X., X. Lü, H. Quan, W. Qian, X. Mu, K. Chen, Z. Wang, and Z. Bai, 2019, Influence factors and an evaluation method about breakthrough pressure of carbonate rocks: An experimental study on the Ordovician of carbonate rock from the Kalpin area, Tarim Basin, China: Marine and Petroleum Geology, v. 104, p. 313–330, doi:10.1016/j.marpetgeo.2019.03.034.

Zhou, Y., Z. Jin, D. Zhu, Y. Yuan, and S. Li, 2012, Current status and progress in research of hydrocarbon cap rocks: Petroleum Geology & Experiment, v. 34, no. 2, p. 234-245, 251.

Zhu, H., Y. Ju, Y. Qi, C. Huang, and L. Zhang, 2018, Impact of tectonism on pore type and pore structure evolution in organic-rich shale: Implications for gas storage and migration pathways in naturally deformed rocks: Fuel, v. 228, p. 272–289, doi:10.1016/j.fuel.2018.04.137.

Zhu, X., Z. Jin, T. Liang, S. Yi, K. Wei, B. Gao, and L. Shi, 2020, Depositional environment, diagenetic evolution, and their impact on the reservoir quality of the carboniferous KT-Ⅱ carbonate in the zhanazhol reservoir, Pre-Caspian Basin, Kazakhstan: Marine and Petroleum Geology, v. 117, p. 104411, doi:10.1016/j.marpetgeo.2020.104411.

Vitae

<u>JUN WU</u>~ School of Energy Resources, China University of Geosciences (Beijing),

Beijing, China; Key Laboratory of Marine Reservoir Evolution and Hydrocarbon Enrichment Mechanism, Ministry of Education, Beijing, China; Department of Mineralogy, Petrology and Applied Geology, Faculty of Earth Sciences, University of Barcelona, Barcelona, Spain; zgdzdxbjwj@126.com. Jun Wu is a lecturer at the China University of Geosciences (Beijing). He graduated in 2014 with a B.S. and received his Ph. D in 2020 from the same university. He has spent 1 year as a joint Ph. D. scholar at the University of Barcelona. His research focuses on carbonate sedimentology and diagenesis, carbonate cap rocks characterization, and their sealing capacity evaluation. He is a corresponding author of this paper.

TAILIANG FAN~ School of Energy Resources, China University of Geosciences (Beijing), Beijing, China; jhy17519@126.com. Tailiang Fan is a professor of Petroleum Geology at the China University of Geosciences (Beijing). He received his Ph. D. from this university in 1990. He is currently the leader of the Key Laboratory of Marine Reservoir Evolution and Hydrocarbon Enrichment Mechanism, Ministry of Education, China. He has worked for more than 30 years in petroleum exploration and development in the Tarim Basin. His research interests focus on sequence stratigraphy and sedimentology.

ENRIQUE GOMEZ-RIVAS~ Department of Mineralogy, Petrology and Applied Geology, Faculty of Earth Sciences, University of Barcelona, Barcelona, Spain; e.gomez-rivas@ub.edu. Enrique Gomez-Rivas is currently a research fellow at the

University of Barcelona. He graduated with a PhD in structural geology from the Autonomous University of Barcelona in 2008. After that he worked at the universities of Tübingen (Germany) and Aberdeen (United Kingdom) as researcher and lecturer, respectively. His research interests mainly focus on sedimentary geology, the formation of tectonic structures as well as on fluid-rock interactions, integrating field studies with numerical simulations.

<u>ANNA TRAVÉ</u>~ Department of Mineralogy, Petrology and Applied Geology, Faculty of Earth Sciences, University of Barcelona, Barcelona, Spain; atrave@ub.edu. Anna Travé is a professor at the University of Barcelona. She graduated with a PhD in sedimentary geology from this university. Her research interests focus on carbonate reservoir characterization, carbonate diagenesis and fluid flow and deformation.

<u>QIAN CAO</u>~ Exploration and Development Research Institute of PetroChina Changqing Oilfield Company, Xi'an, China; cq_325@163.com. Qian Cao is an engineer at the PetroChina Changqing Oilfield Company. She received her Ph.D. in 2019 from the China University of Geosciences (Beijing). She is mainly interested in pore structure characterization of carbonate rocks.

<u>ZHIQIAN GAO</u>~ School of Energy Resources, China University of Geosciences (Beijing), Beijing, China; gzq@cugb.edu.cn. Zhiqian Gao is a professor of petroleum geology at the China University of Geosciences (Beijing). He received his Ph.D. in 2007 from this university. His research interests focus on carbonate reservoir geology and sedimentology.

SHANSHAN WANG~ Beijing Municipal Commission of Planning and Natural Resources Yanqing Branch, Beijing, China; 18811589738@163.com. Shanshan Wang graduated with an M.S. from the China University of Geosciences (Beijing) in 2018. She is mainly interested in the prevention and control of geological hazards, the restoration and control of mine geological environments, and on the management of mineral resources.

ZHIHONG KANG~ School of Energy Resources, China University of Geosciences (Beijing), Beijing, China; kangzh98@cugb.edu.cn. Zhihong Kang is a professor of petroleum geology at the China University of Geosciences (Beijing). He received his Ph.D. in 2003 from the Chengdu University of Technology. His research interests focus on carbonate reservoir characterization and geomechanics. He is a corresponding author of this paper.

Figure captions

Fig. 1 (A) Map showing the location of the Tahe oilfield in the Tabei uplift and outcrops in the Keping uplift, northern Tarim Basin. (B) Map of four outcrops in the Keping uplift, including the Penglaiba (PLB), Kepingshuinichang (KPSNC), Yangjikan (YJK) and Dabantage (DBTG) outcrops. (C) Map of the Tahe oilfield, in which the studied wells are marked with brown dots (modified from Wu et al., 2018a).

Fig. 2 Synthetic stratigraphic column of the Tahe oilfield in the Akekule arch, Tabei uplift, Tarim Basin. The formations comprise upper Cambrian to Carboniferous rocks (modified from Tian et al., 2016).

Fig. 3 Detailed lithological succession from the Lower Ordovician Penglaiba Formation to the Middle Ordovician Yijiangang Formation. The thickness of each formation at the four outcrop analogues and subsurface drill wells of Tahe Oilfield are modified from Liu et al. (2017) and Wu et al. (2021). Red, dark blue, light blue, and green stars show the locations of samples from the Penglaiba, Dabantage, Yangjikan, and Kepingshuinichang outcrops.

Fig. 4 Burial and thermal history of the Yingshan Formation carbonate rocks in the Tahe oilfield and at the Dabantage and Penglaiba outcrops (modified after Dong et al., 2013; Du et al., 2016, 2017). The burial curve for the Tahe oilfield is shown in combination with homogenization temperatures of fluid inclusions, as well as the tectonic evolution of Ordovician rocks (modified from Chen et al., 2014).

Fig. 5 Thin-section photomicrograph of carbonate cap rocks and scanning electron microscopy (SEM) photomicrographs of pore types. ARS: alizarin red-stained thin section; PPL: plane-polarized light; MBD: impregnated with methylene blue dye. (A) Highly compacted peloidal packstone-grainstone, in which deformed peloids and stylolite can be observed. Sample from well AD27 at a depth of 6692.7 m, PPL; (B) Highly cemented peloidal grainstone, with point and linear contact between peloids.

Peloids occupy 68% of the total volume and intergranular pores were pervasively cemented with blocky cement. Sample 6 from the Penglaiba outcrop, PPL; (C) Highly cemented oolitic grainstone, in which ooids show different geometries and sizes. Sample from well S106, PPL; (D) Peloidal dolomitic limestone, with bladed calcite cement around peloids, exhibiting subhedral zoned dolomite crystals. Sample from the Penglaiba outcrop, ARS, PPL; (E) Incipiently dolomitized peloidal packstone-grainstone, in which local dolomitization is observed with highly corroded subhedral dolomite crystals. Sample 2 from the Penglaiba outcrop, ARS, PPL; (F) Incipiently dolomitized peloidal packstone-grainstone, with some bioclast fragments and scattered subhedral dolomite crystals. Sample 2 from the Penglaiba outcrop, PPL; (G) A microfracture partially filled with calcite cements, showing filled segments and isolated open segments. Sample from the Penglaiba outcrop, PPL, MBD; (H) Intercrystalline pores are randomly distributed and appear disconnected, with an open microfracture. Sample 35 from well AD27 at a depth of 6692.82 m, SEM.

Fig. 6 Thin-section and scanning electron microscopy (SEM) photomicrographs illustrating the main pore types and main diagenetic processes of carbonate cap rocks. (A) Parts of intercrystalline pores are occluded with illites. Sample 34 from well AD27 at 6690.88 m depth, SEM; (B) Intergranular pores are partially cemented by calcite crystals. Sample 15 from the Dabantage outcrop, SEM; (C) Bladed cement formed the first cement generation, and drusy cement formed the second one. Sample from well AD29 at 6692.7 m depth, alizarin red-stained (ARS), plane-polarized light (PPL); (D)

Meniscus calcite cement around peloids. A microfracture cuts the peloids and was completely filled with calcite cement. Sample from the Penglaiba outcrop, ARS, PPL.

Fig. 7 Thin-section photomicrographs and core photographs showing the effects of diagenetic processes of the carbonate cap rocks from the Yingshan Formation, Tarim Basin. (A) Three groups of peloids showing signs of having undergone mechanical compaction. Intergranular pores were completely occluded by calcite cements and dolomite crystals appear scattered in the host rock. Sample 12 from the Dabantage outcrop, alizarin red-stained (ARS), plane-polarized light (PPL), impregnated with methylene blue dye (MBD); (B) Suture and sharp peak type stylolite with an amplitude varying from 0.23 mm to 0.75 mm. Sample from the Dabantage outcrop, ARS, PPL; (C) Seismogram pinning type stylolite, with a variable amplitude ranging from 0.15 cm to 0.86 cm; (D) Dolomite crystals distributed along or in the vicinity of a stylolite, and pyrobitumen occluded the pore space within stylolites. Sample 13 from the Dabantage outcrop, ARS, PPL; (E) Pyrobitumen is pervasively distributed with a swarm of stylolites, with some dolomite crystals. Sample from the Penglaiba outcrop, PPL; (F) Dedolomitization belt within fine-crystalline dolomite and minor open intercrystalline pores. Sample from the Penglaiba outcrop, ARS, PPL, MBD.

Fig. 8 Types A, B, C and D carbonate cap rocks defined as high-pressure mercury intrusion porosimetry (HPMIP) curves. P_c and S_{Hg} are capillary pressure and mercury saturation, respectively. The numbers in the legend correspond to sample numbers.

Fig. 9 Cross-plot of porosity versus permeability of the four pore-structure types of 20 carbonate cap rocks.

Fig. 10 Sealing capacity defined as cover coefficients of carbonate cap rocks from wells (A) and outcrops (B) of the Yingshan Formation. (C) Comparisons of minimum, maximum and average cover coefficients of cap rock samples from wells and outcrops.

Fig. 11 Four classes of sealing capacity classification, their corresponding lithology, pore size distribution and average pore throat radius derived from HPMIP analysis, and diagenetic alterations of the Yingshan Formation carbonate cap rocks.

Fig. 12 Paragenetic sequence and sealing capacity variation associated with diagenetic processes of the Yingshan Formation at outcrops in the Tarim Basin.

Fig. 13 Relationship between $\delta^{13}C$ and $\delta^{18}O$ (‰, VPDB) of four types of calcite cements in the Yingshan Formation, Tarim Basin (modified from Chen et al., 2003).

Fig. 14 Pore structure evolution of carbonate cap rocks in relation to diagenetic alterations of the Yingshan Formation.

Fig. 15 Thin-section and scanning electron microscopy (SEM) photomicrographs of the Yingshan Formation carbonate cap rocks showing the impact of diagenetic alterations on the pore space and the rock's sealing capacity. (A) and (B) Cementation started earlier than compaction, intergranular pores were preserved during the progressive burial owing to the occurrence of sparry cements. Sample 15 in the Dabantage outcrop, which corresponds to plane-polarized light (PPL) and SEM, respectively. (C) and (D)

Compaction preceded cementation. A highly compacted cap rock exhibits linear grain contact and calcite cement precipitated within pore space. Sample 35 in the well AD27 at 6692.82 m depth, which corresponds to alizarin red-stained (ARS) (PPL) and SEM, respectively. (E) and (F) Dissolution vugs and partially filled microfractures acted as pathways between intergranular pores. Sample 8 in the Penglaiba outcrop, which corresponds to ARS (PPL) and SEM, respectively. In terms of the threshold capillary pressure and average pore throat radius, they can be arranged as follows: (C, D)> (E, F)> (A, B), (A, B)> (E, F)> (C, D). (G) Intensive mechanical compaction and residual bitumen are present within intergranular pores, PPL. (H) Residual bitumen occludes open stylolite, PPL, methylene blue dye (MBD).

Fig. 16 Minimum, maximum and average porosity (A), and minimum, maximum and average permeability (B) in relation to the four lithology types of carbonate cap rocks defined in the Tarim Basin.

Fig. 17 Cross-plot of grain size vs. cover coefficient in grainstone cap rocks.

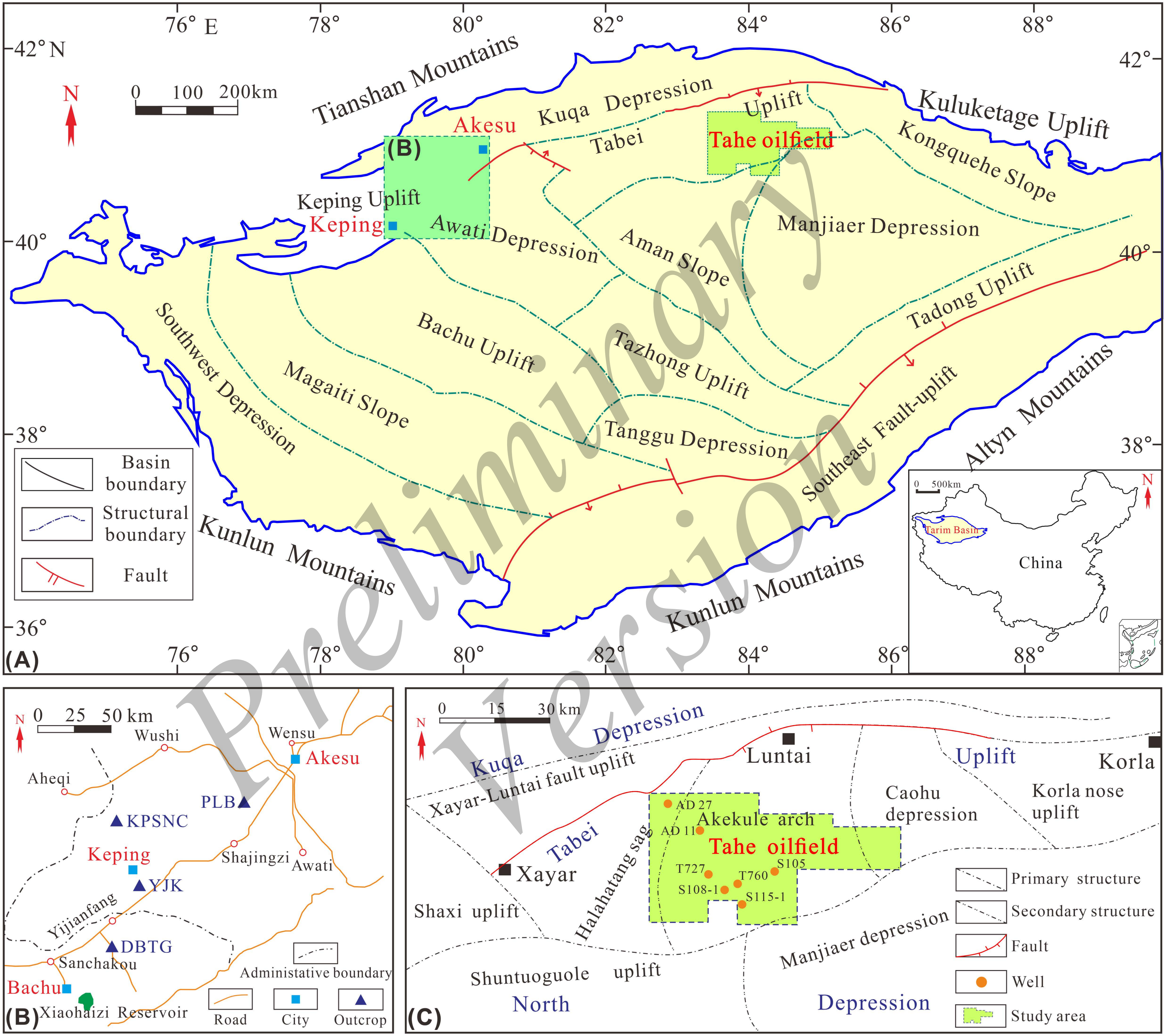
(A)
76° E
78°
80°
82°
84°
86°
88°
42° N
42°
40°
38°
36°
N
0 100 200km
Tianshan Mountains
Kuqa Depression
Uplift
Tahe oilfield
Akesu
Tabei
Kuluketage Uplift
Kongquehe Slope
(B)
Keping Uplift
Keping
Awati Depression
Aman Slope
Manjiaer Depression
Tadong Uplift
Southwest Depression
Magaiti Slope
Bachu Uplift
Tazhong Uplift
Tanggu Depression
Southeast Fault-uplift
Altyn Mountains
Kunlun Mountains
Basin boundary
Structural boundary
Fault
0 500km
Tarim Basin
China
(B)
0 25 50 km
Wushi
Wensu
Akesu
Aheqi
PLB
KPSNC
Keping
Shajingzi
Awati
YJK
Yijianfang
DBTG
Sanchakou
Bachu
Xiaohaizi Reservoir
Administative boundary
Road
City
Outcrop
(C)
0 15 30 km
Depression
Kuqa
Luntai
Uplift
Korla
Xayar-Luntai fault uplift
AD 27
Akekule arch
AD 11
Caohu depression
Korla nose uplift
Tabei
Tahe oilfield
Halahatang sag
Xayar
T727
T760
S105
S108-1
S115-1
Shaxi uplift
Manjiaer depression
Shuntuoguole uplift
North
Depression
Primary structure
Secondary structure
Fault
Well
Study area

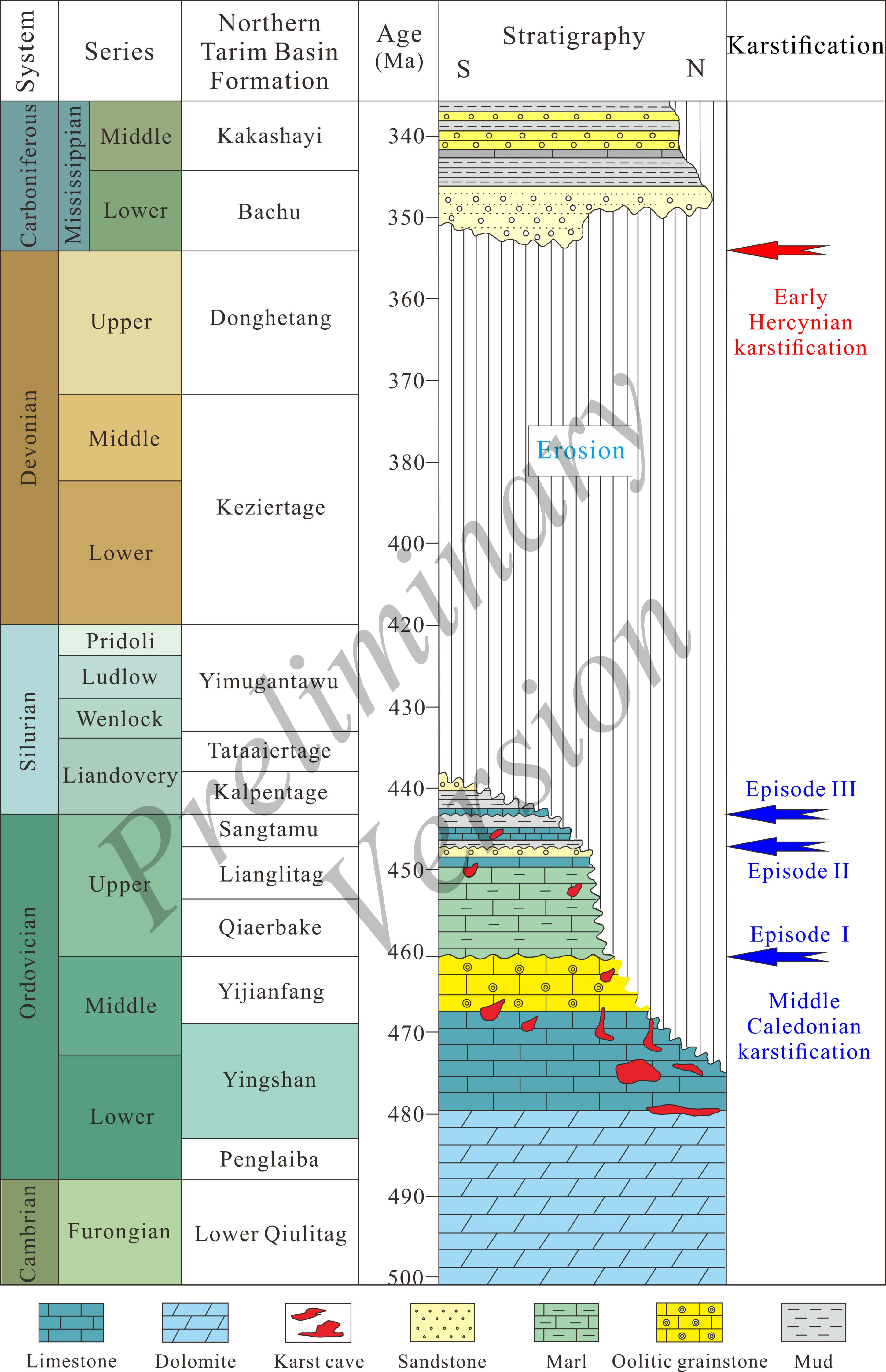
System
Series
Northern Tarim Basin Formation
Age (Ma)
Stratigraphy
S
N
Karstification
Carboniferous
Mississippian
Middle
Lower
Kakashayi
Bachu
Devonian
Upper
Middle
Lower
Donghetang
Keziertage
Silurian
Pridoli
Ludlow
Wenlock
Liandovery
Yimugantawu
Tataaiertage
Kalpentage
Ordovician
Upper
Middle
Lower
Sangtamu
Lianglitag
Qiaerbake
Yijianfang
Yingshan
Penglaiba
Cambrian
Furongian
Lower Qiulitag
340
350
360
370
380
400
420
430
440
450
460
470
480
490
500
Erosion
Early Hercynian karstification
Episode III
Episode II
Episode I
Middle Caledonian karstification
Limestone
Dolomite
Karst cave
Sandstone
Marl
Oolitic grainstone
Mud

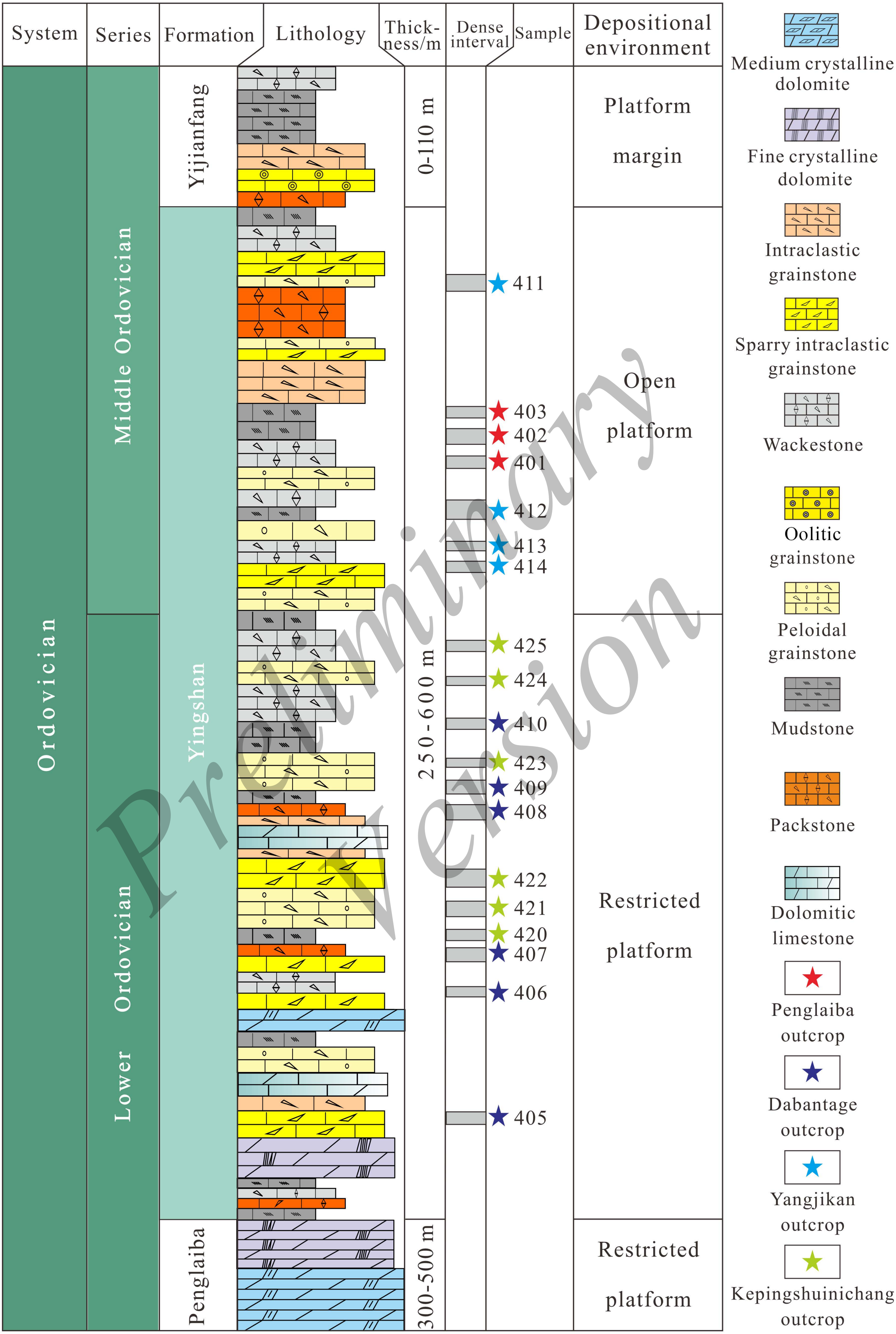
System
Series
Formation
Lithology
Thickness/m
Dense interval
Sample
Depositional environment
Ordovician
Middle Ordovician
Lower Ordovician
Yijianfang
Yingshan
Penglaiba
0-110 m
250-600 m
300-500 m
411
403
402
401
412
413
414
425
424
410
423
409
408
422
421
420
407
406
405
Platform margin
Open platform
Restricted platform
Restricted platform
Medium crystalline dolomite
Fine crystalline dolomite
Intraclastic grainstone
Sparry intraclastic grainstone
Wackestone
Oolitic grainstone
Peloidal grainstone
Mudstone
Packstone
Dolomitic limestone
Penglaiba outcrop
Dabantage outcrop
Yangjikan outcrop
Kepingshuinichang outcrop
Preliminary version

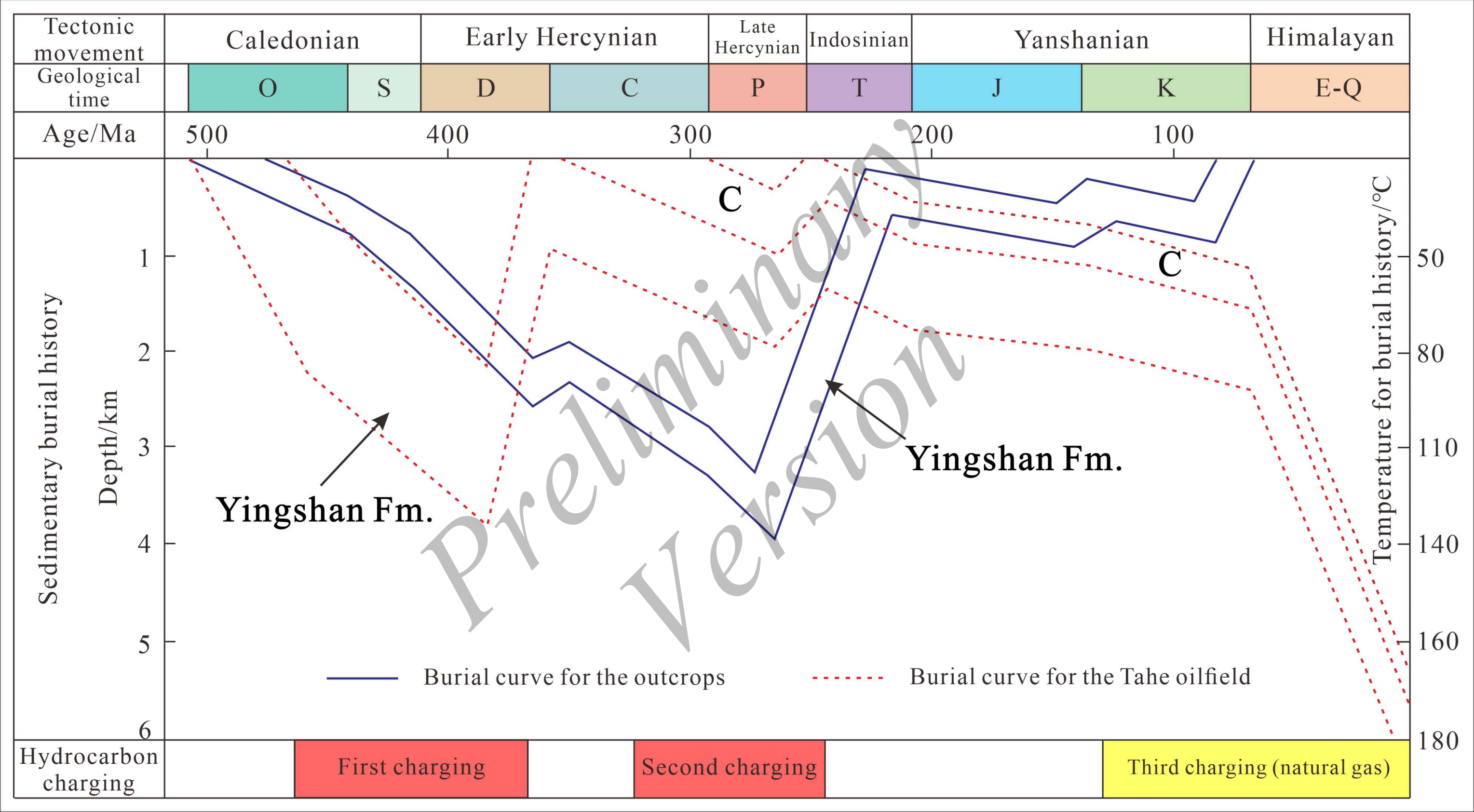

Tectonic movement
Caledonian
Early Hercynian
Late Hercynian
Indosinian
Yanshanian
Himalayan
Geological time
O
S
D
C
P
T
J
K
E-Q
Age/Ma
500
400
300
200
100
Sedimentary burial history
Depth/km
1
2
3
4
5
6
Temperature for burial history/°C
50
80
110
140
160
180
C
C
Yingshan Fm.
Yingshan Fm.
Burial curve for the outcrops
Burial curve for the Tahe oilfield
Hydrocarbon charging
First charging
Second charging
Third charging (natural gas)
Preliminary Version

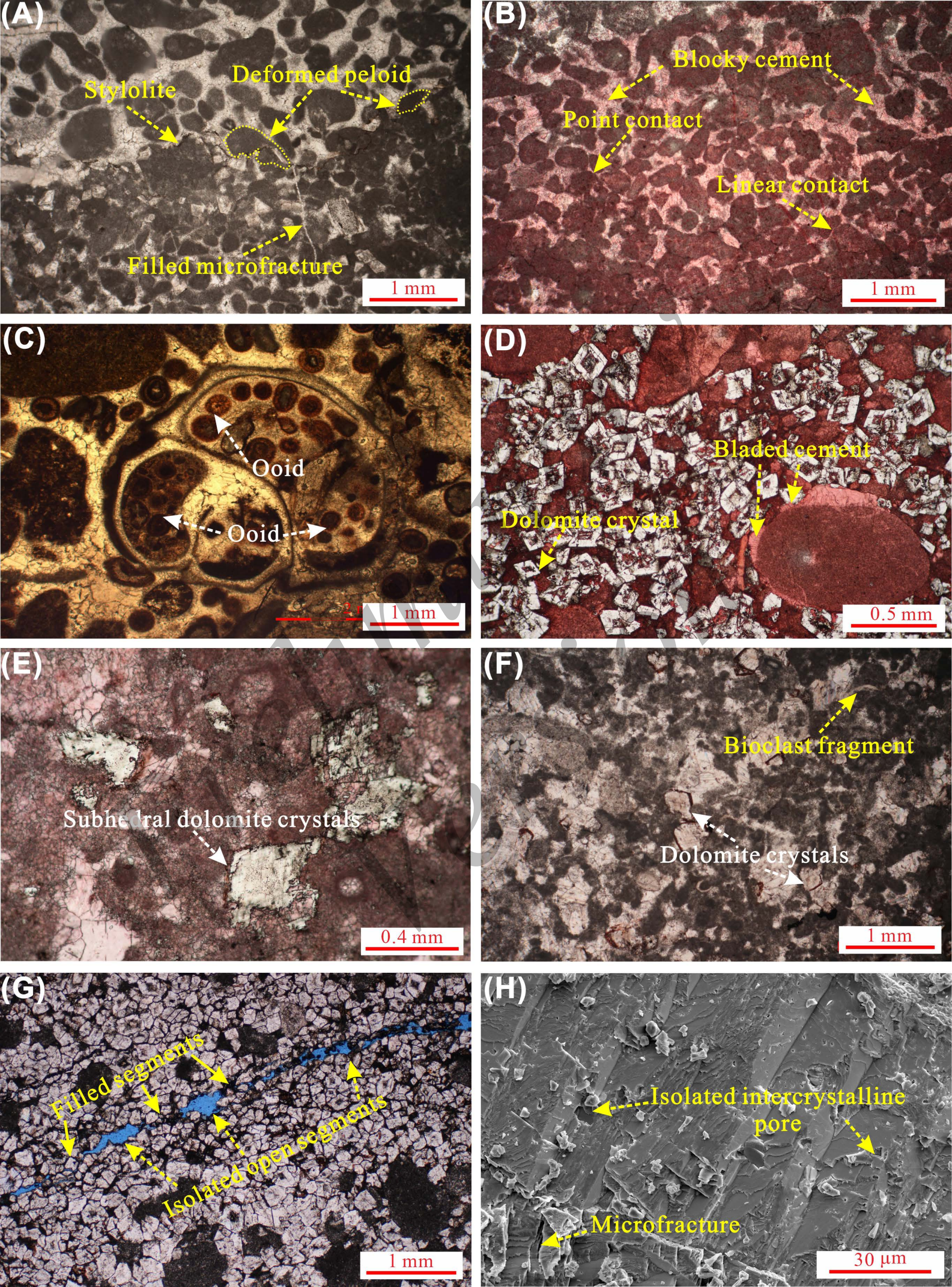
(A)
Stylolite
Deformed peloid
Filled microfracture
1 mm
(B)
Blocky cement
Point contact
Linear contact
1 mm
(C)
Ooid
Ooid
1 mm
(D)
Bladed cement
Dolomite crystal
0.5 mm
(E)
Subhedral dolomite crystals
0.4 mm
(F)
Bioclast fragment
Dolomite crystals
1 mm
(G)
Filled segments
Isolated open segments
1 mm
(H)
Isolated intercrystalline pore
Microfracture
30 μm

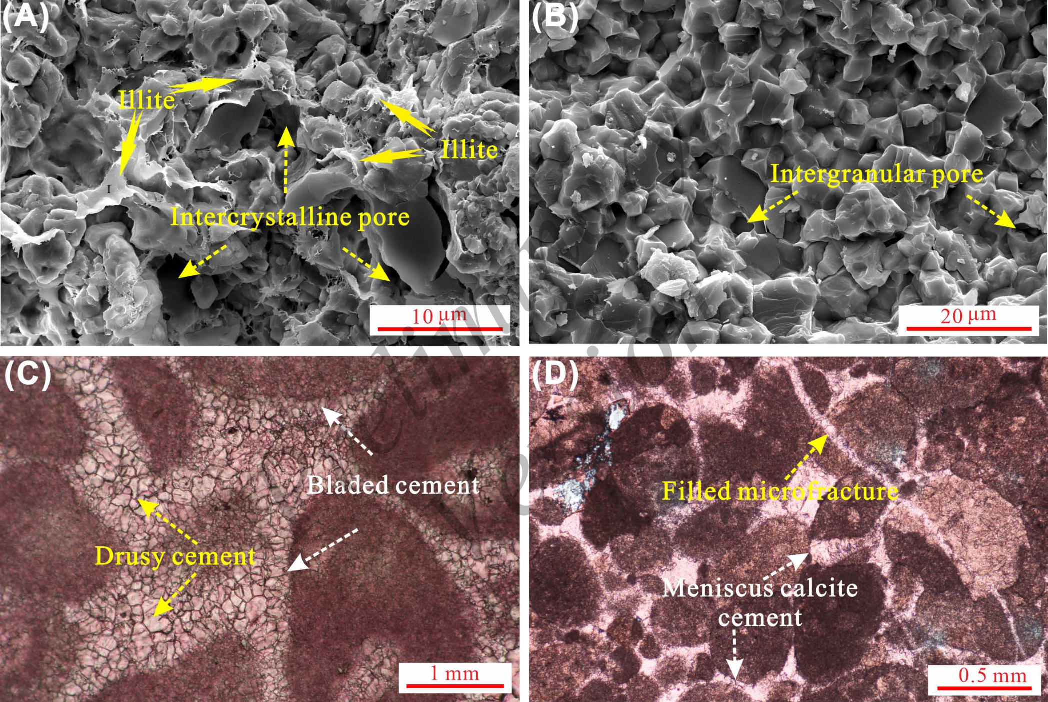
(A)
Illite
Illite
Intercrystalline pore
10 μm
(B)
Intergranular pore
20 μm
(C)
Bladed cement
Drusy cement
1 mm
(D)
Filled microfracture
Meniscus calcite cement
0.5 mm

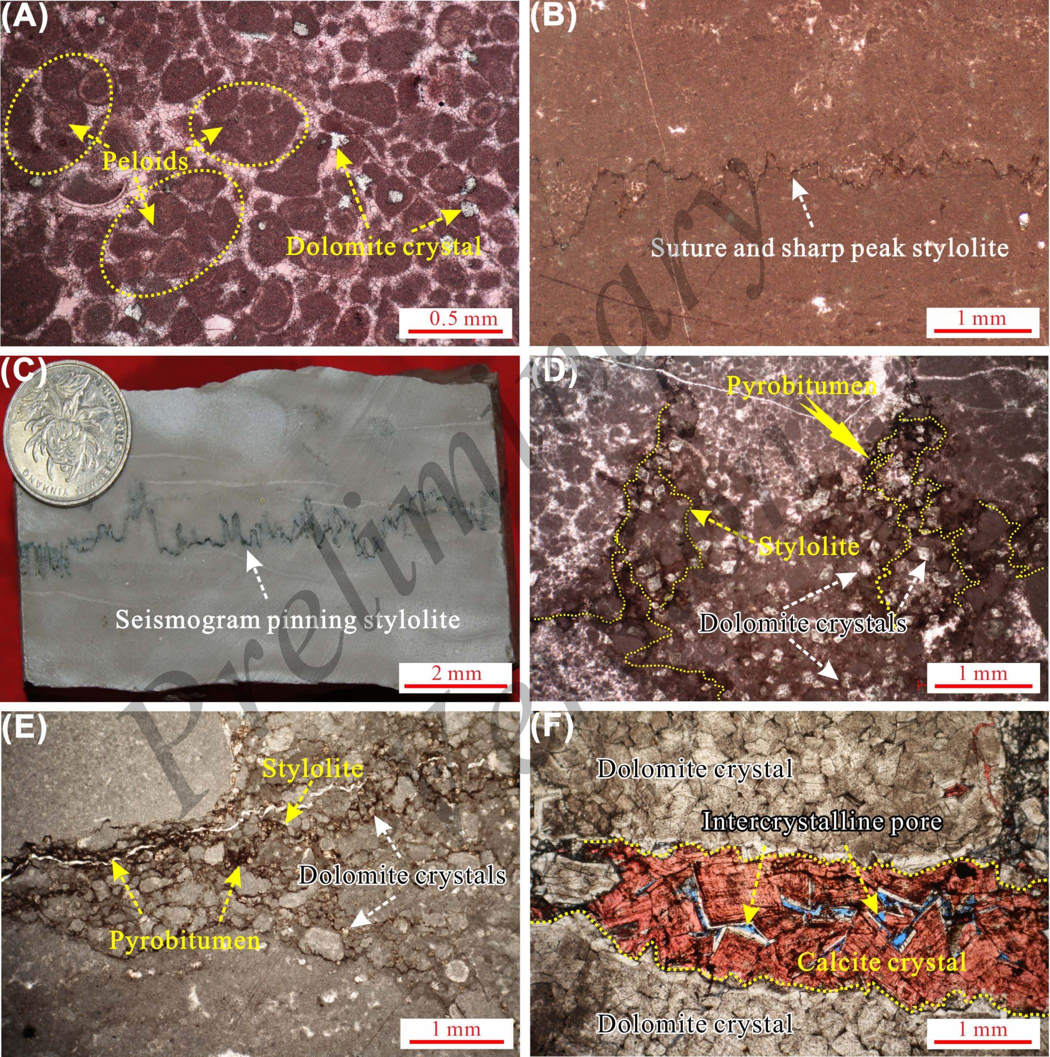
(A)
Peloids
Dolomite crystal
0.5 mm
(B)
Suture and sharp peak stylolite
1 mm
(C)
Seismogram pinning stylolite
2 mm
(D)
Pyrobitumen
Stylolite
Dolomite crystals
1 mm
(E)
Stylolite
Dolomite crystals
Pyrobitumen
1 mm
(F)
Dolomite crystal
Intercrystalline pore
Calcite crystal
Dolomite crystal
1 mm

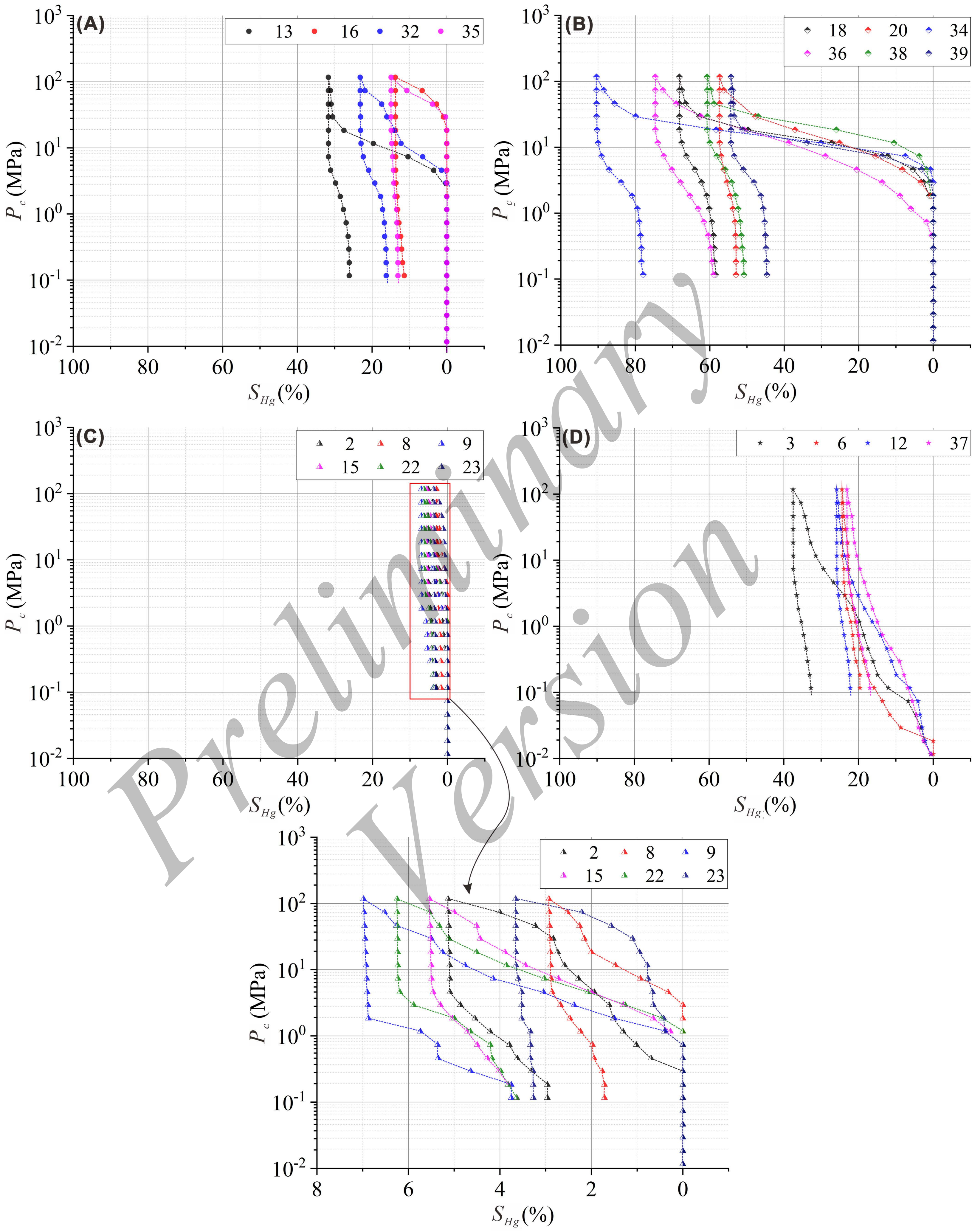
(A)
13
16
32
35
(B)
18
20
34
36
38
39
(C)
2
8
9
15
22
23
(D)
3
6
12
37
P_c (MPa)
S_{Hg}(%)
Preliminary Version

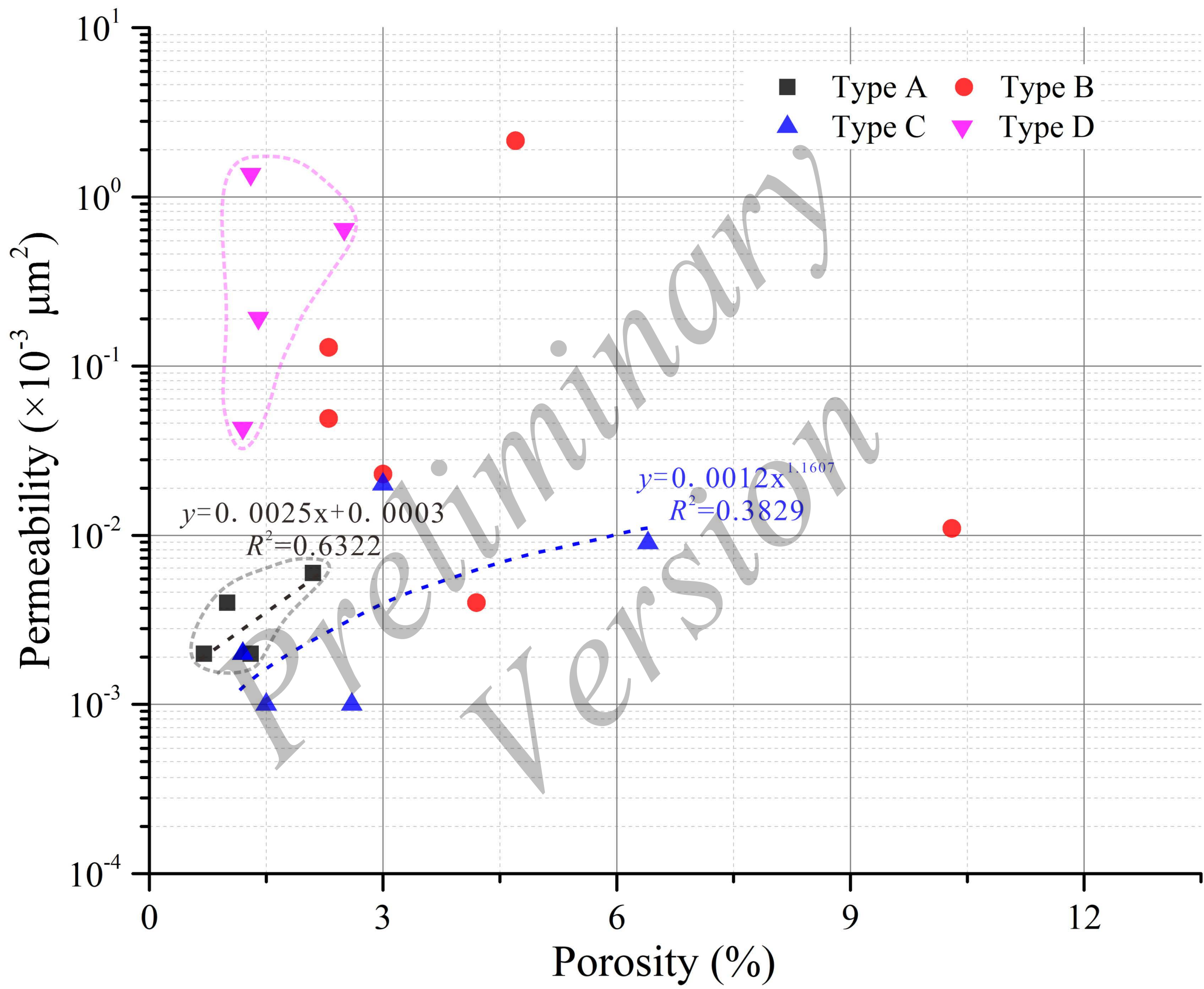

Type A
Type B
Type C
Type D
y=0. 0025x+0. 0003
R²=0.6322
y=0. 0012x^1.1607
R²=0.3829
Permeability (×10⁻³ μm²)
Porosity (%)
10¹
10⁰
10⁻¹
10⁻²
10⁻³
10⁻⁴
0
3
6
9
12
Preliminary Version

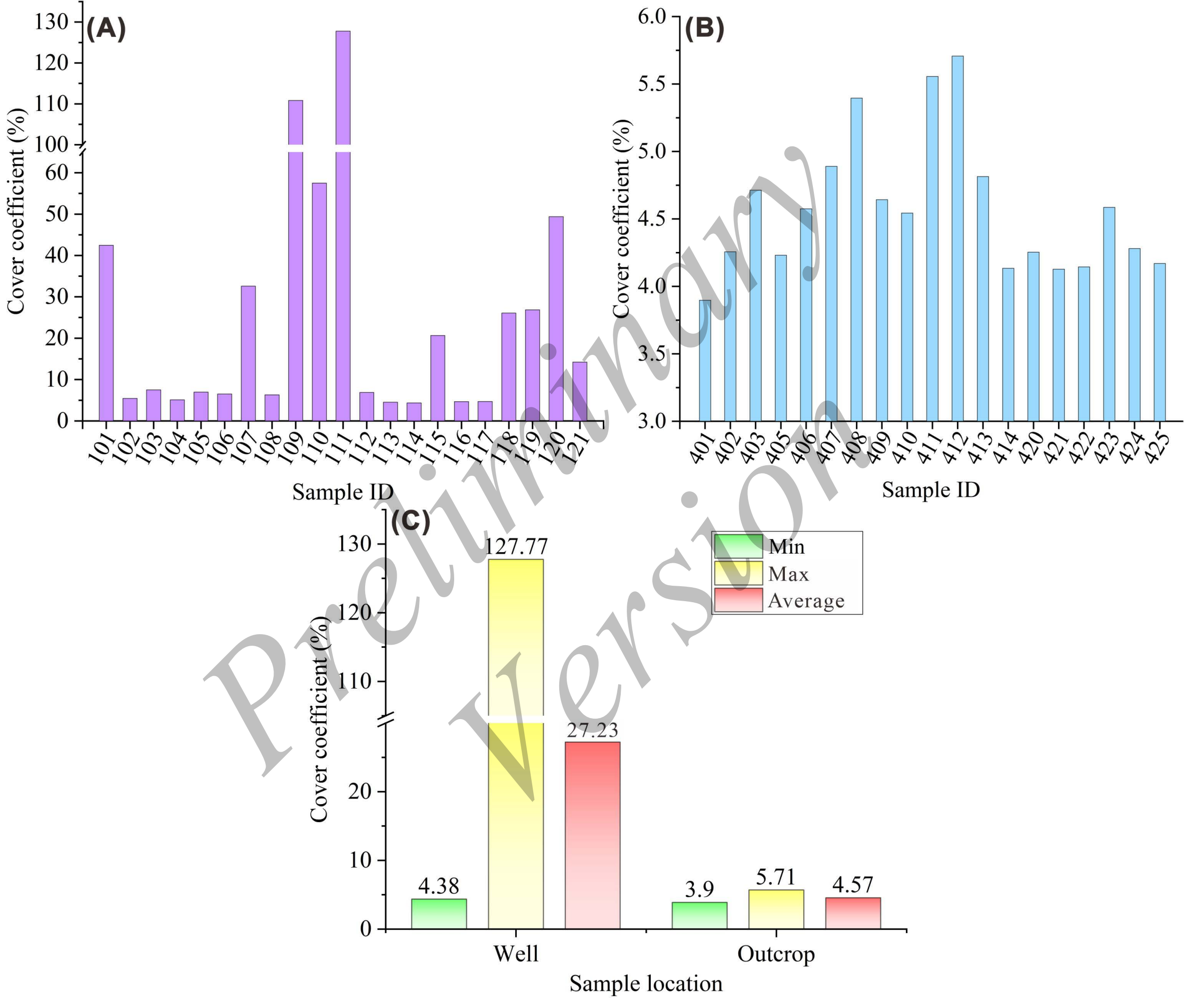
(A)
Cover coefficient (%)
0
10
20
30
40
50
60
100
110
120
130
101 102 103 104 105 106 107 108 109 110 111 112 113 114 115 116 117 118 119 120 121
Sample ID
(B)
Cover coefficient (%)
3.0
3.5
4.0
4.5
5.0
5.5
6.0
401 402 403 405 406 407 408 409 410 411 412 413 414 420 421 422 423 424 425
Sample ID
(C)
Cover coefficient (%)
0
10
20
110
120
130
Min
Max
Average
4.38
127.77
27.23
3.9
5.71
4.57
Well
Outcrop
Sample location

Sealing capacity classification	A Class I-best	B Class II-relatively good	C Class III-moderate	D Class IV-poor
Lithology	Incipiently dolomitized peloidal packstone-grainstone and highly cemented grainstone	Highly cemented grainstone and peloidal dolomitic limestone	Highly compacted peloidal packstone-grainstone and highly cemented grainstone	Highly compacted peloidal packstone-grainstone and peloidal dolomitic limestone
Pore type	Dominated by highly cemented intergranular and intercrystalline pores, lack of open microfactures	Dominated by disconnected microfractures and completely filled intergranular pores, and rare dissolution vugs	Dominated by partially occluded microfractures and isolated dissolution vugs, and minor scattered intergranular pores	Dominated by locally-filled microfractures and partially occluded intercrystalline pores, and minor dissolution vugs
SEM	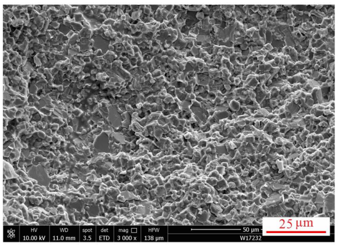	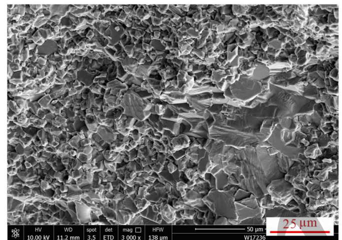	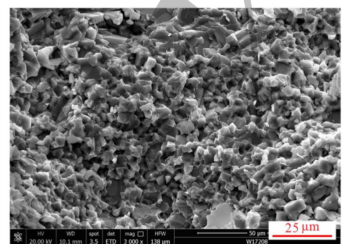	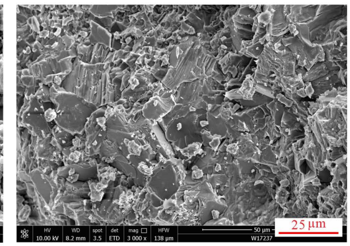
Pore size distribution	Micropore and transitional pore 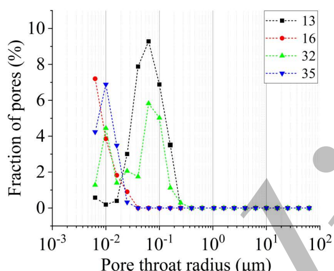	Transitional pore 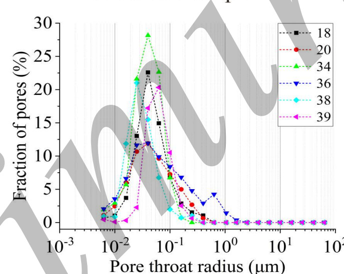	Transitional pore and mesopore 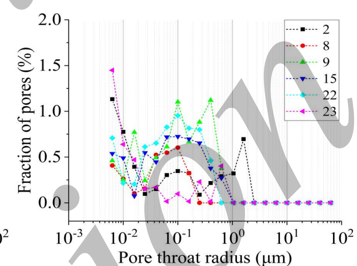	Macropore 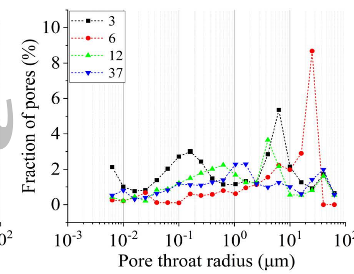
Main pore radius	0.025-1.0 μm	0.025-0.25μm	0.025-1.0 μm	>2.5 μm
Maximum pore radius (R_{max}) Average pore radius (R_a)	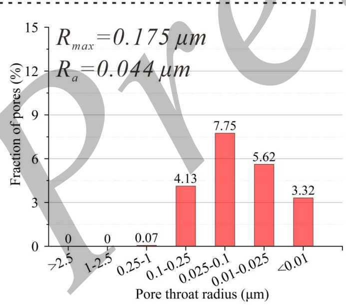	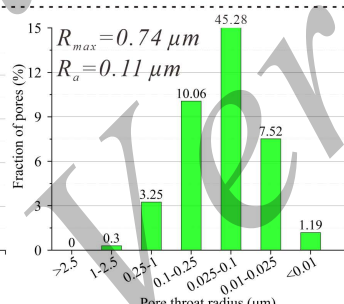	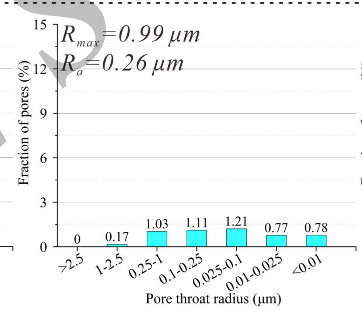	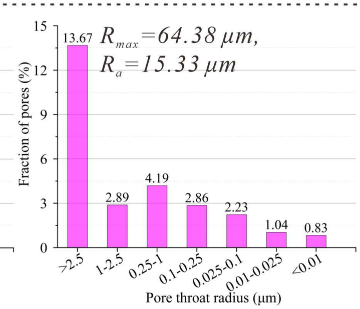
Diagenetic characteristics	Pervasive cementation, intense mechanical compaction, and abundant chemical compaction	Intense cementation, abundant mechanical and chemical compaction, rare dissolution and dolomitization	Moderate cementation, mechanical compaction, abundant chemical compaction, moderate dissolution, and dolomitization	Minor cementation, dolomitization and chemical compaction, moderate mechanical compaction, and intense dissolution
Thin-section photomicrograph	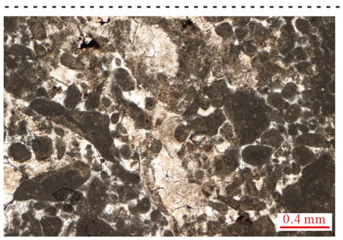	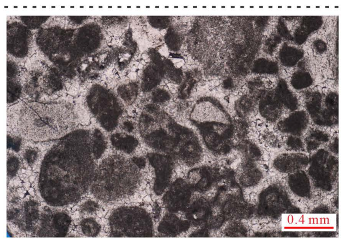	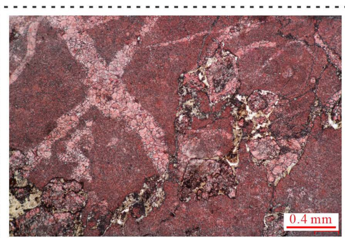	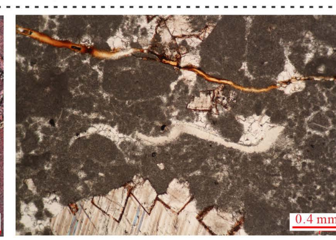

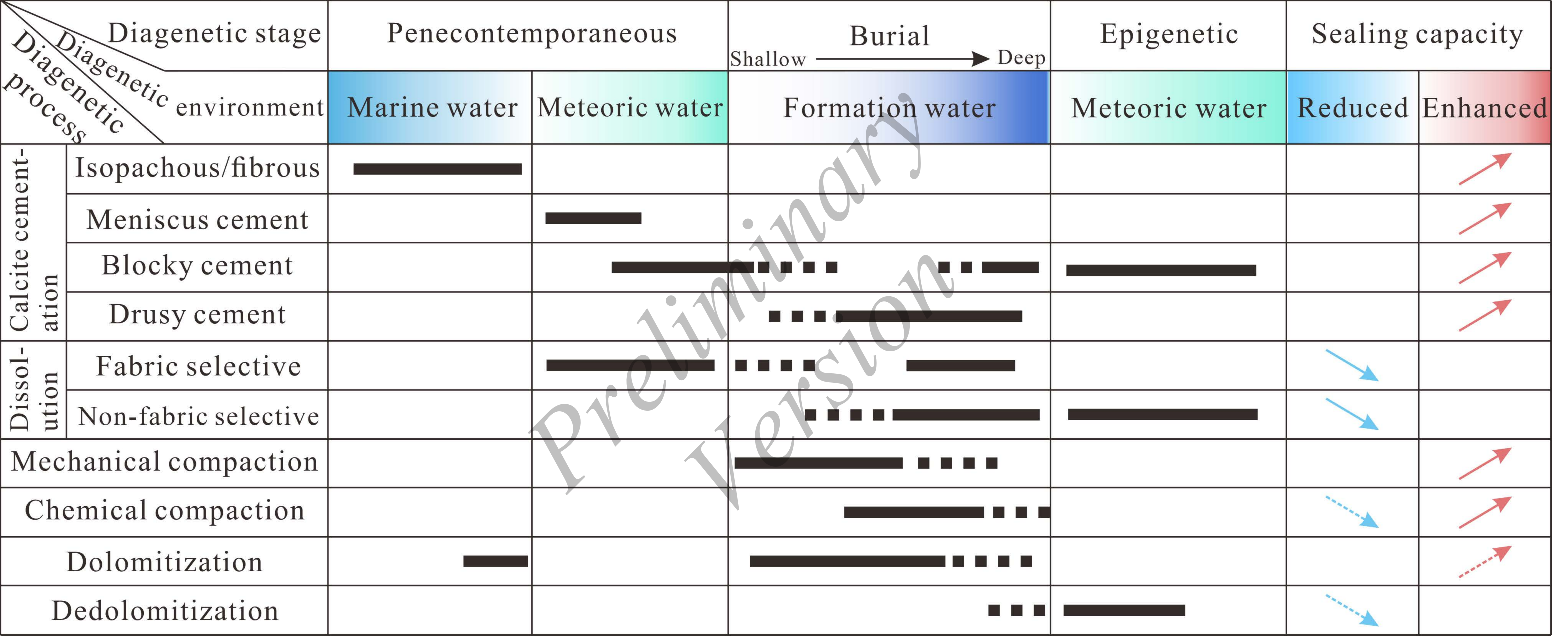
Diagenetic stage
Diagenetic environment
Diagenetic process
Penecontemporaneous
Burial
Shallow
Deep
Epigenetic
Sealing capacity
Marine water
Meteoric water
Formation water
Meteoric water
Reduced
Enhanced
Calcite cementation
Isopachous/fibrous
Meniscus cement
Blocky cement
Drusy cement
Dissolution
Fabric selective
Non-fabric selective
Mechanical compaction
Chemical compaction
Dolomitization
Dedolomitization
Preliminary Version

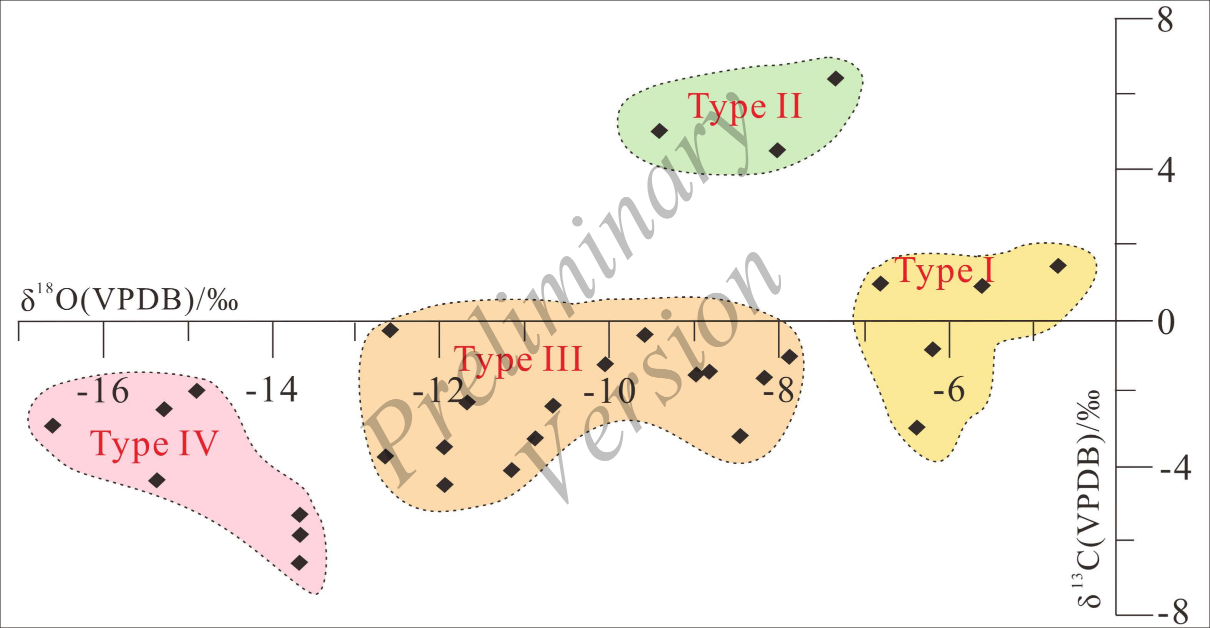

8
4
0
-4
-8
-16
-14
-12
-10
-8
-6
δ18O(VPDB)/‰
δ13C(VPDB)/‰
Type I
Type II
Type III
Type IV
Preliminary Version

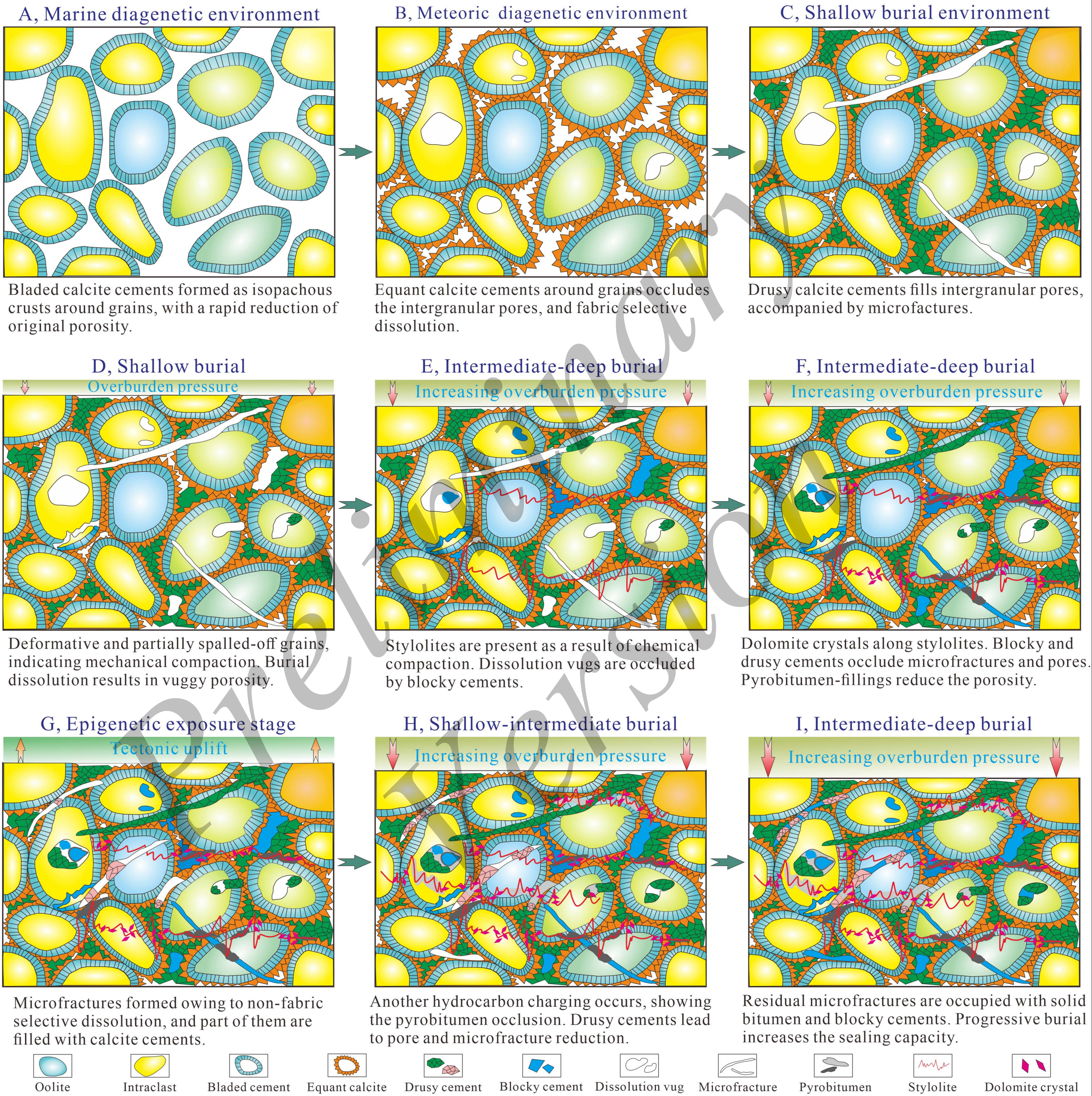
A, Marine diagenetic environment
B, Meteoric diagenetic environment
C, Shallow burial environment
Bladed calcite cements formed as isopachous crusts around grains, with a rapid reduction of original porosity.
Equant calcite cements around grains occludes the intergranular pores, and fabric selective dissolution.
Drusy calcite cements fills intergranular pores, accompanied by microfactures.
D, Shallow burial
Overburden pressure
E, Intermediate-deep burial
Increasing overburden pressure
F, Intermediate-deep burial
Increasing overburden pressure
Deformative and partially spalled-off grains, indicating mechanical compaction. Burial dissolution results in vuggy porosity.
Stylolites are present as a result of chemical compaction. Dissolution vugs are occluded by blocky cements.
Dolomite crystals along stylolites. Blocky and drusy cements occlude microfractures and pores. Pyrobitumen-fillings reduce the porosity.
G, Epigenetic exposure stage
Tectonic uplift
H, Shallow-intermediate burial
Increasing overburden pressure
I, Intermediate-deep burial
Increasing overburden pressure
Microfractures formed owing to non-fabric selective dissolution, and part of them are filled with calcite cements.
Another hydrocarbon charging occurs, showing the pyrobitumen occlusion. Drusy cements lead to pore and microfracture reduction.
Residual microfractures are occupied with solid bitumen and blocky cements. Progressive burial increases the sealing capacity.
Oolite
Intraclast
Bladed cement
Equant calcite
Drusy cement
Blocky cement
Dissolution vug
Microfracture
Pyrobitumen
Stylolite
Dolomite crystal

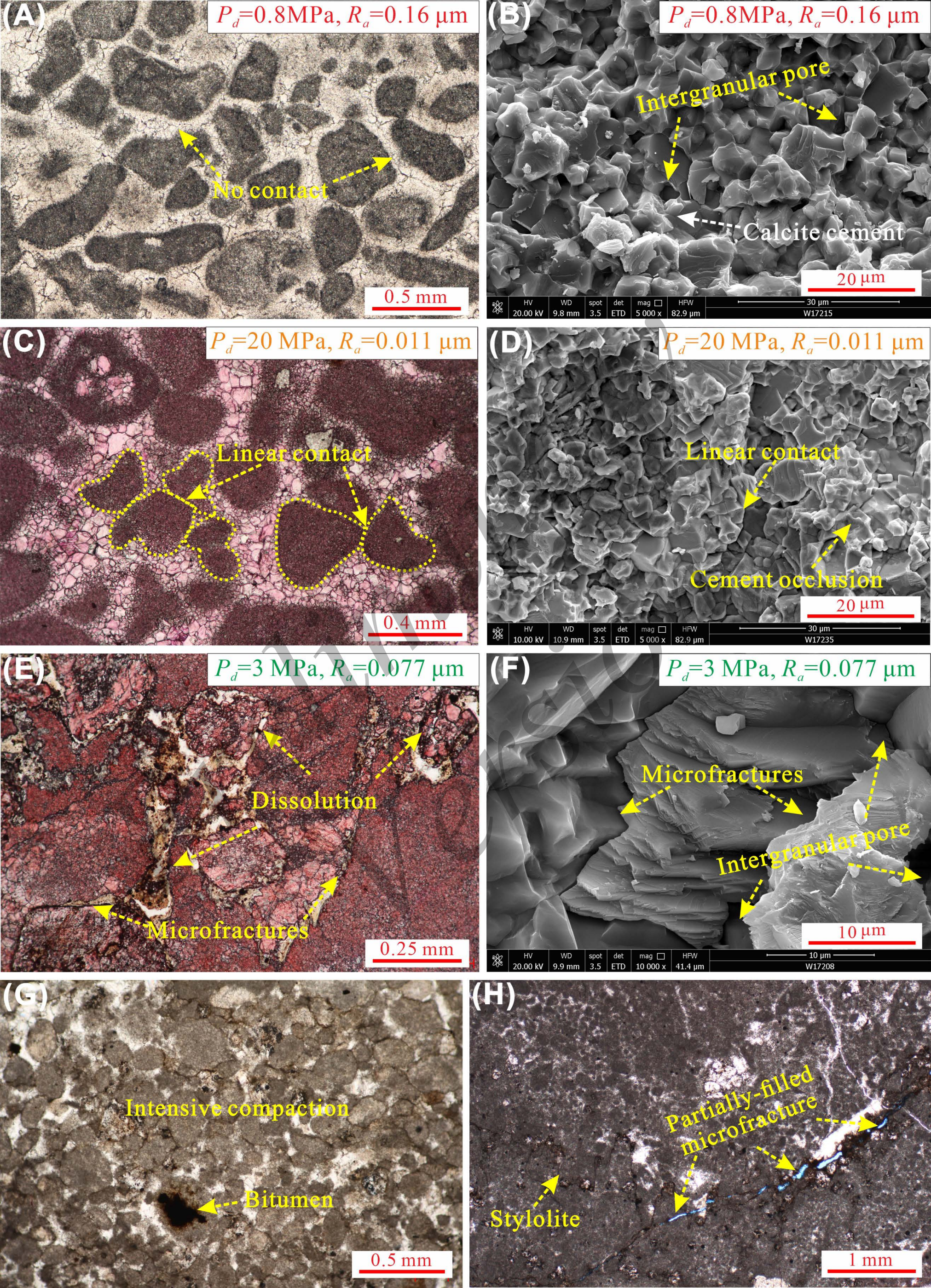
(A)
P_d=0.8MPa, R_a=0.16 μm
No contact
0.5 mm
(B)
P_d=0.8MPa, R_a=0.16 μm
Intergranular pore
Calcite cement
20 μm
(C)
P_d=20 MPa, R_a=0.011 μm
Linear contact
0.4 mm
(D)
P_d=20 MPa, R_a=0.011 μm
Linear contact
Cement occlusion
20 μm
(E)
P_d=3 MPa, R_a=0.077 μm
Dissolution
Microfractures
0.25 mm
(F)
P_d=3 MPa, R_a=0.077 μm
Microfractures
Intergranular pore
10 μm
(G)
Intensive compaction
Bitumen
0.5 mm
(H)
Partially-filled microfracture
Stylolite
1 mm

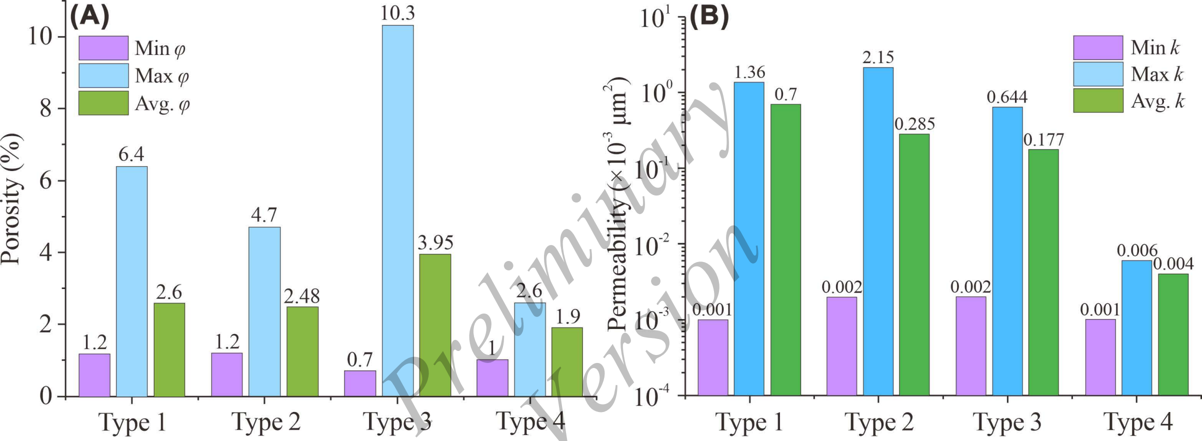

Type 1: Highly compacted peloidal packstone-grainstone

Type 2: Highly cemented intraclastic-ooidal-bioclastic grainstone

Type 3: Peloidal dolomitic limestone

Type 4: Incipiently dolomitized peloidal packstone-grainstone

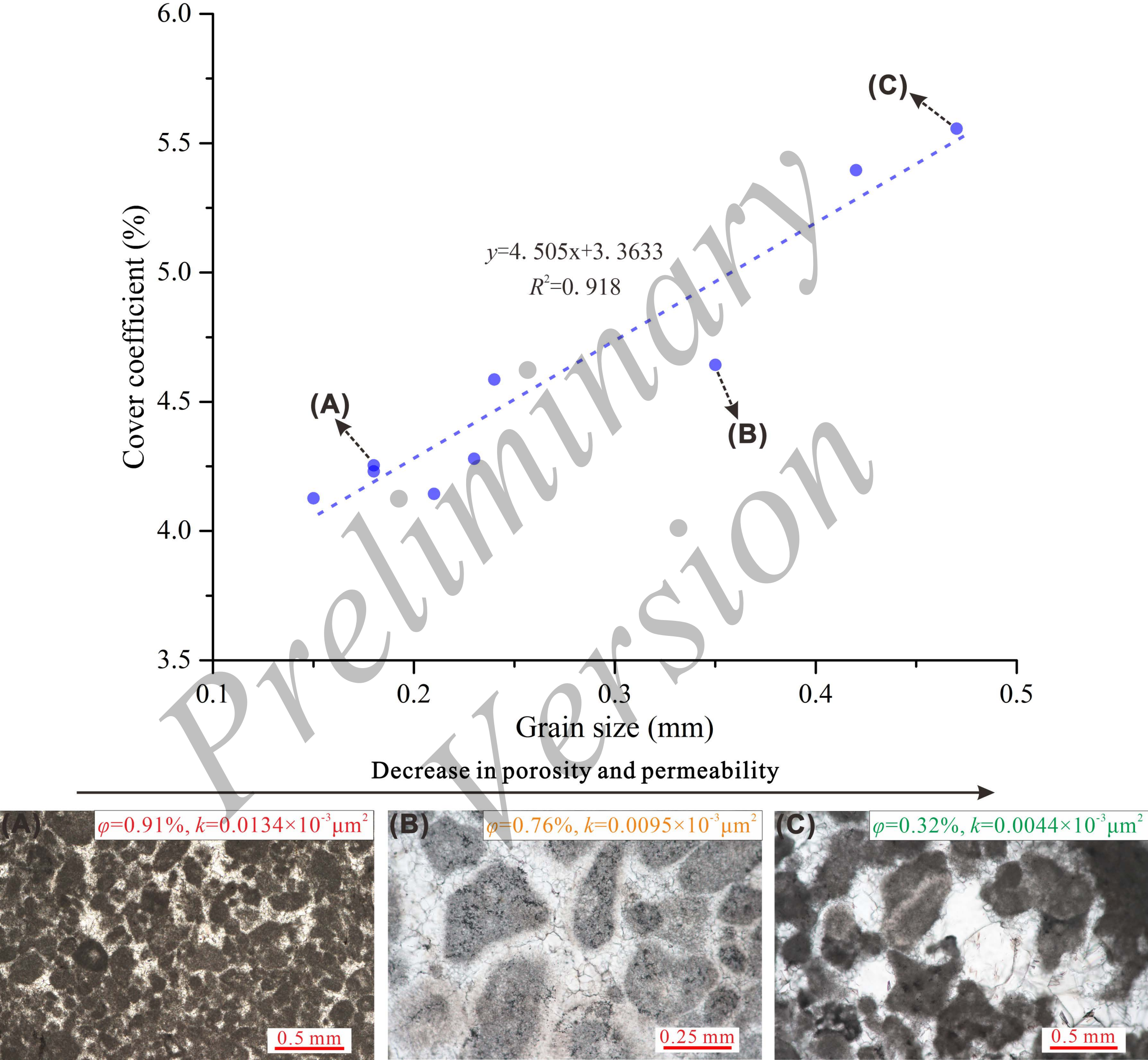
6.0
5.5
5.0
4.5
4.0
3.5
Cover coefficient (%)
0.1
0.2
0.3
0.4
0.5
Grain size (mm)
y=4. 505x+3. 3633
R^2=0. 918
(A)
(B)
(C)
Decrease in porosity and permeability
(A) φ=0.91%, k=0.0134×10^{-3}μm^2
0.5 mm
(B) φ=0.76%, k=0.0095×10^{-3}μm^2
0.25 mm
(C) φ=0.32%, k=0.0044×10^{-3}μm^2
0.5 mm

Table 1 Lithological type, sampling location and pore structure of carbonate cap rocks obtained from the HPMIP tests. Type 1: highly-compacted peloidal packstone-grainstone; Type 2: highly-cemented intraclastic-ooidal-bioclastic grainstone; Type 3: peloidal dolomitic limestone; Type 4: incipiently dolomitized peloidal packstone-grainstone; φ: porosity; K: permeability; P_t: threshold capillary pressure; R_{max}: maximum pore throat radius; P_{c50}: median saturation capillary pressure; R_{50}: median pore throat radius; S_{max}: maximum mercury intrusion saturation; W_e: efficiency of mercury withdrawal; R_a: average pore throat radius; S_k: skewness.

Pore type of rocks	Sample ID	Outcrop/well	Depth location (m)	Lithological type	φ (%)	K ($\times 10^{-3}$ μm^2)	P_t (MPa)	R_{max} (μm)	P_{c50} (MPa)	R_{50} (μm)	S_{max} (%)	W_e (%)	R_a (μm)	S_k
A	13	Dabantage	130.65	Type 4	1	0.004	3	0.25	-	-	31.72	17.69	0.081	1.81
	16	Dabantage	218.46	Type 3	0.7	0.002	20	0.04	-	-	13.78	17.37	0.011	2.70
	32	AD11	6709.68	Type 4	2.1	0.006	2	0.37	-	-	23.18	29.98	0.073	2.14
	35	AD27	6692.82	Type 2	1.3	0.002	20	0.04	-	-	14.92	12.42	0.011	2.59
Average A					1.28	0.0035	11.25	0.175	-	-	20.9	19.37	0.044	2.31
B	18	Well A	6549.03	Type 2	3	0.023	1.5	0.49	18.51	0.04	68.17	14.22	0.087	1.30
	20	Well A	6576.01	Type 2	4.2	0.004	1.5	0.49	33.91	0.022	57.36	7.66	0.097	1.41
	34	AD27	6690.88	Type 3	10.3	0.011	3	0.25	15.72	0.047	90.42	13.88	0.051	1.51
	36	S108-1	6058.98	Type 3	2.3	0.049	0.3	2.45	17.71	0.041	74.65	20.98	0.266	1.43
	38	T760	5974.06	Type 2	2.3	0.129	2	0.37	32.32	0.023	60.71	16.28	0.053	1.33
	39	T760	5979.48	Type 2	4.7	2.15	2	0.37	17.66	0.042	54.32	17.8	0.077	1.39
Average B					4.47	0.39	1.72	0.74	22.64	0.04	67.61	15.14	0.11	1.39
C	2	Penglaiba	20.52	Type 4	2.6	0.001	0.3	2.45	-	-	5.13	42.33	0.67	4.75
	8	Penglaiba	103.5	Type 1	1.2	0.002	3	0.25	-	-	2.93	41.53	0.077	5.96
	9	Penglaiba	105.46	Type 1	1.5	0.001	0.8	0.92	-	-	6.98	46.25	0.244	3.94
	15	Dabantage	205.09	Type 2	1.2	0.002	0.8	0.92	-	-	5.54	34.44	0.207	4.41
	22	Well A	6577.91	Type 2	3	0.02	1.5	0.49	-	-	6.25	41.83	0.16	4.13
	23	Well A	6579.87	Type 1	6.4	0.009	0.8	0.92	-	-	3.66	10.58	0.221	5.40

Average C					2.65	0.0058	1.2	0.99	-	-	5.08	36.16	0.26	4.77
	3	Penglaiba	26.45	Type 1	1.3	1.36	0.01	73.54	-	-	37.51	12.83	13.339	2.21
	6	Penglaiba	48.26	Type 2	1.2	0.043	0.02	36.77	-	-	24.42	19.73	16.303	3.06
	12	Dabantage	108.84	Type 2	1.4	0.192	0.01	73.54	-	-	25.83	13.99	14.7	2.46
	37	S115-1	6158.17	Type 3	2.5	0.644	0.01	73.54	-	-	23.08	26.63	16.979	2.68
Average D					1.6	0.5598	0.0125	64.38	-	-	27.71	18.30	15.33	2.60

Table 2 Sealing capacity defined as cover coefficient (*CC*) of carbonate cap rocks derived from the combination of mercury intrusion capillary pressure (MICP) and N_2GA.

Sample	Well	Depth (m)	*CC* (%)	Sample	Well	Depth (m)	*CC* (%)	Sample	Outcrops	*CC* (%)	Sample	Outcrops	*CC* (%)
101	AD11	6705.33	42.467	112	AD27	6691.22	6.914	401	Penglaiba	3.897	412	Yangjikan	5.707
102	AD11	6706.82	5.466	113	S105	6014.70	4.550	402	Penglaiba	4.256	413	Yangjikan	4.814
103	AD11	6706.93	7.540	114	S105	6024.85	4.384	403	Penglaiba	4.713	414	Yangjikan	4.134
104	AD11	6707.84	5.144	115	S108-1	6057.43	20.670	405	Dabantage	4.231	420	Kepingshuinichang	4.254
105	AD11	6708.17	6.991	116	S115-1	6157.80	4.692	406	Dabantage	4.575	421	Kepingshuinichang	4.127
106	AD11	6874.75	6.543	117	T727	6163.66	4.746	407	Dabantage	4.890	422	Kepingshuinichang	4.144
107	AD11	6876.44	32.606	118	T760	5975.93	26.097	408	Dabantage	5.396	423	Kepingshuinichang	4.586
108	AD11	6945.39	6.337	119	T760	5978.43	26.865	409	Dabantage	4.643	424	Kepingshuinichang	4.280
109	AD27	6688.85	110.818	120	T760	5982.32	49.390	410	Dabantage	4.543	425	Kepingshuinichang	4.170
110	AD27	6689.6	57.500	121	T760	5983.69	14.253	411	Yangjikan	5.556			
111	AD27	6690.53	127.771										

Table 3 Geological and geochemical characteristics of the diagenetic environments from the Lower Ordovician in the Tahe oilfield (modified from Chen, 2004).

Diagenetic environment		Properties of diagenetic media	Diagenetic assemblage	Geochemistry of cement
Marine water		The seawater between the grains has good fluidity, CO_2 escapes quickly, weak precipitation and significant bioturbation	Cementation, syntaxial overgrowth, and penecontemporaneous dolomitization.	B, Sr, Na close to the seawater, positive $\delta^{13}C$ and intermediate negative $\delta^{18}O$ signature.
Meteoric water		P_{O2}, P_{CO2}, Eh>0, low pH value	Cementation and dissolution.	Extremely low FeO, MnO, Na_2O, SrO and BaO.
Early shallow burial		Strongly influenced by meteoric freshwater, this stage is similar to that of freshwater. Salinized pore water with high pH and Eh<0.	Cementation, mechanical and chemical compaction, dolomitization and silicification. Hydrocarbon intrusion.	Fe and Mn increased.
Epigenetic meteoric water	Vadose zones	Pores were completely filled with meteoric water and air. Relatively high P_{O2} and P_{CO2}, low pH, Eh>0.	Cementation showing meniscus and equant calcite, vadose silt, dissolution, dedolomitization and ferritization. Hydrocarbon oxidation.	Low B, Sr, Na and Mn. Negative $\delta^{13}C$ and $\delta^{18}O$.
	Phreatic zones	Pores were saturated with freshwater, showing weak acidity and alkalinity. Water saturated with respect to $CaCO_3$ and fast precipitation.	Dissolution showing horizontal dissolution vugs and caverns, cementation and dedolomitization.	Low B, Sr and Na values. Negative $\delta^{13}C$ and $\delta^{18}O$.
Shallow-deep burial		Closed state diagenetic system with intense reduction environment, high temperature and high in-situ stress, $4 \leqslant pH \leqslant 6$.	Mechanical and chemical compaction, cementation, and burial dissolution.	Relatively high values of Fe, Mn, K, Na, B and F, but low Sr value. Positive $\delta^{13}C$ and negative $\delta^{18}O$.